5-2017

Magmatic Evolution of Early Subduction Zones: Geochemical Modeling and Chemical Stratigraphy of Boninite and Fore Arc Basalt from the Bonin Fore Arc

Emily A. Haugen
Utah State University

MAGMATIC EVOLUTION OF EARLY SUBDUCTION ZONES: GEOCHEMICAL MODELING AND CHEMICAL STRATIGRAPHY OF BONINITE AND FORE ARC BASALT FROM THE BONIN FORE ARC

by

Emily A. Haugen

A thesis submitted in partial fulfillment
of the requirements for the degree

of

MASTER OF SCIENCE

in

Geology

Approved:

_____	_____
John Shervais, Ph.D. Major Professor	Alexis Ault, Ph.D. Committee Member
_____	_____
Anthony Lowry, Ph.D. Committee Member	Mark R. McLellan, Ph.D. Vice President for Research and Dean of the School of Graduate Studies

UTAH STATE UNIVERSITY
Logan, Utah

2017

ABSTRACT

Magmatic Evolution of Early Subduction Zones: Geochemical Modeling and Chemical Stratigraphy of Boninite and Fore Arc Basalt from the Bonin Fore Arc

by

Emily A. Haugen, Master of Science

Utah State University, 2017

Major Professor: Dr. John Shervais
Department: Geology

IODP expedition 352 drilled four core in the Izu-Bonin fore arc in the Western Pacific. The Izu-Bonin fore arc records early subduction processes in the form of volcanics, notably Fore Arc Basalt (FAB) and boninite. FAB are Mid-Ocean Ridge Basalt (MORB)-like tholeiites with variable fluid mobile element enrichment and lower Ti/V ratio than MORB. Boninites are hydrous high-Mg andesite low in TiO_2 with a distinct subduction zone character and extreme depletion of Rare Earth Elements (REE). These volcanics are used to track the evolution of a subduction zone from initiation to maturity with FAB produced first and boninite produced later. Forward modeling of mantle-derived melts from a Deplete MORB Mantle source composition produces FAB from ~20% melt in the spinel lherzolite field and 1% in the garnet lherzolite field. Boninite is modeled from high degrees of melt the FAB residue and requires an addition of melt to

match the model with observed samples. Three types of boninite have been sampled, Basaltic Boninite (BB), Low-Silica Boninite (LSB), and High-Silica Boninite (HSB). Within the core, LSB is produced first with HSB modeled from the LSB residue. BB is generated throughout the core.

The geochemistry of the four core analyzed records period of recharge and fraction of the magma chamber. The base of Core U1442A and U1439C record a transition from more FAB-like samples to boninite samples from low Cr and high Al concentrations. Few of the shipboard-defined units record magma mixing as seen by the scatter in the depth plots and petrographically. Enrichment of Fluid Mobile Elements and High-Field Strength incompatible Elements indicate a subduction input in the form of fluids and melt.

(190 pages)

PUBLIC ABSTRACT

Magmatic Evolution of Early Subduction Zones: Geochemical Modeling and Chemical Stratigraphy of Boninite and Fore Arc Basalt from the Bonin Fore Arc

Emily A. Haugen

The Izu-Bonin-Mariana arc stretches south from Japan to Guam in the Western Pacific. International Ocean Discovery Project Expedition 352 drilled four core in the fore arc of the Izu-Bonin arc east of the Bonin Islands: U1439C, U1440B, U1441A, and U1442A. From the four core, 124 samples were retrieved and analyzed for major and trace elements. Two main rock types were identified: FAB and boninite. FAB is a Mid-Ocean Ridge Basalt (MORB)-like tholeiite with variable fluid mobile element enrichment such as Rb, Ba, and Sr, and low Ti/V ratios more similar to an island arc volcanic than a mid-ocean ridge volcanic. Boninite is a hydrous high-Mg andesite with low TiO_2 and distinctive subduction zone characteristics in the form of elevated fluid mobile elements and melt mobile elements. FAB was assumed to be formed from a Depleted MORB-Mantle (DMM) source and the boninite was formed from a depleted mantle source, presumably the mantle after FAB melt was extracted. Here, we used the Rare Earth Elements (REE) of the samples to model melt scenarios for the FAB and boninite in order to better understand the initial volcanic product of subduction zones.

This research was funded by in joint by the National Science Foundation,

Consortium for Ocean Leadership, and International Ocean Discovery Program. 124 samples were analyzed using an X-Ray Fluorescence (XRF) and Inductively Coupled Plasma - Mass Spectrometer (ICP-MS) to determine the major and trace elements. These analyses were then used to recreate the chemostratigraphy defined by the shipboard crew and determine variations within the core. We found that there was variability as the magma evolved over time and mixed with other melts, seen in magma mixing horizons. Boninite samples were separated based on their SiO_2 and MgO concentrations into Basaltic Boninite (BB), Low-Silica Boninite (LSB), and High-Silica Boninite (HSB) with BB being more primitive and HSB being more evolved.

These volcanics are the first known products of the subduction zone and were used to model the early evolution of the subduction zone. FAB was the first product due to its proximity to the trench and greater age than the boninite. Assumed to be generated from DMM, FAB was modeled with a total melt extraction of ~20% spinel lherzolite and 1% garnet lherzolite. Boninite was assumed to be generated from the FAB residue because it requires a depleted source and because the FAB residue was within the hydrous flux melt zone of the subduction factory. Boninite was modeled at high degree of melt from the FAB residue, however an additional melt must be added to the model to match the observed samples. We proposed a small fraction of FAB melt mixed with the models because it is still present in the subduction factory, observed in core U1439C with a FAB sample in the HSB regime.

ACKNOWLEDGMENTS

I would like to thank Dr. John Shervais for making available to me the core he collected on IODP Expedition 352 to the Bonin Fore Arc and data therein, and my committee members Drs. Alexis Ault and Anthony Lowry for their support and assistance throughout the entire process. I would also like to thank the IODP 352 Researchers for their input at meetings and sharing of data.

Emily A. Haugen

CONTENTS

Page

LIST OF TABLES

LIST OF FIGURES

CHAPTER I

INTRODUCTION

The Izu-Bonin-Mariana arc is a west-dipping, ocean-ocean convergent plate margin. The arc extends ~2500 km south from Japan to Guam in the Western Pacific (Figure 1). Subduction at this arc initiated approximately 52 Ma (Meijer et al., 1983; Cosca et al., 1998; Ishizuka et al., 2006; Reagan et al., 2010). This arc has been the subject of considerable research on subduction zones, subduction initiation, and subduction evolution. Researchers have dredged, drilled, and conducted dives near the arc since founding of the Deep-Sea Drilling Project (DSDP) in 1966. Despite on-going research, outstanding questions persist regarding geochemical and chronologic signatures of subduction initiation. Varying rock types observed in this system hint at the complexity of the process (Johnson and Fryer, 1990; Ishizuka et al., 2006; Reagan et al., 2010; Ishizuka et al., 2011; Reagan et al., 2013). Proposed geodynamic models attempt to explain how subduction initiates and how the mantle responds to the sinking plate and deformation above the subduction zone (e.g., Meijer et al., 1982; Hickey and Frey, 1982; Johnson and Fryer, 1990; Stern and Bloomer, 1992; Pearce et al., 1992; Cosca et al., 1998; Ishizuka et al., 2006; Reagan et al., 2010; Ishizuka et al., 2011; Reagan et al., 2013; Arculus et al., 2015).

The Izu-Bonin-Mariana arc is highly studied for several reasons. First, it is a juvenile arc at ~52 Ma with little erosion (Johnson and Fryer, 1990). The

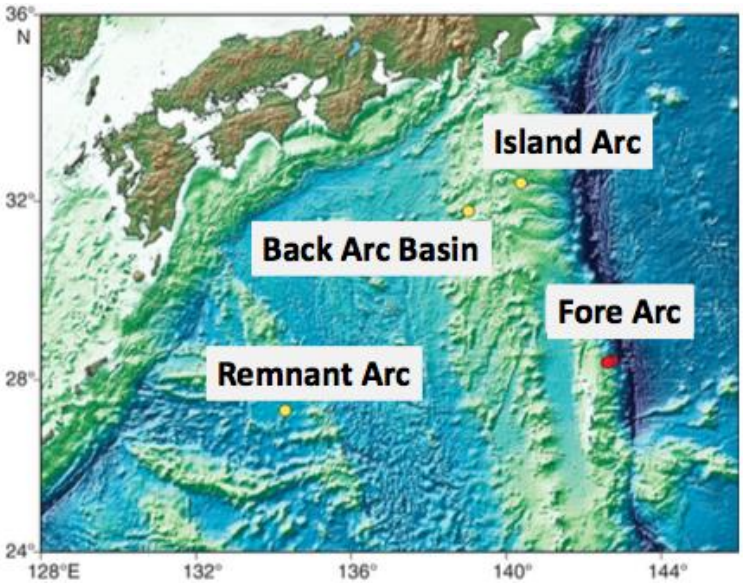

Figure 1. Location map for IODP Expedition 352. Located in the Western Pacific south of Japan. Red circles mark drilling locations of IODP Exp. 352. Fore Arc lies just west of the trench. Island Arc is west of the Fore Arc. Back Arc Basin is west of the Island Arc. Remnant Arc created from back arc rifting, located further west. (Figure modified from Preliminary Report Reagan et al., 2015)

volcanic arcs associated with the complex have not weathered away, including the present-day volcanic arc, as well as the older initial arc that has since been rifted away by back arc basin processes (Figure 1). Second, it is a non-accretionary plate margin lacking excess sediment, which allows access to the first lavas erupted at this subduction zone (Johnson and Fryer, 1990).

Geochemical study of the Izu-Bonin-Mariana complex allows us to better understand and characterize early subduction and subduction initiation, as well as providing a better understanding of ophiolite complexes around the world. The two key lava types in this system are fore arc basalt (FAB) and boninite. FAB is a mid-ocean ridge basalt (MORB)-like tholeiitic lava that has variable fluid soluble elements and lower Ti/V ratios than normal-MORB (Reagan et al., 2010).

Boninite is a hydrous high-Mg andesite low in TiO_2 with a distinct subduction zone character, indicated by the enrichment of fluid-soluble elements such as Sr, K, Rb, and Ba (Cameron et al, 1979; Hickey and Frey, 1982; Falloon and Crawford, 1991; Sobolev and Danyushevsky, 1994; Taylor et al, 1994; Bédard et al., 1998).

In the summer of 2014, International Ocean Discovery Program (IODP) Expedition 352 cored four drill sites in the Bonin fore arc to sample boninite, fore arc basalt (FAB), and the transition between the two lava types (Reagan et al., 2015). The four drill sites lie on an east-west line from the trench to the Bonin Islands (Figure 2). From east to west, the sites consist of two FAB dominated cores, holes U1440B and U1441A, and two boninite dominated cores, holes U1439C and U1442A (Figure 2). FAB is interpreted as the first volcanic product

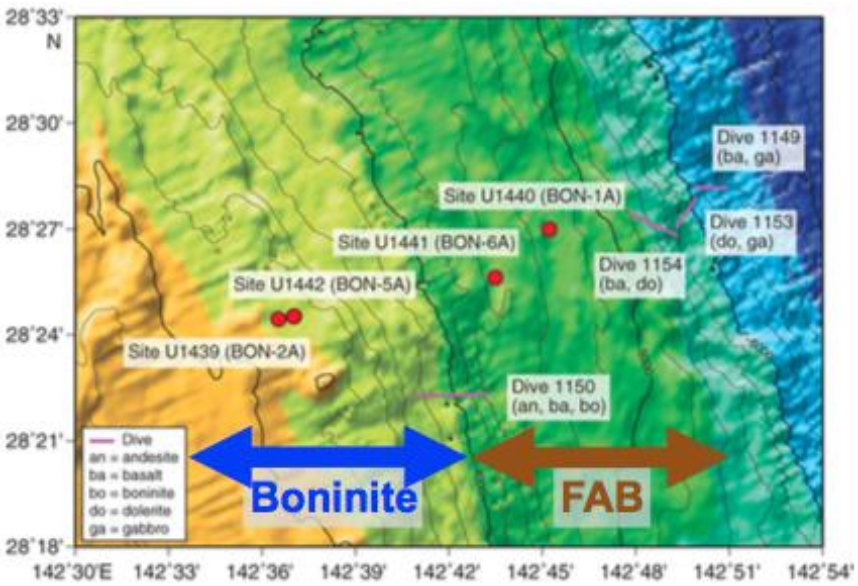

Figure 2. IODP 352 drill sites. Boninite dominated holes U1439C and U1442A lie to the west. FAB dominated holes U1441A and U1440B lie to the east. Trench lies to the east and the Bonin islands lie to the west. (Figure modified from Preliminary Report Reagan et al., 2015)

of the subduction zone due to its proximity to the trench and previous reports of FAB underlying the boninite (Reagan et al., 2010). Access to these cores permits unique geochemical characterization of these units.

The relationship between FAB and boninite in the Bonin fore arc is unusual due to their different geochemistry and magmagenesis styles. FAB is generated through decompression melting of the mantle, giving it a MORB-like signature, while boninite is generated through hydrous flux melting of depleted mantle over a subducting slab, giving it a subduction zone signature (Cameron et al., 1979; Coish et al., 1982; Hickey and Frey, 1982; Umino and Kushiro, 1989; van der Laan et al., 1989; Pearce et al., 1992; Kostopoulos and Murton, 1992; Sobolev and Danyushevsky, 1994; Brenan et al., 1995; Keppler, 1996; Bédard et al., 1998; Ishikawa et al., 2002; Reagan et al., 2010). Despite the differences in generation, these lavas are related with respect to (1) time, with FAB erupting from ~52-48 Ma and boninite erupting from ~48-45 Ma, and (2) spatial distribution, FAB is locally interleaved with boninite in the Mariana arc (Cosca et al., 1998; Ishizuka et al., 2006; Reagan et al., 2010).

The purpose of this research is to decode the geochemical signature of the FAB to boninite transition in this unique setting to ultimately understand the magmagenesis relationship between these two components of the subduction system. To evaluate this question, I will use four IODP drill cores to create a chemostratigraphy of the fore arc in the FAB to boninite transition. Using this chemical stratigraphy, I will determine if boninite is generated from the depleted mantle that produced the FAB, or from an unrelated mantle source. These data

will be used to address the question of how mantle melting progresses through magmatic evolution during subduction initiation to early subduction by tracking trace element fractionation. Ultimately, I will use the high-precision chemical stratigraphy of the fore arc cores to decipher minute but important changes to the composition of the lavas and therefore the mantle over time.

BACKGROUND

The Izu-Bonin-Mariana arc is composed of rocks entirely of arc origin due to an absence of an accretionary wedge (Johnson and Fryer, 1990). Subduction and subduction-related volcanism occurred nearly simultaneously along the length of the present-day arc, characterized by boninitic volcanism at similar dates in samples taken from various locations on the arc (Figure 3) (Ishizuka et al., 2006, Ishizuka et al., 2011). K-Ar and Ar-Ar dates from pillow lava and associated sediment constrain subduction initiation at ~52 Ma and the time of boninitic volcanism from ~48-45 Ma (Cosca et al., 1998; Ishizuka et al., 2006; Ishizuka et al., 2011; Reagan et al., 2013). The time of subduction initiation is coincident with the estimated change in Pacific Plate motion as evidenced by the bend in the Hawaiian-Emperor Sea mount chain; however, the cause of subduction initiation remains unknown (Meijer et al., 1983; Cosca et al., 1998; Ishizuka et al., 2006; Reagan et al., 2010). The time between subduction initiation and boninitic volcanism can be explained by the initial production of FAB which must be ~>49 Ma based on the overlying lavas and interpretation that FAB

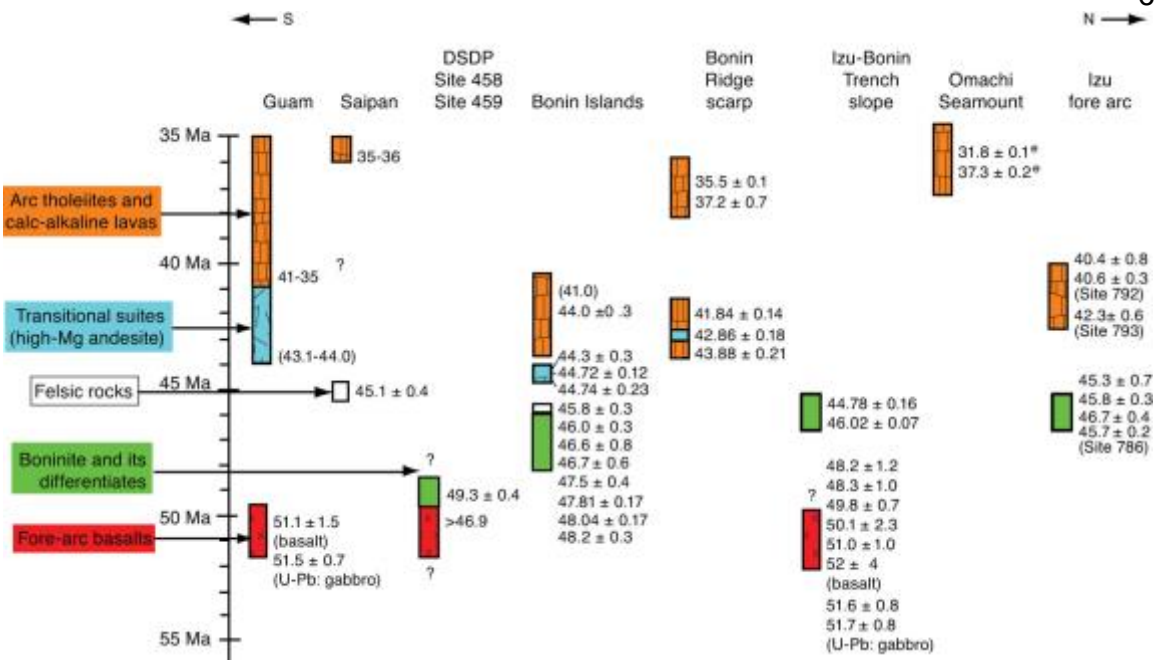

Figure 3. Published dates from the IBM fore arc and island arcs. Dates show FAB erupting from ~48-52 Ma and boninite erupting from ~44-49 Ma. The transitional suite known as HMA erupts from ~43-44 Ma and island arc volcanics erupted from ~31-43 Ma. (Figure from Ishizuka, 2006)

locally underlies boninite (Cosca et al., 1998; Ishizuka et al., 2006; Reagan et al., 2010). FAB cannot be much older than boninite due to a lack of evidence of a hiatus as seen in Ar/Ar and U-Pb dating, as well as the existence of transition lavas from FAB-like to boninite-like described from DSDP site 458 (Reagan et al., 2010).

The Bonin ridge fore arc (known as the Ogasawara ridge in Japanese), where the four core from IODP Expedition 352 were drilled, is ~400 km long and trends north-south. Previous work on this section of fore arc occurred via diving and dredging, and by drilling on Deep Sea Drilling Project (DSDP) leg 160 and Ocean Drilling Program (ODP) legs 125 and 126 (Hussong and Uyeda, 1982;

Bloomer, 1983; Taylor, 1992; Arculus et al., 1992; Murton et al., 1992; Pearce et al., 1992; Taylor et al., 1992; Ishizuka et al., 2006). Before FAB was recognized as a product of subduction, DSDP sites 458 and 450 recovered boninites underlain by tholeiitic basalt (Hickey-Vargas, 1989, Ishizuka et al., 2006). This discovery of tholeiitic basalt (FAB) indicates that, in addition to boninitic volcanism, FAB volcanism also occurred simultaneously along the arc.

Kikuchi (1890) first described boninite on the Bonin Islands, while Peterson (1891) named it. Johannsen (1937) described boninite petrographically, and Kuroda and Shiraki described it chemically in the 1970s (Shiraki and Kuroda, 1977; Kuroda et al., 1978). Boninite is a hydrous high-magnesium andesite with very low TiO_2 that is enriched in Large Ion Lithophile Elements (LILE) compared to MORB, giving it a U-shaped trace element pattern, and lacking plagioclase (Cameron et al., 1979; Hickey and Frey, 1982; Falloon and Crawford, 1991; Sobolev and Danyushevsky, 1994; Taylor et al., 1994; Bédard et al., 1998). The International Union of Geological Sciences have defined boninite as having >52 wt% SiO_2, < 0.5% TiO_2, and >8 wt% MgO (Pearce and Robison, 2010). Boninite generation was previously poorly understood because it required a depleted mantle (harzburgite) under hot hydrous LILE enriched conditions and low pressures (Sun and Nesbitt, 1978; Cameron et al., 1979; Coish et al., 1982; Hickey and Frey, 1982; Kostopoulos and Murton, 1992; Brenan et al., 1995; Keppler, 1996).

More recently, researchers determined boninite occurred in young, hot subduction zones from melting of depleted mantle at temperatures below 1250°C

and depths below 30 km in the presence of water (1-5 wt% in the primary magma) (Green 1973; Umino and Kushiro, 1989; van der Laan et al., 1989; Stern and Bloomer, 1992; Pearce et al., 1992; Falloon and Danyushevsky, 2000; Ishikawa et al 2002; Parman and Grove, 2004; Reagan et al., 2010). Umino and others (2015) estimated temperature-pressure conditions for boninite from melt inclusions at 1345-1421ºC and 0.56-0.85 GPa for boninites 48-46 Ma and 1381ºC at 0.85 GPa for boninite at 45 Ma. Due to the specific circumstances of boninite generation, they occur primarily during early subduction within the fore arc (Bédard et al., 1998; Stern, 2002; Ishizuka et al., 2006). Boninites have been found in several ophiolite complexes around the world, e.g., Troodos (Rogers et al., 1989; Portnyagin et al., 1997), Oman (Ishikawa et al., 2002), Mirdita (Dilek et al., 2007; Dilek et al., 2008), Pindos (Dilek and Furnes, 2009), Othris (Barth and Gluhak, 2009), Kudi (Yuan et al., 2005), Betts cove (Bédard et al., 1998), and the Bay of Islands (Bédard et al., 1998).

Boninite drilled in the Izu-Ogasawara and Mariana fore arc terranes during Leg 125 has previously been segregated into three distinct suites: low-Ca boninite, intermediate-Ca boninite, and high-Ca boninite (Crawford et al., 1989; Pearce et al., 1992; Arculus et al., 1992). Low-Ca boninite is described as the oldest unit, characterized by dikes and sills below a pillow lava horizon, and an average CaO/Al_2O_3 ratio of 0.41. Low Ti content indicates that the low-Ca boninite was generated via pooling of melt fractions from the uppermost part of the lithosphere and is produced from the most depleted mantle source (Crawford et al., 1989; Pearce et al., 1992; Arculus et al., 1992). Low-Ca and intermediate-

Ca boninite have the highest La/Sm ratios and lowest Tb/Yb ratios, producing a distinct U-shaped trace element profile. Intermediate-Ca boninite occurs in the main dike series, pyroclastic flows, and breccias above the pillow lava horizon. It has an average ratio of CaO/Al_2O_3 of 0.60. Generated from a slightly less depleted source than the Low-Ca boninite, or from the same source but with less melting of the depleted source, the high-Ca boninite is the youngest boninite type and is characterized by dikes or sills throughout the basement. High-Ca boninite has an average CaO/Al_2O_3 ratio of 0.84, the highest Ti content, higher Y and Yb, lower Th, and flatter trace element profiles than the low-intermediate-Ca boninites. As a result, the high-Ca boninites likely are generated from pooling of melt fractions from the lowermost part of the lithosphere.

During IODP Expedition 352, boninite was split into three distinct suites: high-silica boninite (HSB), low-silica boninite (LSB), and basaltic boninite (BB). Boninite samples were divided into the three categories as depicted by the MgO-SiO_2 discrimination diagram (Figure 4). High-silica boninites (HSB) are characterized by high silica (>57.5% SiO_2 at 8% MgO) and >8 wt% MgO. Low-silica boninite (LSB) are characterized by low silica (54-57.5% SiO_2 at 8% MgO) and >8 wt% MgO. Basaltic boninite (BB) are characterized by the lowest silica (52-54% SiO_2 at 8% MgO) and >8 wt% MgO. High-magnesium andesite (HMA), also considered evolved low-silica boninite, are characterized by low-high silica and <8 wt% MgO. HMA have high magnetic susceptibility due to groundmass Fe-Ti oxides, unlike the low susceptibility of boninites.

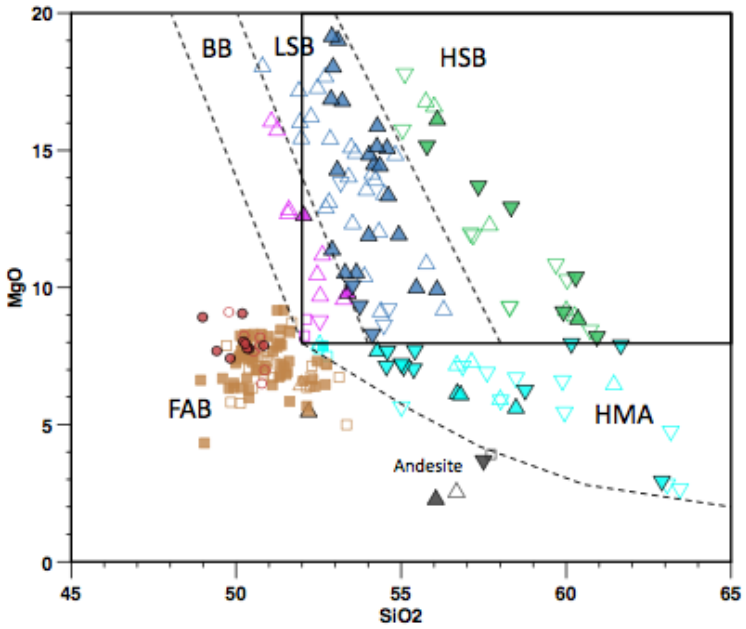

Figure 4. MgO-SiO_2 Discrimination Diagram. FAB (orange-red) field at the corner of the boninite box. Boninites divided into three types: Basaltic Boninite (BB - purple), Low-Silica Boninite (LSB - blue), and High-Silica Boninite (HSB - green). High-Mg Andesite (light blue) below boninite field and above the curve. Upright triangles are U1439C samples, inverted triangles are U1442A samples, circles are U1441A samples, and Squares are U1440B samples. (Legend in Appendix A) Unfilled samples are Pool samples from Godard et al., in prep. (Figure modified from Preliminary Report Reagan et al., 2015)

Boninite consists of common phenocrysts that appear in all types of boninite. Olivine is the most common phenocryst present along with rare low-calcium pyroxene. High calcium pyroxene appears in BB and HMA along with olivine. The groundmass is pale tan glass with abundant microlites of low-calcium pyroxene. High-calcium pyroxene is often seen as overgrowths on the low-calcium pyroxene microlites.

Recognition of FAB as an inherent component of the fore arc is relatively recent (Reagan et al., 2010). Originally, FAB was thought to have been trapped oceanic crust from the Philippine plate due to its MORB-like geochemical

signature (Johnson and Fryer, 1990; DeBari et al., 1999). However, the magmatic material in the fore arc is an intrinsic product of subduction and has been interpreted as a result of mantle rising to fill the space left by the descending plate, although this is unlikely given that during subduction initiation there is no slab to descend (Stern and Bloomer, 1992; Reagan et al., 2010). FAB could be generated from the extension of the would-be lower plate pulling away from the upper plate (Stern and Bloomer, 1992; Metcalf and Shervais, 2008; Stern et al., 2012). This would cause extension and thinning of the plate, decompressing the mantle below and causing melting. FAB is characterized by its MORB-like geochemical signature and variability of fluid soluble elements, but also by much lower ratios of REE or High-Field Strength Element (HFSE) to V than MORB (Reagan et al., 2010). Low Ti/V and Yb/V ratios suggest that the FAB are more closely related to boninite than MORB (Reagan et al., 2010).

The production of FAB, and later boninite, along the length of the arc simultaneously, suggests that the mantle underwent the same processes along the length of the arc at broadly the same time. FAB is thought to be generated via decompression melting of rising asthenospheric mantle with no input from a subducting slab, implying that this event occurred as the upper plate extended and released pressure on the underlying mantle prior to descent of the lower plate reaching depths required to release fluids (Reagan et al., 2010). Boninite is generated via hydration flux melting of depleted mantle with input from the subducting slab, implying that this event occurred when the subducting plate was at sufficient depth to release fluids (Cameron et al, 1979; Coish et al., 1982;

Hickey and Frey, 1982; Kostopoulos and Murton, 1992; Sobolev and Danyushevsky, 1994; Brenan et al., 1995; Keppler, 1996; Bédard et al., 1998). One possible explanation for the FAB to boninite transition is that the transition records the system change as fluids and sediment melt is driven from the subducting slab.

CORE DESCRIPTIONS

Core descriptions from IODP Expedition 352 are as follows (Reagan et al., 2015). Modal variations occur in all rock types and all core. The existence of phenocrysts is not necessary to define a rock type, but they assist in defining discreet units. Major and trace element variation occurs across samples with MgO and SiO_2 defining the specific rock types FAB, BB, LSB, and HSB.

U1440B

Core U1440B is dominantly FAB with dolerite dikes in the lowermost section (Figure 5). Most of the lava is aphanitic to fine-grained basalt, typically aphyric. Rarely plagioclase and/or augite phenocrysts are present, not exceeding 1% modally. While mineral assemblage rarely changes within the core, chemistry of the lava varies.

Core U1440B is separated into three parts: volcanic extrusive, the transition zone, and dikes. The volcanic extrusive zone consists of FAB, the dikes consist of dolerite, and the transition zone is the change from dike to volcanic extrusive. There is little modal difference down-hole, but the chemistry

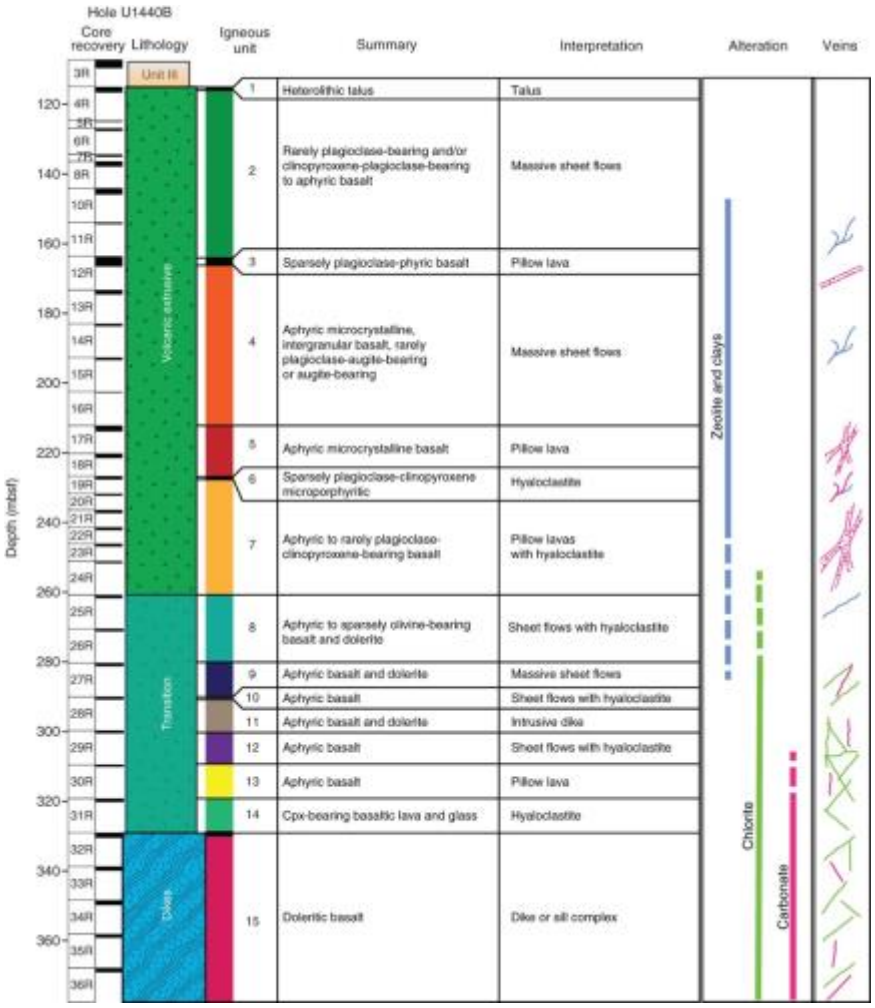

Figure 5. U1440B Core Description. Hole U1440B shipboard stratigraphy with associated units. Units defined by pXRF analysis (mostly TiO_2, Cr, and Ti/Zr) and formation type (sheet flows, pillow flows, breccias, etc.). (Figure from Preliminary Report Reagan et al., 2015)

changes significantly.

Alteration is dominated by clays and to a lesser extent zeolite and calcite. Alteration is variable but generally low except in rare pieces. Some fresh glass remains after alteration. Alteration zones frequently parallel fracture faces and are cut by veins, indicating multiple stages of alteration.

Veins occur through nearly the entire hole, but are absent at the top. Vein-

filling material include: magnesian calcite, zeolites, clays, native copper, and sulfides. Calcite rich veins with angular clasts of host rock are abundant throughout the core.

U1441A

Core U1441A (Figure 6) is dominated by FAB, which is typically aphyric

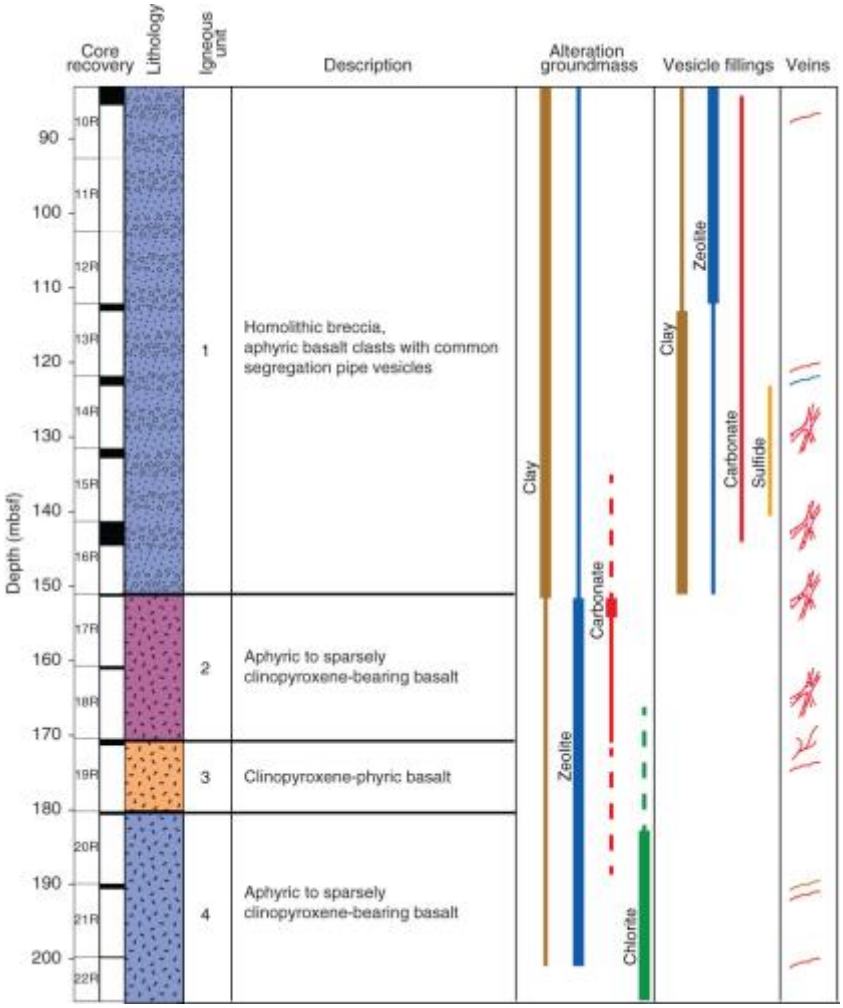

Figure 6. U1441A Core Description. Hole U1441A shipboard stratigraphy with associated units. Units defined by pXRF analysis (mostly TiO_2, Cr, and Ti/Zr) and formation type (sheet flows, pillow flows, breccias, etc.). (Figure from Preliminary Report Reagan et al., 2015)

with rare microphenocrysts of plagioclase, olivine, and orthopyroxene. The groundmass is dominated by plagioclase and clinopyroxene.

Alteration ranges from moderate to high in the uppermost section and decreases down core. Secondary alteration consists of smectite group clays up-section and zeolites down-section. Zeolite is an alteration product of plagioclase, whereas clays are an alteration of clinopyroxene and olivine.

Veins consist of a dense network in a small region of calcite and sporadic, isolated veins of zeolite, clay, or calcite.

U1442A

Core U1442 (Figure 7) is dominated by boninitic lava. The basement section of U1442A consists of boninitic lava and hyaloclastites. The uppermost section is comprised of seafloor colluvium. Core U1442A contains multiple zones of faulting and cataclastite. The faulted region marks a change in lithology and chemistry.

HSB is characterized by olivine and orthopyroxene phenocrysts of euhedral crystals. Orthopyroxene phenocrysts are low-calcium, occurring as single crystals or glomerocrysts. The groundmass consists of pale tan glass with pyroxene microlites of low-calcium and high-calcium pyroxene varieties.

LSB contains some augite (high-calcium pyroxene) phenocrysts within an augite groundmass. No BB was found in ship board tests. HMA contain common augite phenocrysts and rare plagioclase phenocrysts. The groundmass is dominantly plagioclase and augite which may be intergrown. These rocks have

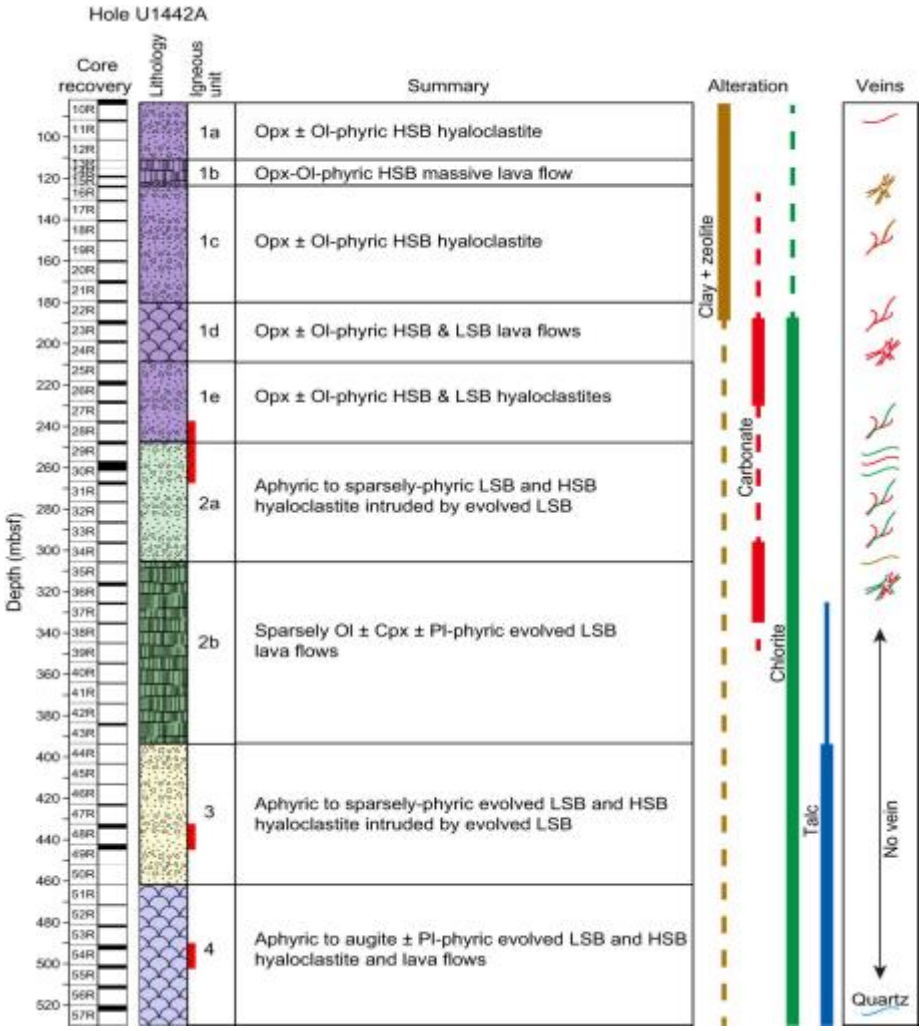

Figure 7. U1442A Core Description. Hole U1442A shipboard stratigraphy with associated units. Units defined by pXRF analysis (mostly TiO_2, Cr, and Ti/Zr) and formation type (sheet flows, pillow flows, breccias, etc.). (Figure from Preliminary Report Reagan et al., 2015)

high magnetic susceptibility unlike other boninites, due to Fe-Ti oxides in the groundmass.

Alteration in core U1442A is highly variable and consists of smectite group clay minerals, zeolites, calcite, and talc at depth. Groundmass and phenocrysts are altered; however, some unaltered glass is preserved as clasts. Veins are not

common in core U1442A and are composed of calcite, clays, and zeolite. A quartz vein was observed near the bottom of the hole.

U1439C

Core U1439C (Figure 8) is dominated by boninitic lava, similar to core U1442A. The base of the hole is characterized by mafic dikes or sills and intercalations of high-magnesium andesite and boninite. The midsection of the hole is dominated by pillow lava with some massive sheet flows, igneous breccias, and pyroclastic flow deposits. The uppermost section of the hole is comprised of heterolithic breccias of seafloor colluvium.

HSB are dominated by orthopyroxene phenocrysts with few olivine phenocrysts. Orthopyroxene phenocrysts appear as blocky euhedral crystals. The groundmass lacks augite and plagioclase.

LSB are dominated by olivine phenocrysts as blocky euhedral crystals and a lesser abundance of orthopyroxene crystals. The groundmass contains augite with or without orthopyroxene cores. BB are dominated by phenocrysts of olivine and high-calcium pyroxene, with less common orthopyroxene. The groundmass contains augite with or without orthopyroxene cores. HMA contain common augite phenocrysts with rare plagioclase and olivine phenocrysts, and the groundmass is dominantly plagioclase and augite which may be intergrown.

Alteration is variable throughout core U1439, with the highest degree of alteration found in the olivine-rich boninites. Phenocryst-rich samples tend to be more altered than the microphenocrysts of aphyric samples. Veins are

abundant in core U1439C. They consist of zeolite or calcite with rare phyllosilicate veins. Veins widen when crosscutting vesicles.

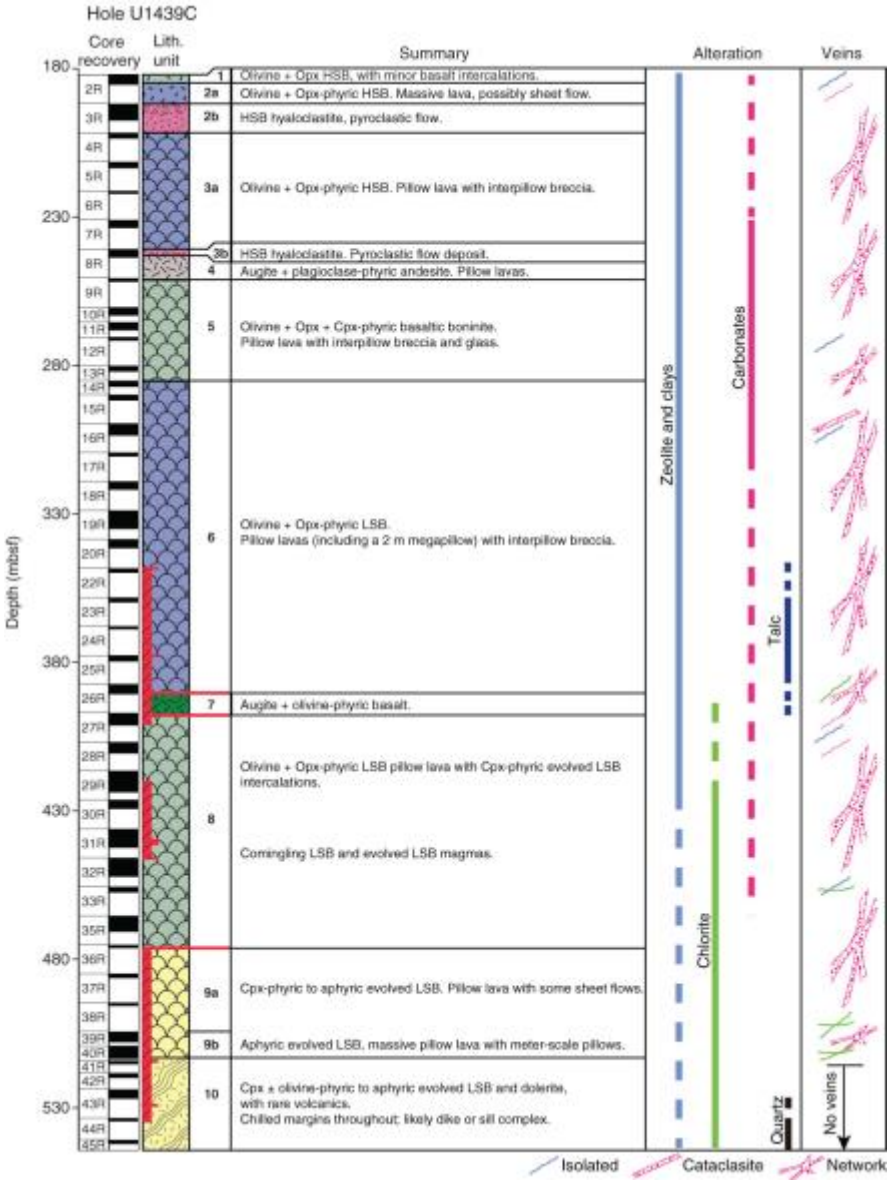

Figure 1. U1439C Core Description. Hole U1439C shipboard stratigraphy with associated units. Units defined by pXRF analysis (mostly TiO_2, Cr, and Ti/Zr) and formation type (sheet flows, pillow flows, breccias, etc.). (Figure from Preliminary Report Reagan et al., 2015)

CHAPTER II

METHODS

Four holes were drilled on an East-West line in the fore arc of the Bonin Islands: U1440B, U1441A, U1442A, and U1439C (Figure 2). From these, 124 core samples were selected for detailed petrologic and geochemical study. The number identifier of the holes corresponds to the order in which they were drilled. Samples were unequally obtained from these holes due to recovery complications of the core. Samples collected include: U1440B = 61 samples, U1441A = 9 samples, U1442A = 20 samples, and U1439C = 34 samples. Samples were collected based on freshness (little to no alteration), geochemical types as determined by shipboard analysis, and to bracket chemostratigraphic unit boundaries as defined by portable X-Ray Fluorescence (pXRF) analysis. In addition to these personal samples, analytical data are available for 112 pool samples.

Sample Preparation and Analysis

The samples were cut to retain a split of the original sample. The other split was then crushed into small gravel sized pieces. The crushed pieces were then washed in an ultrasonic for 15 minutes or until the water ran clear, to remove surface contaminants. The samples dried under heat lamps prior to picking. Picking involved choosing the cleanest, least weathered pieces from the crushed sample. The unweathered samples were then crushed to a powder in a

shatterbox using a tungsten mill for approximately 20 seconds. A split of powder, approximately 1 gram, was reserved for Inductively Coupled Plasma - Mass Spectrometer (ICP-MS) analysis, while the remainder of the powder was used for X-Ray Fluorescence (XRF).

XRF preparation involved heating a fraction of each powder for 4 or more hours at 1,000ºF to drive off volatile elements, typically water, from the sample in a process called Loss on Ignition (LOI). This is performed to ensure that the sum weight that is collected by the machine is accurate and not missing weight that is driven off as the volatiles leave the sample as it is being fused. The ignited powder was mixed with a 1:7 ratio of tetraborate flux to melt the powder into a fused disk. The fused disk was then analyzed on a Panalytical 2400 XRF Spectrometer at Utah State University, Utah, to determine the major element and select trace element concentrations. The XRF was calibrated using a selection of USGS and international rock standards.

The split set aside for ICP-MS was weighed out to 0.050 grams. 3 ml Nitric acid and 2 ml Hydrofluoric acid was added to the vial prior to being placed on a hot plate to dissolve the sample. Watch glasses were used to prevent liquid from evaporating. After 3 hours, or until the sample is completely dissolved, the watch glasses were removed and the liquid was allowed to evaporate, approximately 2-4 hours. When all the liquid evaporated, 30 ml of 5% Nitric acid was then added to the vial at 50ºC overnight. The samples were removed from the hot plate and allowed to cool before filling the vial to 50 ml with 5% Nitric acid. This final mixture was spiked with an internal standard of In-Bi in a secondary vial. The

spiked sample was then run on a Perkin Elmer Elan 9000 quadropole ICP-Mass Spectrometer at Centenary College, Louisiana.

Iron was analyzed as Fe_2O_3 because all iron is oxidized during ignition or during the bead-making process. We convert Fe_2O_3 into FeO by multiplying the conversion factor 0.8998 (molecular weight of FeO/molecular weight of Fe_2O_3). After this conversion, totals must be renormalized to the original total. Some samples were not ignited prior to fusing of the beads, so LOI was added in after the analysis to determine the original total before normalization. The data were normalized to the original sum by multiplying the elements by the Sum+LOI divided by the original Sum. To normalize the samples to 100%, the elements are multiplied by 100 then divided by the new sum using FeO.

Forward Modeling of Mantle-derived Melts

Modeling of melt compositions derived from a mantle source was modified from Jean and others (2010). Source mode and melt mode are taken from Niu (1997) We assumed that the base starting composition was Depleted MORB-source Mantle (DMM) (Salters and Stracke, 2004), mantle asthenosphere composition from which MORB is thought to be derived. Equations for the bulk distribution coefficient of the original solids, bulk distribution coefficients of minerals which make up the melt, pooled melt, and residue are from Rollinson (1993). The final equation, pooled melt from two melt sources, is from Jean and others (2010).

Partition coefficients are the distribution of trace elements between phases

and are determined experimentally (Rollinson, 1993). Most of the partition coefficients used in this study are collected from partition coefficients experiments (Johnson et al., 1990; Hart and Dunn, 1993; Horn et al., 1994; Hauri et al., 1994; McDonough and Sun, 1995; Brenan et al., 1998; Gaetani and Grove, 1998; Johnson, 1998; Walter, 1998; Canil, 1999; Green et al., 2000; Klemme and Blundy, 2002; Gaetani et al., 2003; McDade et al., 2003; Salters and Stracke, 2004; Witt-Eickschen and O'Neil, 2005; Adam and Green, 2006; Elkins et al., 2008; Mallman and O'Neill, 2009). Other partition coefficients were extrapolated using reasonable values from other elements (Jean et al., 2010).

Partition coefficients, Kd, are used to determine the bulk distribution coefficients of the original solids. This is determined by multiplying the Kd for an element in a specific mineral by the source mode for that mineral and adding all the minerals involved (Rollinson, 1993). The equation is as follows:

$$D_i = x_1*Kd_1 + x_2*Kd_2 + x_3*Kd_3 \ldots$$

where Di is the bulk distribution coefficient for the element i, x_1 is the percentage proportion of mineral 1 in the rock, and Kd_1 is the partition coefficient for element i in mineral 1.

The bulk distribution coefficients of minerals that make up the melt have a very similar equation as the bulk distribution coefficient of the original solid with the difference being instead of using the mineral percent proportion, the melt percent proportion is used (Rollinson, 1993). The equation is as follows:

$$P = p_1Kd_1 + p_2Kd_2 + p_3Kd_3 \ldots$$

where P is the bulk distribution coefficient of the minerals that make up the melt,

p_1 is the normative weight fraction of mineral 1 in the melt, and Kd_1 is the partition coefficient for a given trace element in mineral 1.

The minerals of interest for both the bulk distribution coefficients of the original solids (D) and bulk distribution coefficient of minerals that make up the melt (P) are olivine, orthopyroxene, clinopyroxene, spinel, and garnet. Melts involving spinel and garnet are exclusively one or the other. This is because garnet is a deep mantle mineral: below 2.8 GPa, or <85 km depth, garnet transforms into spinel (Robinson and Wood, 1998).

Pooled melt is a type of fractional melt where the incremental melts have collected instead of leaving the system. The equation is as follows:

$$C_L = (C_O/F) * (1-(1-((P*F)/D) \text{ ^}(1/P))$$

where C_L is the melt, C_O is the starting composition, F is the fraction of melt, P is the bulk distribution coefficient of minerals that make up the melt, and D is the bulk distribution coefficient of the original solids.

The melt residue is the remaining material of the starting rock composition after an amount of melt has been removed from it. This residue is often used as the starting composition of other melt models when DMM is not accurate or the model calls for melt after another melt based on DMM. The equation is as follows:

$$C_R = (C_O/(1-F)) * (1-((P*F)/D) \text{ ^}(1/P))$$

where C_R is the residue and C_O, F, P, D are defined above.

The final equation is the pooled melt from two melt sources. This equation is used when combining two melts, such as a fraction of garnet melt mixing with

a fraction of spinel melt. The equation is as follows:

$$((F_{M1}/(F_{M1}+F_{M2})) * M1_{melt}) + ((F_{M2}/(F_{M1}+F_{M2})) * M2_{melt})$$

where F_{M1} is the melt fraction of the first melt and F_{M2} is the melt fraction of the second melt: $M1_{melt}$ is the composition of the first melt, and $M2_{melt}$ is the composition of the second melt.

Most models in this study are pooled melt from two melt sources. By removing a previous melt, a depleted residue remains that then becomes even more depleted when it is melted again. This model is severely depleted in LREE. As such, it is necessary to pool two melts to bring the values up to match a sample.

Source mode and melt mode determine the likelihood of a mineral forming or remaining in the melt (Niu, 1997). These vary for spinel and garnet melts, as well as for composition of the mantle. Spinel is the alumina-rich phase at pressures >27 kb (although Cr-spinel and garnet fields may overlap). Lherzolite (olivine + orthopyroxene + clinopyroxene ± spinel or garnet) and harzburgite (olivine + orthopyroxene +/- spinel or garnet) are the two mantle modal compositions considered in these models. Lherzolite mantle is fertile and produces MORB-type extrusive rocks. Harzburgite is depleted relative to lherzolite and is considered the residue after melt extraction from lherzolite. Due to the MORB-like character of FAB, lherzolite source mode and melt mode is modeled first, then harzburgite is modeled when lherzolite melt is depleted. Clinopyroxene is exhausted at approximately 28% melting in the spinel lherzolite field.

CHAPTER III

RESULTS

Major element concentrations change with the evolution of the reservoir and with recharge of the reservoir. The fractionation of major elements is dependent on the minerals crystallizing. Elements indicating evolution of the reservoir include decreasing Mg and increasing Si (Figure 9). Elements that vary with minerals being produced include Fe, Al, and Na. The major element K can be used as an indication of alteration, with higher concentrations suggesting more alteration. Ca is variable in boninites due to the presence or absence of clinopyroxene crystallizing. However, it can be used as an indicator for reservoir evolution with high Ca indicating primitive magma (Pearce et al., 1992).

Fractionation may be traced throughout the core retrieved from IODP Expedition 352 by tracking SiO_2, MgO, FeO, Al_2O_3, Na_2O, Ti, and Zr. Cores U1440B and U1439C display evidence for “recharge” and “fractionation” due to the large number of samples analyzed. Evidence for fractionation is lacking in cores U1441A and U1442A due to sparse samples. Recharge and fractionation are used tentatively here to mean more primitive and more evolved than surrounding samples. Recharge and fractionation apply to a single reservoir; however, these samples are most likely from multiple sources and reflect the overall change of the system.

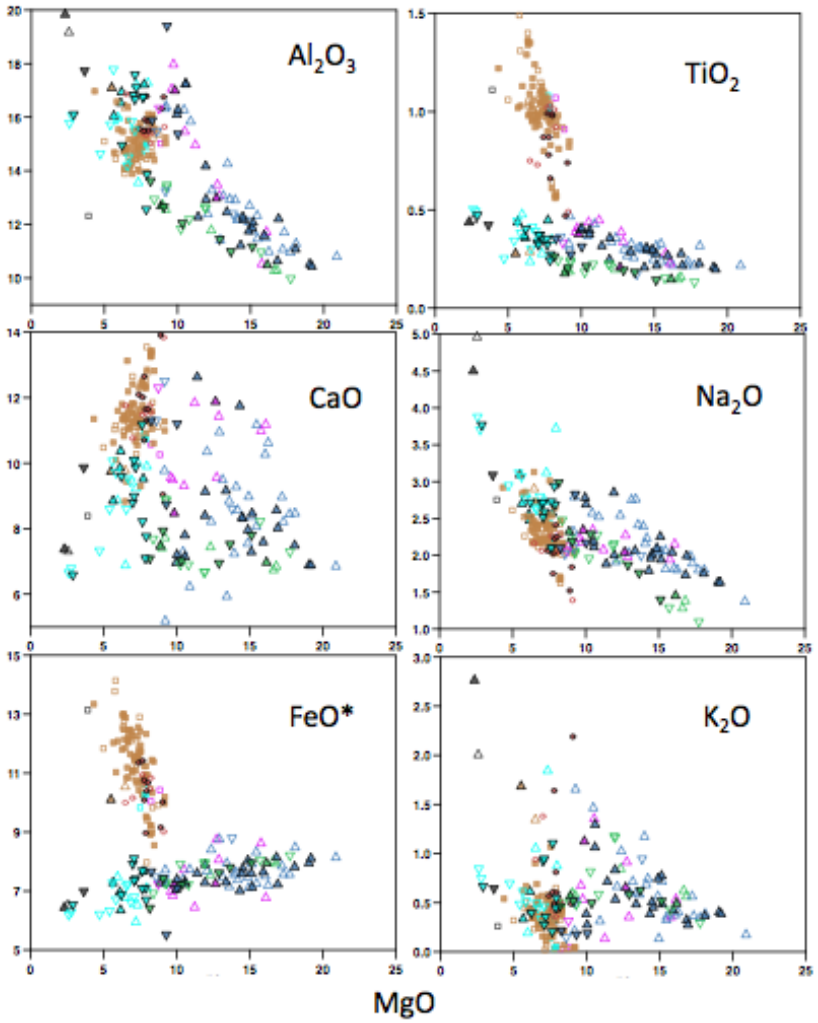

Figure 9. MgO major element discrimination diagrams. Symbols same as Figure 4 (Appendix A).

PETROLOGY

FAB

The major minerals that comprise FAB in cores U1441A and U1440B are plagioclase, and pyroxene with some olivine, like MORB (Reagan et al., 2015). Olivine controls the elements Mg and Fe. Plagioclase controls the elements Na, Ca, and Al. Depending on the type of pyroxene present, clinopyroxene controls

the elements Ca, Mg, Fe, and Al while orthopyroxene controls the elements Mg and Fe. Thus, FAB should have relatively high concentrations of Mg, Fe, Al, Ca, and moderate Na. Evolution pathways should show decreasing Mg, Fe, Al, and Ca as these minerals crystallize.

Boninite

The major minerals that comprise boninite are olivine and pyroxene, contributing to the high MgO content. Boninite is notably lacks in plagioclase. This is because water suppresses plagioclase crystallization. HSB in cores U1439C and U1442A typically have low-calcium orthopyroxene and olivine (Reagan et al., 2015). LSB in cores U1439C and U1442A typically have clinopyroxene and olivine (Reagan et al., 2015). BB in core 1439C typically has olivine and high-calcium clinopyroxene (Reagan et al., 2015). In terms of Ca content, BB is the most primitive and HSB is the most evolved form of boninite from pyroxene type present. Evolution of boninites should have pathways decreasing in Mg and Fe with moderate decrease in Ca. Other major elements will increase content because they are not being used to form the main minerals present.

Other

In addition to the FAB and boninite, there are two other lava types present: High Magnesium Andesite (HMA) and normal andesite (Figure 4). HMA is plotted below 8% MgO on the MgO-SiO_2 discrimination diagram within the curve. Normal andesite plots outside the curve and above 52% SiO_2 and appears at the very

base of U1439C. HMA is considered to be evolved LSB from olivine fractionation curves suggested in Figure 4 with increasing SiO_2 and decreasing MgO (Reagan et al., 2015). The focus of this research is on FAB and boninite, and as such, the chemostratigraphy will be dependent on these entities. The focus of this research is on the FAB and boninite, however there are units defined by the shipboard stratigraphy that are comprised purely of HMA or andesite, so they are included in the diagrams, but not in the discussion.

GEOCHEMISTRY OF FAB AND BONINITE

Several major and trace elements were chosen to plot due to the variation between units, as well as ratios indicating amount of slab derived material influence. Pool samples from Godard and others (in prep.) serve as support to the personal samples analyzed here. Pool samples plot as open unfilled symbols and the personal samples analyzed for this thesis plot as filled symbols. In most cases, the pool samples and samples analyzed in this study plot on top or very near each other in Figures (9-22). Deviation of analysis arises from difference in the instrument used, not the samples necessarily.

Major Elements

FAB are characterized by higher CaO, FeO, and TiO_2 than boninite, whereas Al_2O_3 is about the same at similar MgO contents (Figure 9). FeO and TiO_2 increases with decreasing MgO, which indicates control by plagioclase and olivine fractionation. Na_2O does not change with decreasing MgO, reflecting

similar levels in both the melt and the fractionating assemblage. Alumina and CaO both decrease with decreasing MgO, which also indicates control by plagioclase and olivine fractionation.

Boninites were divided by Reagan et al. (2015) into three categories using the MgO-SiO_2 discrimination diagram (Figure 4). The slopes of these boundaries are based on olivine-control lines and define groups of samples that could be related by fractional crystallization. High Silica Boninites (HSB) are those samples with greater than 8% MgO and within the boundary SiO_2 = 53 wt% at MgO = 20 wt% and SiO_2 = 58 wt% at MgO = 8 wt%. Low Silica Boninites (LSB) have greater than 8% MgO and fall within the boundaries: SiO_2 = 53 wt% at MgO = 20 wt% and SiO_2 = 58 wt% at MgO = 8 wt% (Upper), and SiO_2 = 50 wt% at MgO = 20 wt% and SiO_2 = 54 wt% at MgO = 8 wt% (lower). Basaltic Boninites (BB) have greater than 8% MgO and fall within the boundary: SiO_2 = 50 wt% at MgO = 20 wt% and SiO_2 = 54 wt% at MgO = 8 wt% (upper); and SiO_2 = 48 wt% at MgO = 20 wt% and SiO_2 = 52 wt% at MgO = 8 wt% (lower).

Pearce and others used the CaO/Al_2O_3 ratio to define three boninite units within the Izu-Ogasawara and Mariana fore arc (Crawford et al., 1989; Pearce et al., 1992; Arculus et al., 1992). Using their method, we find that there is a tenuous connection with low-Ca boninite correlated with HSB, intermediate-Ca boninite with LSB, and High-Ca boninite with BB (Figure 10). Low-Ca boninites are interpreted to have been generated from a more depleted source than High-Ca boninites which is similar to HSB being more depleted than BB here (Deschamps and Lallemand, 2003). However, for this thesis boninite samples

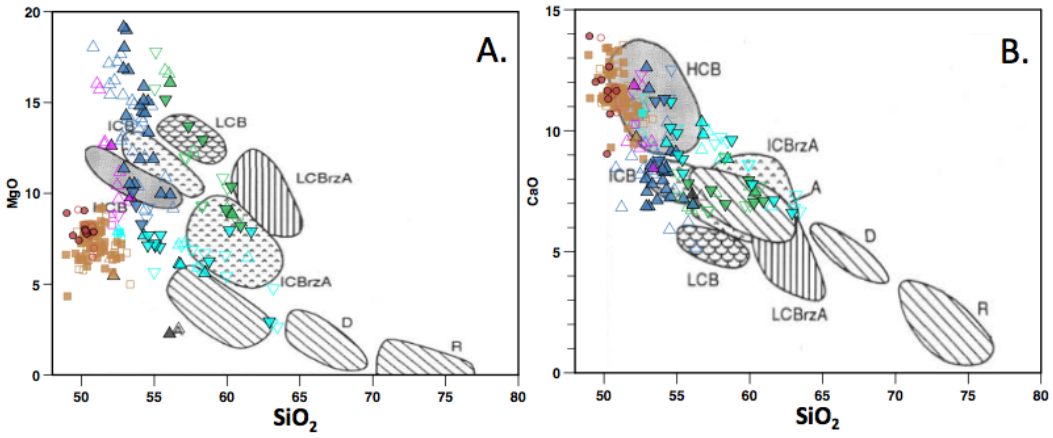

Figure 10. High-, intermediate-, and low-Ca boninite. Fields as defined by Pearce et al., 1992. Generally, HSB plots within the low-Ca boninite range, LSB within the intermediate-Ca boninite range, and BB within the high-Ca boninite range. A. MgO vs SiO2. B. CaO vs SiO2. Symbols same as Figure 4 (Appendix A). (Figure modified from Pearce et al., 1992)

are discriminated into HSB, LSB, and BB for continuity from IODP Expedition 352 reports (Reagan et al, 2015).

Boninites are characterized by lower FeO, CaO, and TiO_2 than FAB (Figure 9). Decreasing FeO with decreasing MgO indicates control by mafic mineral crystallization because mafic minerals use FeO and MgO which leaves the magma depleted in these elements. In contrast, TiO_2 increases slightly with decreasing MgO, which shows that fractionating mafic minerals had a very low Ti content because Olivine has no TiO_2 and orthopyroxene has very low TiO_2 content, thus enriching the magma chamber in TiO_2. Na_2O and Al_2O_3 both increase with decreasing MgO, reflecting the lack of plagioclase in the fractionating assemblage. CaO in boninite in general plots below FAB concentrations with a slight increase in decreasing MgO.

Alteration by seawater post-eruption affects many of these major

elements, in particular K_2O and Na_2O. Na_2O and, to an extent, CaO are only slightly affected by this alteration so that trends in the data are useful, but the absolute values may not be reflecting only the source. K_2O variation gives an indication of alteration amount with higher values having more alteration, but the exact amounts are unknown.

Trace Elements

Key trace elements of interest include Sr, Ba, Cr, Zr, Hf, La, and Sm. Sr and Ba are notably fluid mobile elements and an indicator of slab input and/or seawater alteration. Sr and Ba are generally not as easily enriched through seawater alteration as other more susceptible elements such as Rb, K, or U (Staudigel et al., 1996). Cr, Zr, and Hf are HFSE where primitive magmas have generally high Cr and low Zr and Hf (Rollinson, 1993). La, a light-REE, and Sm, a medium-REE, are REE that are generally immobile, however the light-REE are more mobile than medium-LREE and have a higher tendency to be added to a melt from sediment input from a descending slab (Rollinson, 1993).

Ratios of trace elements allow us to determine how much of the trace elements are added from a slab input or from primitive melt. Low Ti/Zr and Zr/Sm ratios indicate slab melting in the presence of residual amphibole (Taylor et al., 1994). Low Ti/Zr indicates a high degree of melting, or melt from a depleted source (Reagan et al., 2015). High Ba/La ratios indicate sediment input in the form of Ba compared to the relatively immobile La with arc basalt values >20 (Morris and Hart, 1983). Th/La is another indicator of subducted sediment melt

influence on the magma in the form of high temperature mobile Th compared to less mobile La. Elevated Sr/Zr suggest subduction influence in terms of fluid mobile Sr. Ti/V reflects subduction component as water-enhanced melting of the source (Shervais, 1982).

Ti/V diagram is sectioned into separate fields corresponding to a type of volcanic based on the Ti/V ratio. With island-arc basalts plotting between 10 and 20 and MORB plotting between 20 and 50 (Figure 11). Nearly all FAB fall within the island-arc field between 10 and 20, indicating that water is present in the genesis of these samples. Boninites overlap the 10 Ti/V line with HSB falling on <10 and the rest >10 within the island-arc field. The lower the Ti/V ratio, the more water present in the source when melting occurred.

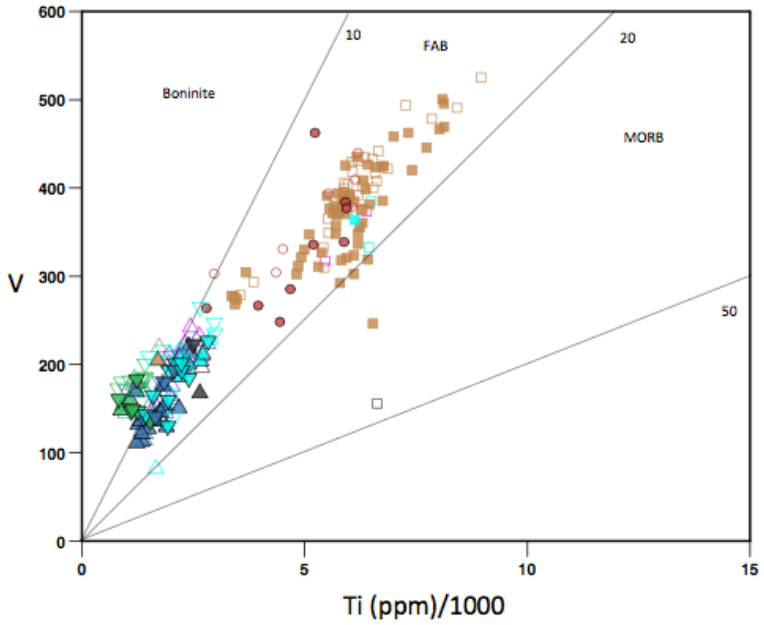

Figure 11. Ti/ V diagram. Low ratios indicate water present during genesis. Symbols same as Figure 4 (Appendix A).

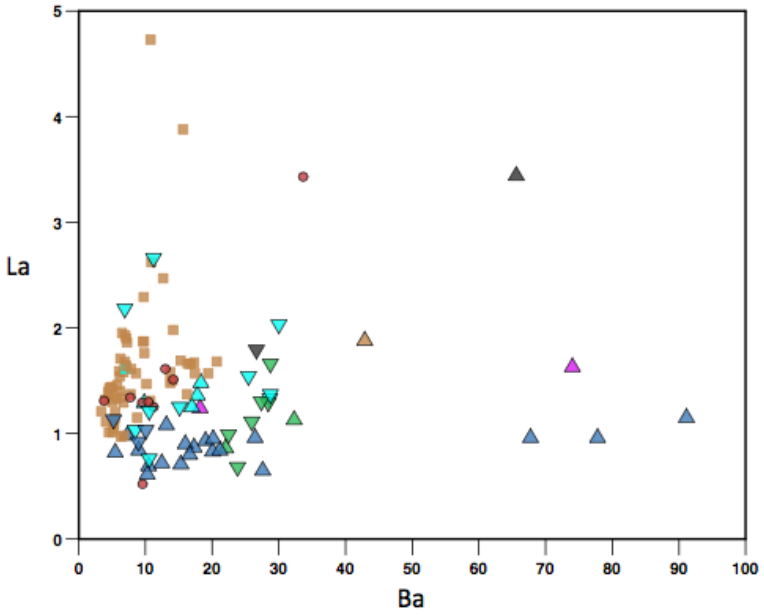

Figure 12. Ba/La diagram. Ba is fluid mobile and La is not. Symbols same as Figure 4 (Appendix A).

Ba/La diagram shows a low amount of Ba present in most of these samples (Figure 12). FAB have typically higher La than boninite and boninite has higher Ba than FAB. HSB samples have in general the highest Ba, reflecting the presence of more subduction competent than other samples. La in boninite does not necessarily reflect the source values due to enrichment from sediment and/or slab melt as seen by the REE diagrams.

Sr/Zr v. Ti/Zr diagram shows a distinct separation of the FAB and boninite due to plagioclase fractionation (Figure 13) (Reagan et al., 2015). Higher Sr/Zr indicates subduction input, while Ti/Zr indicates higher degrees of melting. Plagioclase fractionation affects this diagram by raising Ti/Zr and lowering Sr/Zr, as we see with the FAB.

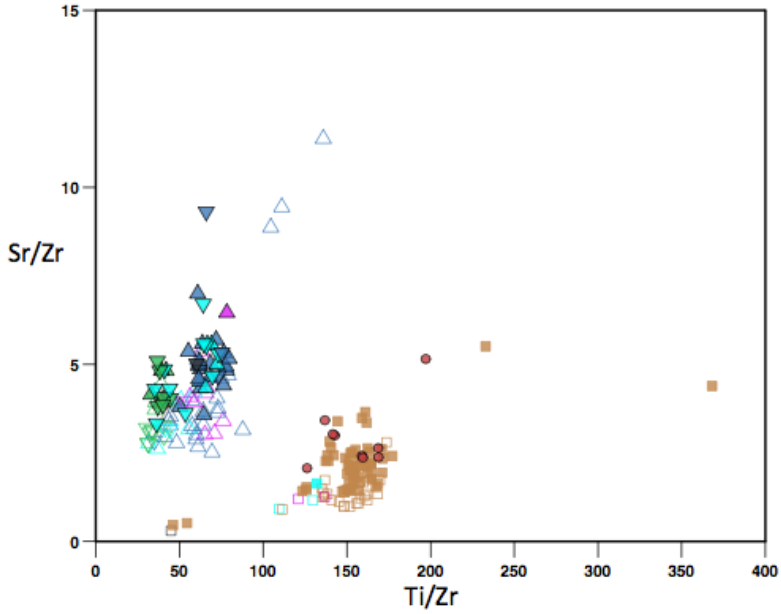

Figure 13. Sr/Zr vs. Ti/Zr diagram. FME Sr compared to HFSE element Ti. Symbols same as Figure 4 (Appendix A).

Sm/Zr diagram shows a clear separation of FAB and boninite samples (Figure 14). Boninites have higher Zr and lower Sm than FAB. Zr is likely elevated in Boninites from a subduction input while Sm reflects the original source composition. Sm reflects the original source composition and degree of melting with low values indicating higher degrees of melting.

The Ti/Zr ratio follows Si content with low Ti/Zr ratios reflecting high Si. Within the Ti/Zr diagram there is a clear separation between FAB and boninite in general, and another separation of HSB and the other boninites (Figure 15). The Zr content for all samples are roughly the same, while boninite Ti content is much lower than FAB.

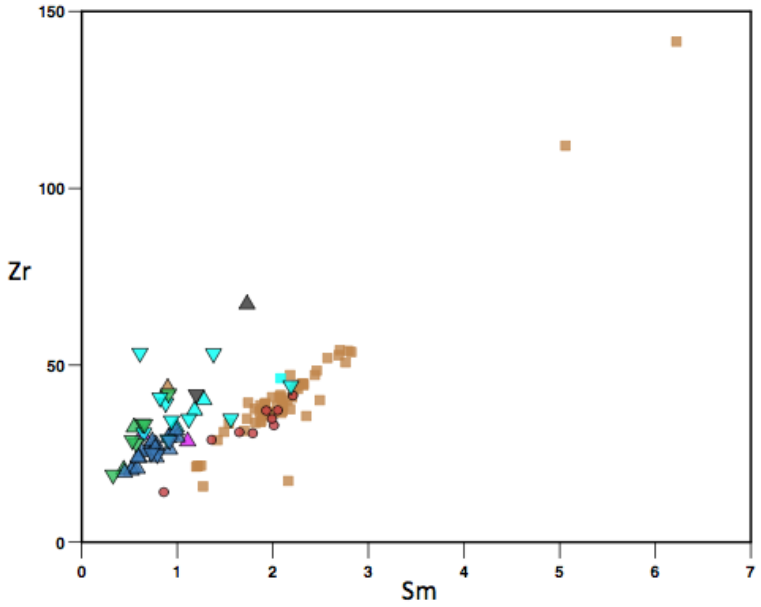

Figure 14. Sm/Zr diagram. Zr is a HFSE and SM is a MREE. Symbols same as Figure 4 (Appendix A).

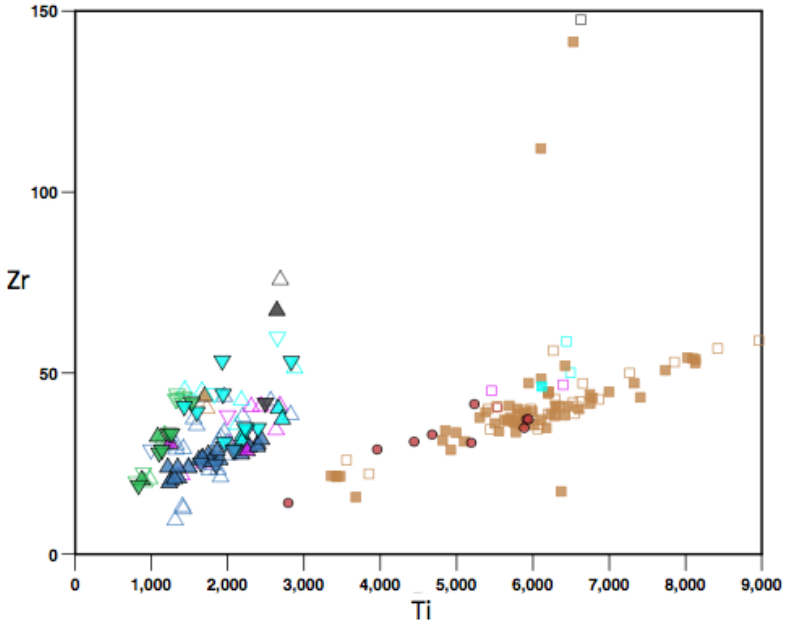

Figure 15. Ti/Zr diagram. The Ti/Zr ratio was used as a substitute for SiO_2. Symbols same as Figure 4 (Appendix A).

REE Diagrams

Rare Earth Element (REE) diagrams show the depleted nature of most samples compared to N-MORB (Figure 16-17). Low REE values indicate a primitive nature of the volcanics. LREE and some MREE are melt mobile, however the HREE are a good indicator of the original source composition.

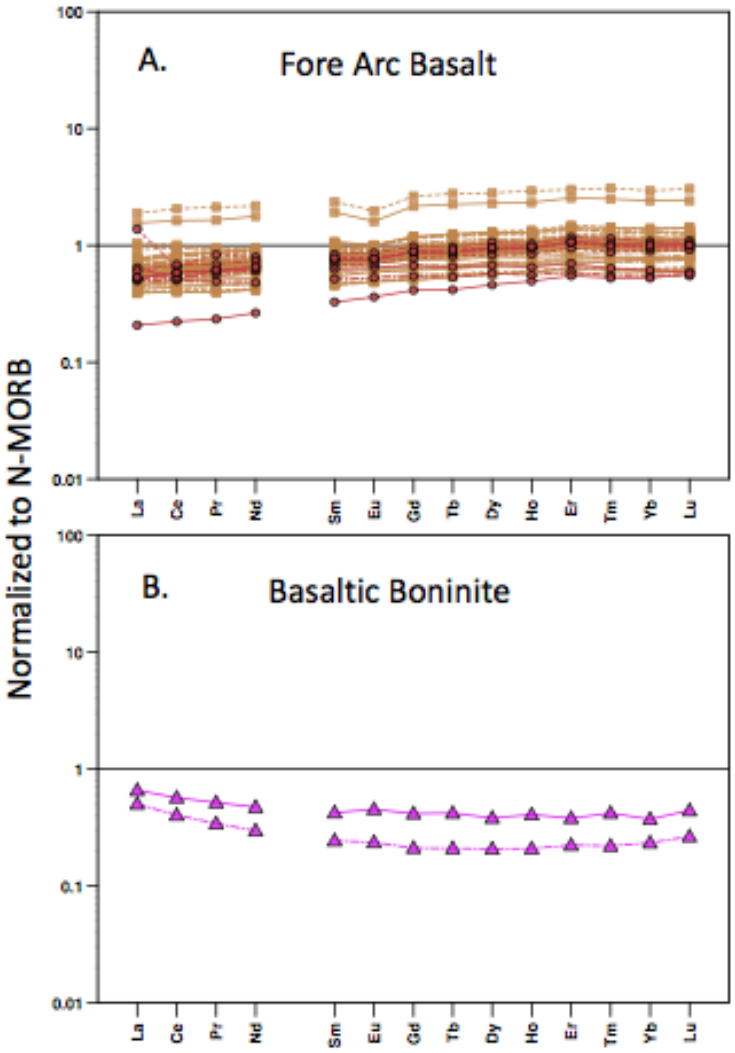

Figure 16. Rare Earth Element Diagrams of all FAB and BB samples. Unfilled symbols are pool samples from Godard et al., in prep. Two enriched samples in FAB are andesite. BB displays U-shaped pattern typical of boninite. Symbols same as Figure 4 (Appendix A).

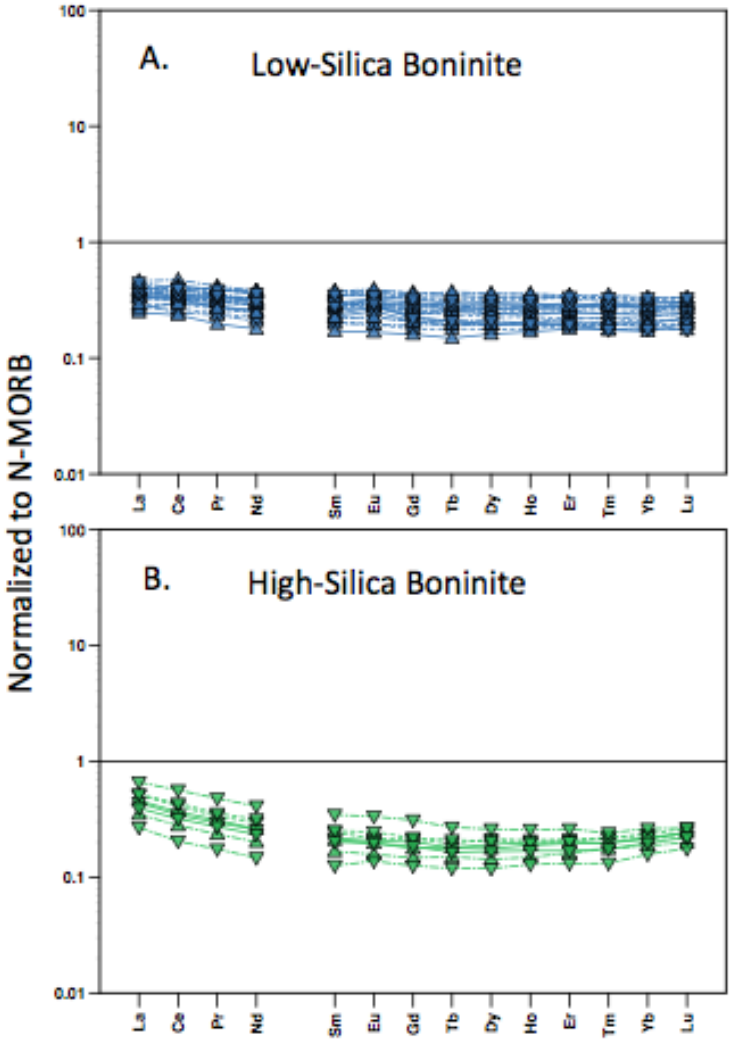

Figure 17. Rare Earth Element Diagrams of all LSB and HSB samples. Unfilled symbols are pool samples from Godard et al., in prep. LSB has slight U-shaped pattern typical of boninite. HSB has a better defined U-shaped pattern. Symbols same as Figure 4 (Appendix A).

FAB are typically more depleted in LREE-MREE than N-MORB, one sample is considered Depleted FAB (DFAB) (Figure 16A). The HREE for the most primitive FAB is depleted relative to N-MORB, but as the magma evolves, the HREE is comparable to N-MORB. The Two samples that are enriched relative to N-MORB on this diagram are andesite from Unit 6 of core U1440B.

The boninites display a U-shaped to slightly curved REE pattern characteristic of boninites with high LREE/HREE ratios. This pattern reflects the depleted nature of the source in low HREE and a subduction input for the elevated LREE while the relatively immobile MREE remain depressed. LREE is added to the boninite melt by either sediment melt form the subducting plate or by small amounts of slab melt.

There are only two BB samples with REE data (Figure 16B). These samples are not as depleted as LSB and HSB, indicating that not as much melting was required to produce these samples (Figure 17). They are depleted relative to N-MORB and the FAB from Figure 16A. LSB samples are more depleted than BB, but have a flatter REE pattern than the characteristic U-shape (Figure 17A). This indicates that there was not a great amount of subduction input, but there was enough to flatten the REE pattern. HSB samples have higher amounts of LREE than either of the other boninite types (Figure 17B). This indicates a greater amount of subduction input than the others. HSB are more depleted than LSB, making these samples the most depleted of the samples analyzed.

Spider Diagrams

Spider diagrams for each of the four rock types explored here show Fluid Mobile Element (FME) enrichment in all samples (Figures 18-19). FME include the trace elements: Rb, Ba, Th, U, K, Pb, and Sr. Many samples are varied and some FME are comparable or depleted relative to N-MORB, however, on

average, FME are enriched relative to N-MORB. This enrichment may come from a subduction component or from seawater alteration post eruption.

In most samples, High-Field Strength incompatible Elements (HFSE) are depleted relative to N-MORB. HFSE include the elements: Nb, Zr, Hf, and Ti. These elements reflect the original source composition and any enrichment is

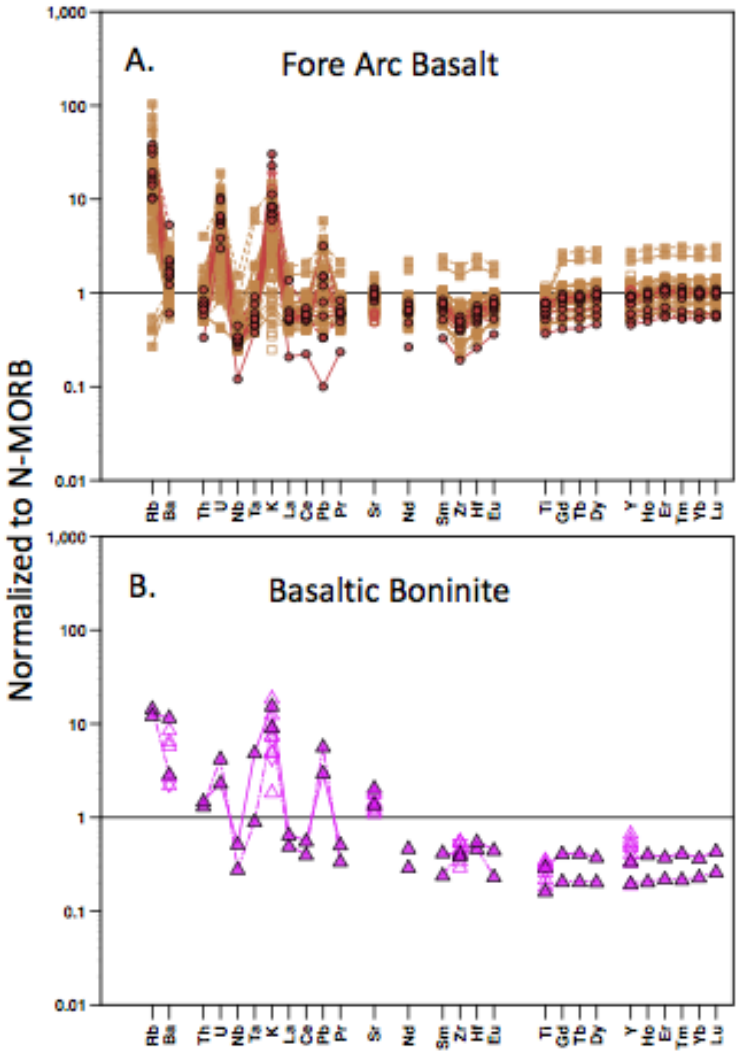

Figure 18. Spider Diagrams of all FAB and BB samples. Fluid Mobile Elements Rb, Ba, Th, Sr, K, and Pb. High Field Strength Incompatible Elements Nb, Zr, Hf, and Ti. Unfilled symbols are pool samples from Godard et al., in prep. Symbols same as Figure 4 (Appendix A).

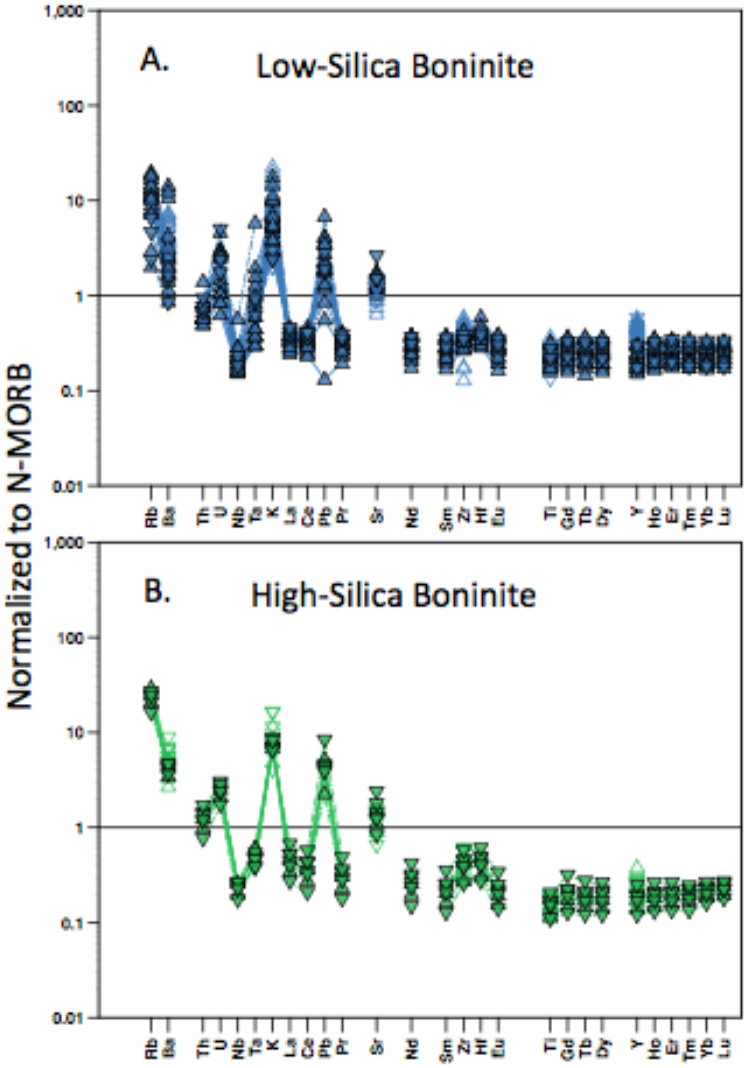

Figure 19. Spider Diagrams of all LSB and HSB samples. Fluid Mobile Elements Rb, Ba, Th, Sr, K, and Pb. High Field Strength Incompatible Elements Nb, Zr, Hf, and Ti. Unfilled symbols are pool samples from Godard et al., in prep. Symbols same as Figure 4 (Appendix A).

due to a melt being added to the magma. This melt could be a subduction component melt consisting of sediment and some basaltic crust from the down-going slab. Alternatively, these elements may be added via a secondary melt. In these spider diagrams, relative to N-MORB, HFSE are depleted, indicating a depleted source.

CHEMOSTRATIGRAPHY

A preliminary stratigraphy was generated on the ship during the cruise (Figures 5-8). This preliminary data was collected using a Portable X-Ray Fluorescence (pXRF) instrument. The pXRF cannot analyze light elements, so this stratigraphy was determined based on the elements in the range of magnesium to uranium. Analysis of the samples using XRF and ICP-MS allows for a more detailed stratigraphy (Appendix B [Tables 1-4]). These analyses collectively show the evolution of the fore arc over time, with increasingly evolved or primitive lavas being produced.

Units were chemically defined based on three main elements: Cr, Ti, and Zr; in some cases, Sr was used if a unit had unusual concentrations. Appendix D is a comparison of shipboard unit definitions and supporting geochemical analysis from XRF and ICP-MS. Not all units are characterized with shore-based XRF and ICP-MS due to lack of samples. Several other elements were considered in further defining these units, however there is much overlap between units and actual unit lines tend to be derived from the lithology.

U1440B

The base of core U1440B (Unit 15) was interpreted to be a dike or sill complex, and is characterized by large variation in the major elements (Figures 20-21). Trace elements TiO_2, Zr, and Sr are roughly the same with little scatter. The next section of the core is known as the transition zone and is comprised of Units 8-14 with alternating sheet flows and one intrusive dike. This zone is

characterized by a lot of scatter in major elements and similar trace elements to the dike and sill complex.

SiO_2 decreases from Unit 7 to Unit 3, where it experiences scatter, then an increase in Unit 2 and more scatter in Unit 1. MgO follows SiO_2 trend. Na_2O,

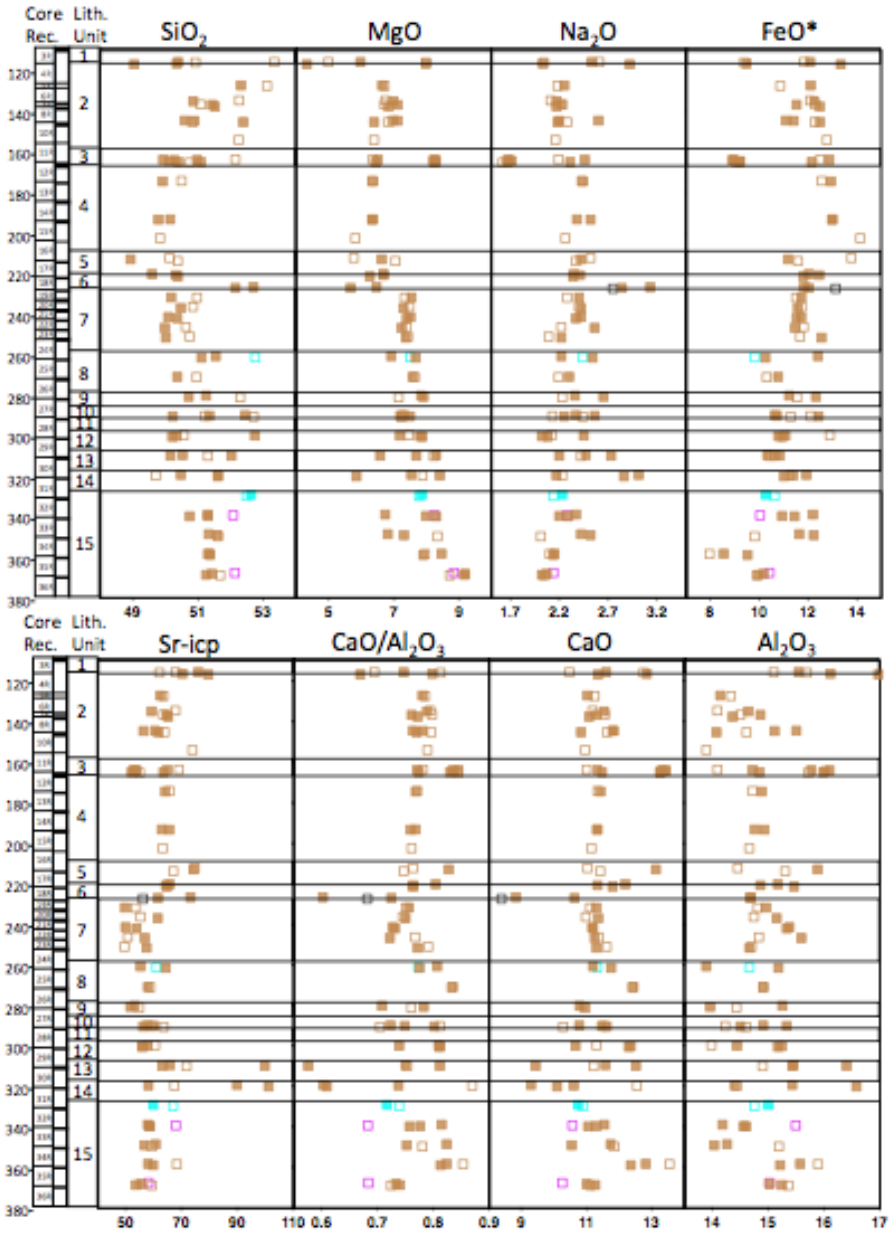

Figure 20. U1440B Depth plots. Unfilled symbols are pool samples from Godard et al., in prep. Symbols same as Figure 4 (Appendix A).

Al_2O_3, and FeO trend opposite SiO_2 and Mg with increasing concentrations up section to Unit 3, then decreasing in Units 2 and 1. CaO remains relatively stable.

Up section in Unit 7 samples reflect fractionation of the magma chamber with increasing TiO_2 and decreasing Cr and Al_2O_3. Other elements remain

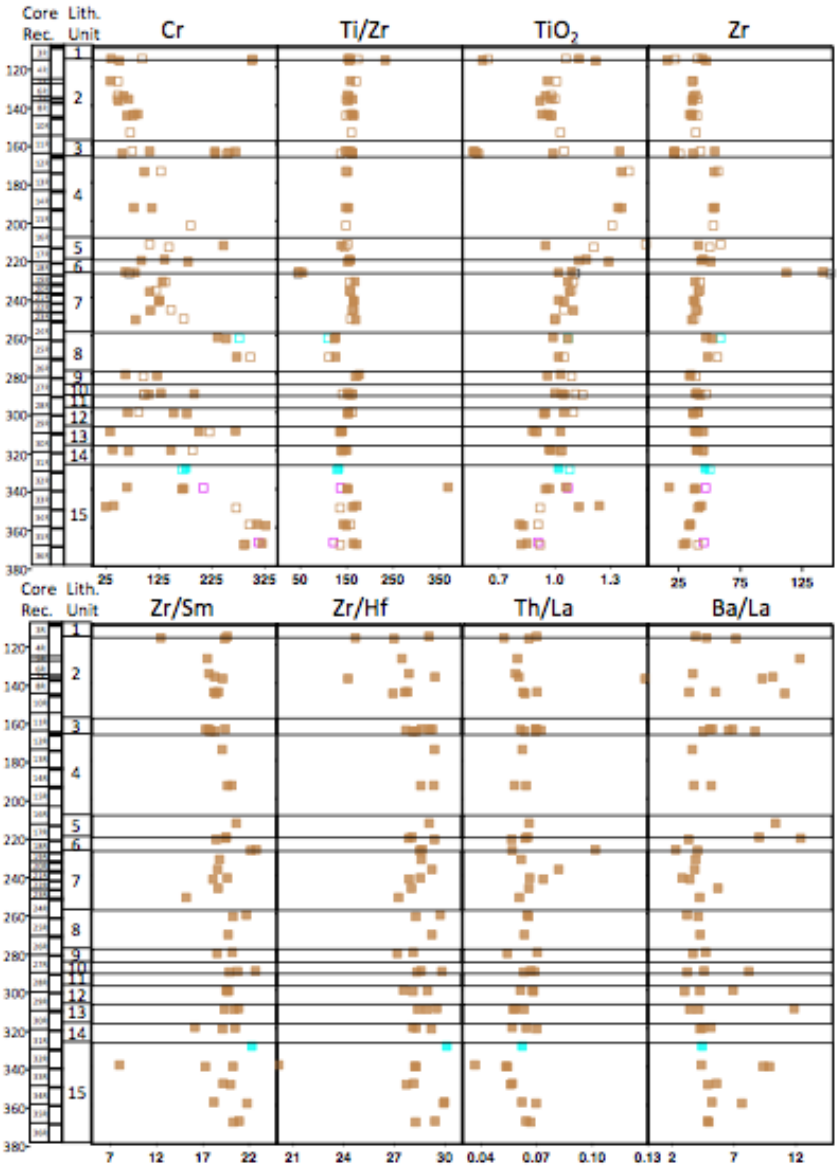

Figure 21. U1440B Depth plots. Unfilled symbols are pool samples from Godard et al., in prep. Symbols same as Figure 4 (Appendix A).

relatively stable. Evolution of the magma continues with increasing TiO_2 up section to Unit 3 where the samples shows scatter possibly due to magma mixing. The next Units have lower TiO_2, indicating a recharge of the magma chamber. Zr mirrors TiO_2 but with less extreme variation. Cr decreases from Unit 7, reflecting evolution of the magma chamber, with variation in Units 5, 6, and 1.

Unit 3 is a pillow lava with scattered concentrations, indicating magma mixing (Figures 20-21). Other units displaying scatter are talus (Unit 1) and hyaloclastites (Unit 6) suggesting the scatter is due to a post eruption combining of the lithology and not a magma mixing event.

U1441A

Core U1441A displays considerable variability up section and several instances of recharge and fractionation seen in major elements (Figures 22-23). SiO_2, Na_2O, TiO_2, and FeO decreases as MgO, CaO, and Al_2O_3 increases through Unit 3. Up section, through Unit 2, concentrations switch with increasing SiO_2, Na_2O, TiO_2, and FeO and decreasing, MgO, CaO, and Al_2O_3. Unit 1 has both recharge and fractionation as MgO increases then decreases near the top.

Zr follows TiO_2 patterns and is opposite Cr concentrations. Ba/La peaks in Unit 3 before decreasing to a stable level. Th/La peaks in Unit 2 before dropping drastically through Unit 1. Zr/Hf and Zr/Sm decreases through to Unit 2 before increasing through Unit 1. Sr has moderate levels at the base of the core, decreases through Unit 3 the increases rapidly through Unit 2 to a steady, high

level in Unit1.

Unit 3 consists of the depleted FAB (DFAB) sample. It has lowest SiO_2, Na_2O, FeO, and TiO_2, with highest MgO, CaO, and Cr. It also has the highest Ba/La ratio indicating subduction input, but lowest Sr, possibly reflecting less alteration post-eruption than surrounding samples.

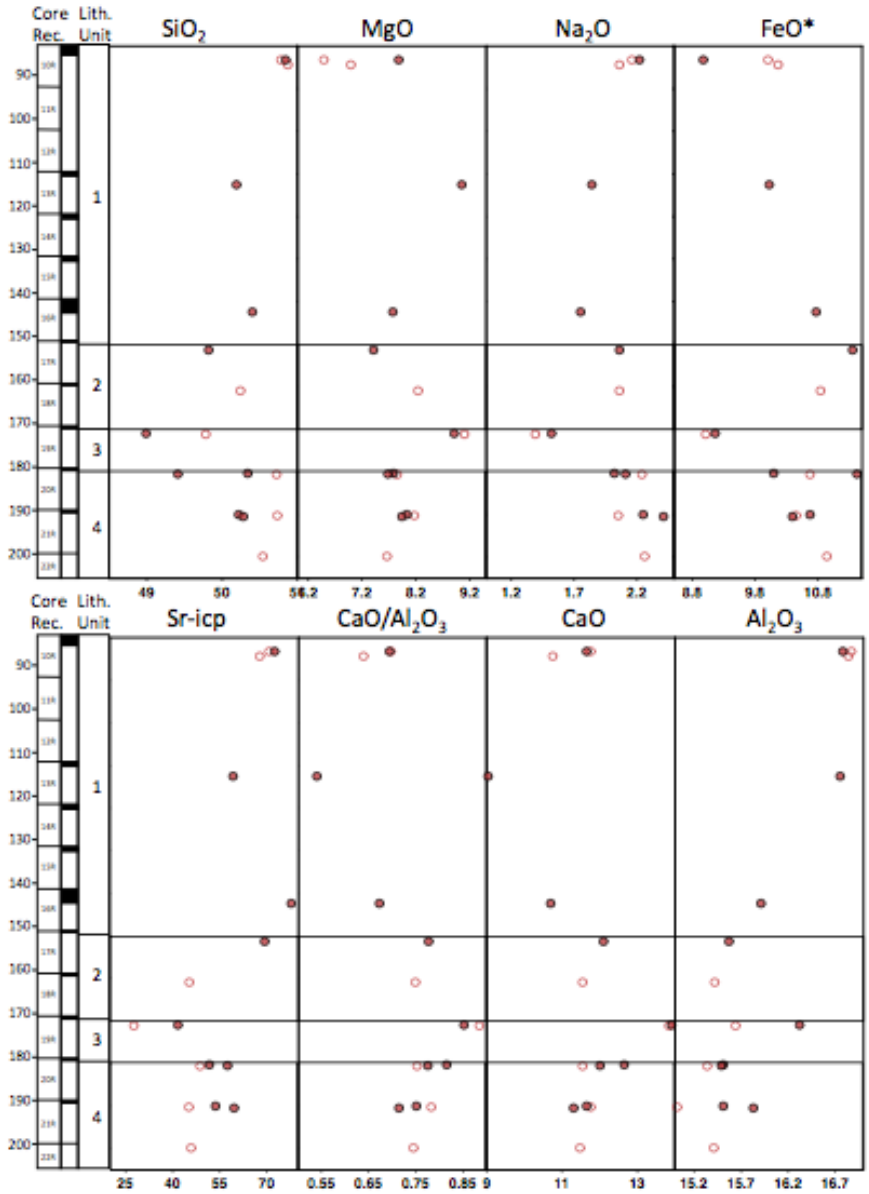

Figure 22. U1441A Depth plots. Unfilled symbols are pool samples from Godard et al., in prep. Symbols same as Figure 4 (Appendix A).

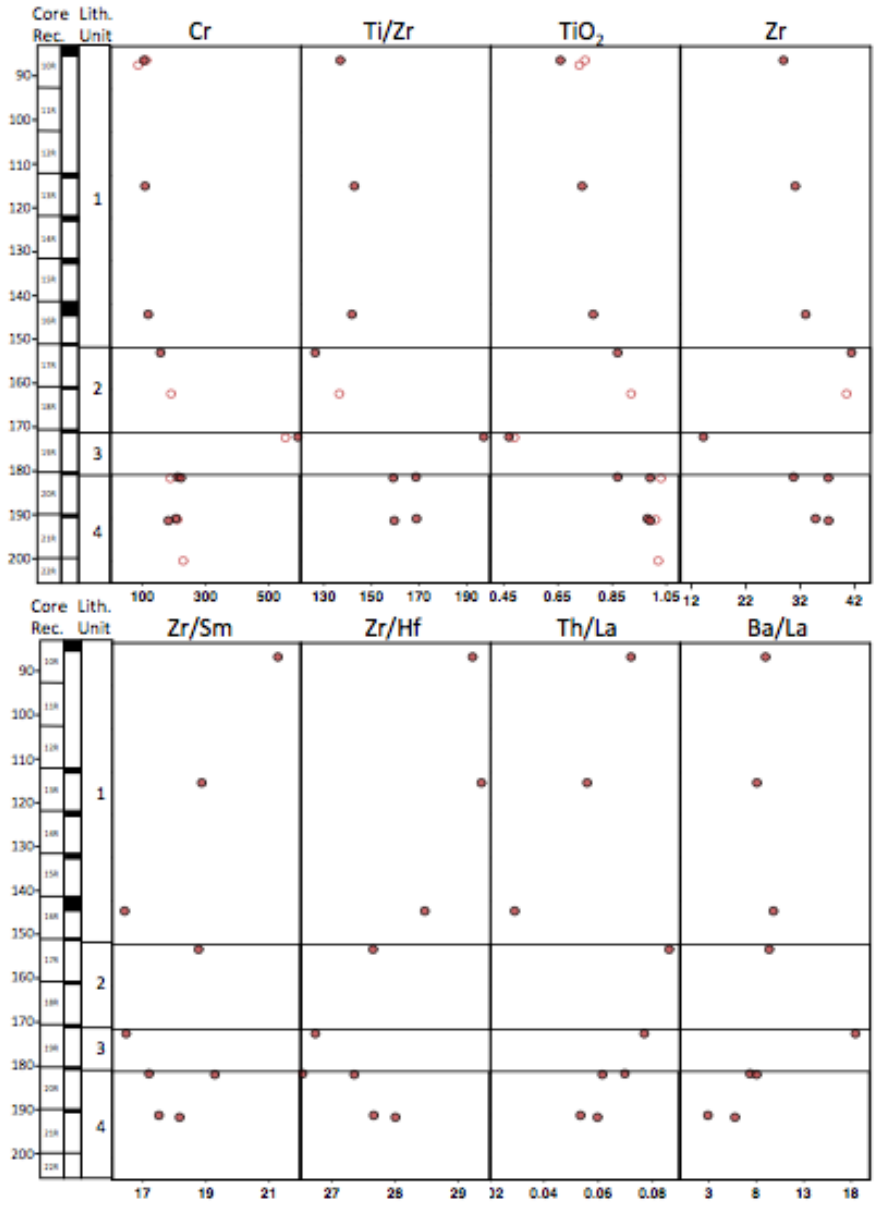

Figure 23. U1441A Depth plots. Unfilled symbols are pool samples from Godard et al., in prep. Symbols same as Figure 4 (Appendix A).

U1442A

Core U1442A begins with a LSB with moderate MgO, Na_2O, FeO, and TiO_2 but low SiO_2. MgO and Al_2O_3 decrease up section as the other major elements increase SiO_2, FeO, CaO, and TiO_2 (Figure 24-25). At the base of Unit 2b, there

is a spike in concentrations increasing, SiO_2, Na_2O, TiO_2, and decreasing, FeO, MgO, CaO, Al_2O_3. Through Unit 2b there appears to be a short recharge period followed by a fractionation period that proceeds to halfway through Unit 2a before another period of recharge through to Unit 1d where fractionation dominates

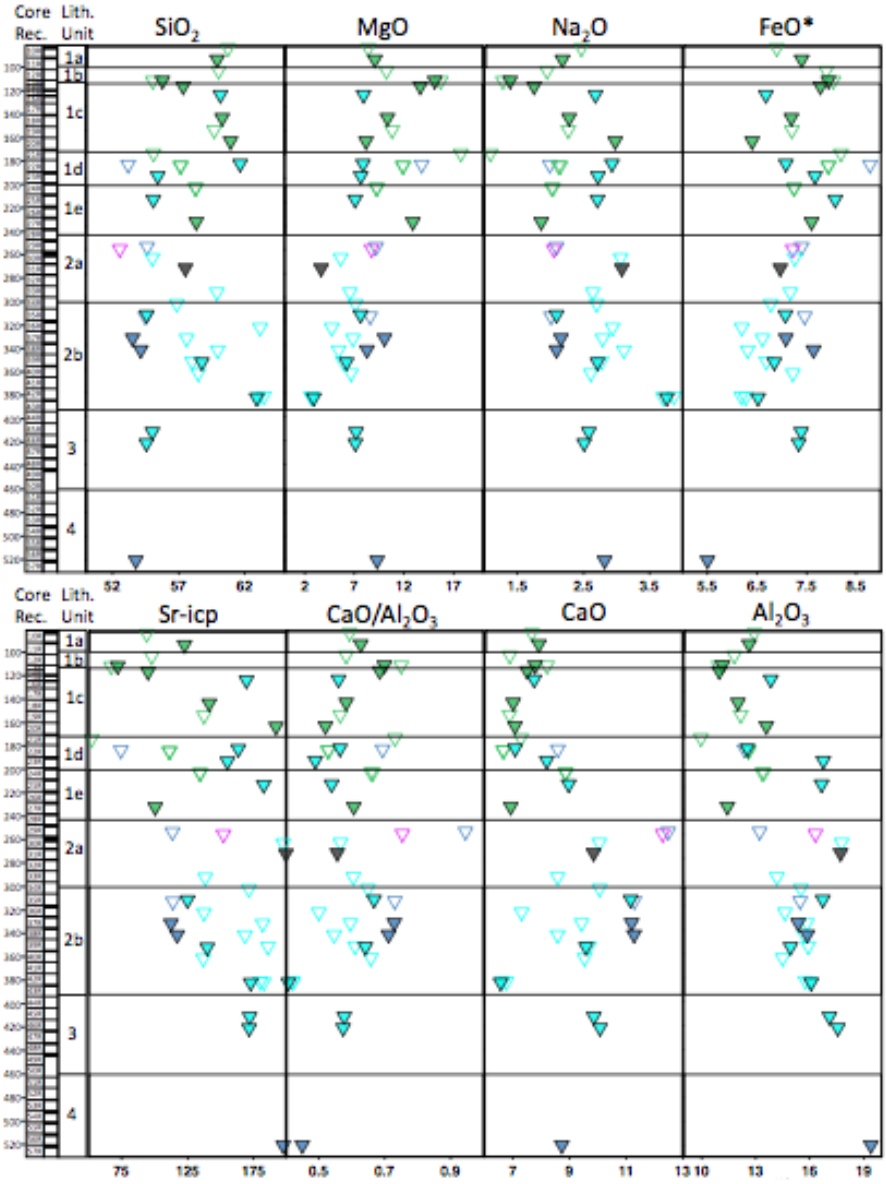

Figure 24. U1442A Depth plots. Unfilled symbols are pool samples from Godard et al., in prep. Symbols same as Figure 4 (Appendix A).

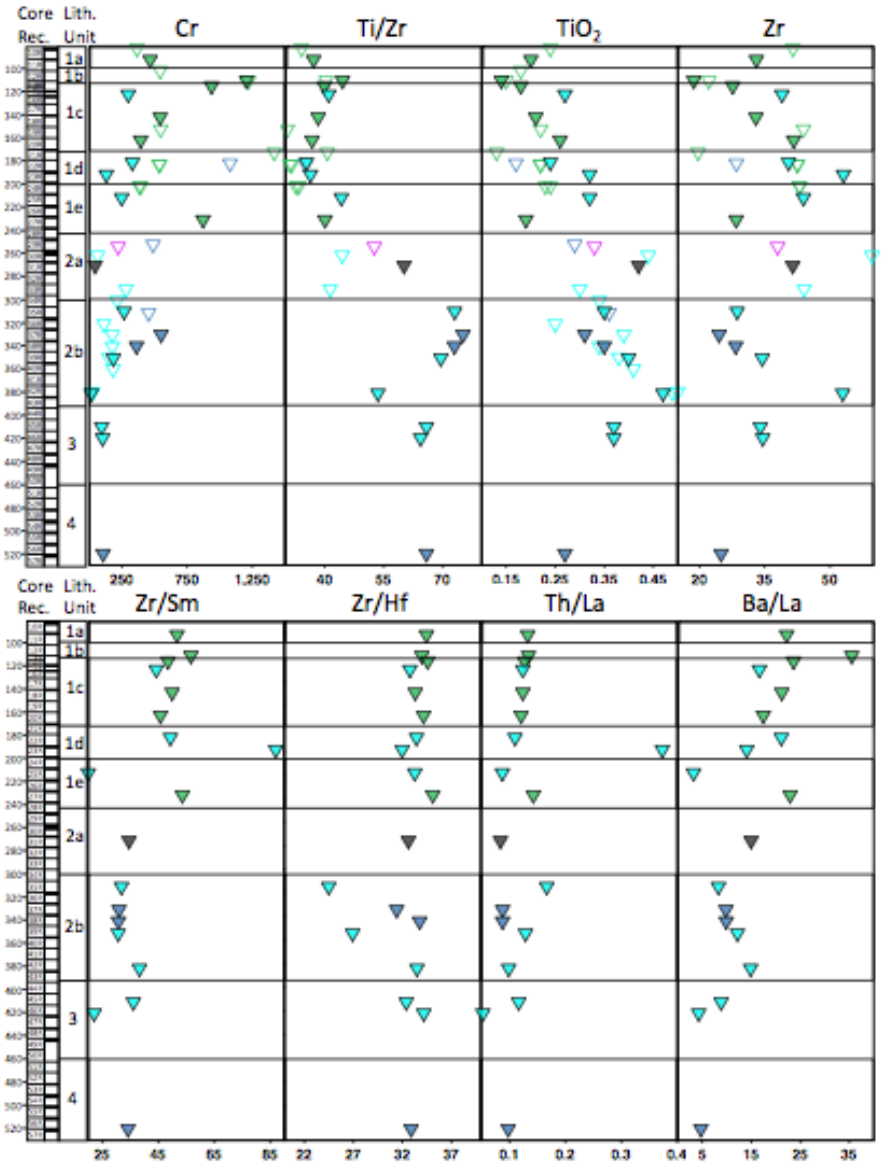

Figure 25. U1442A Depth plots. Unfilled symbols are pool samples from Godard et al., in prep. Symbols same as Figure 4 (Appendix A).

once more. Unit 1b appears to be more primitive than surrounding units with MgO, indicating a short interval of recharge.

Cr remains steady up section with a small spike in Unit 2b and a spike in Unit 1e before gradually increasing to Unit 1a. Zr follows TiO_2 with a spike at the base

of Unit 2b and multiple instances of recharge and fractionation. Zr/Sm has a relatively gradual increase up section, indicating more slab component. Ba/La increases up section, but has a spike at the base of Unit 2b and a decreased spike at Unit 1e.

In this case, the variability of element concentrations could be a factor of multiple sources or magma chambers, and not recharge and fractionation. The upper most portion of Core U1442A is dominated by HSB with higher SiO_2 and Cr than LSB and lower Ti/Zr and CaO than LSB.

U1439C

The base of Core U1439C is similar to a transition zone with low Cr, MgO, CaO Zr/Sm and high TiO_2, Zr, Al_2O_3 more like FAB than boninite (Figure 26-27). Up section SiO_2 remain steady until Unit 5 where there is a small decrease then rapid increase followed by a decrease. The other major elements experience more variation with MgO increasing past the transition zone until the upper portion of Unit 8 where it decreases through to unit 6 where a mild recharge increases concentrations before decreasing again. Na_2O, FeO, Al_2O_3, CaO, and TiO_2 have opposite concentration trends as MgO, decreasing when it increases. Unit 5 has variability in the concentrations, possibly indicating a magma mixing unit.

Zr follows TiO_2 trends and Cr follows MgO trends. Sr remains low throughout the core. Zr/Sm ratio is controlled by distinct units with Unit 8 being greater than Unit 6 and 5 then increasing again up section. Zr/Hf remains relatively steady.

Th/La increases up section with a moderate decrease at the base of Unit 6 before increasing again. Ba/La is the highest in this core and remains steady through the core apart from outliers. The ratio plots have several outliers, some correspond to scatter in Units 8 and 6 for the elements Cr, CaO, and MgO.

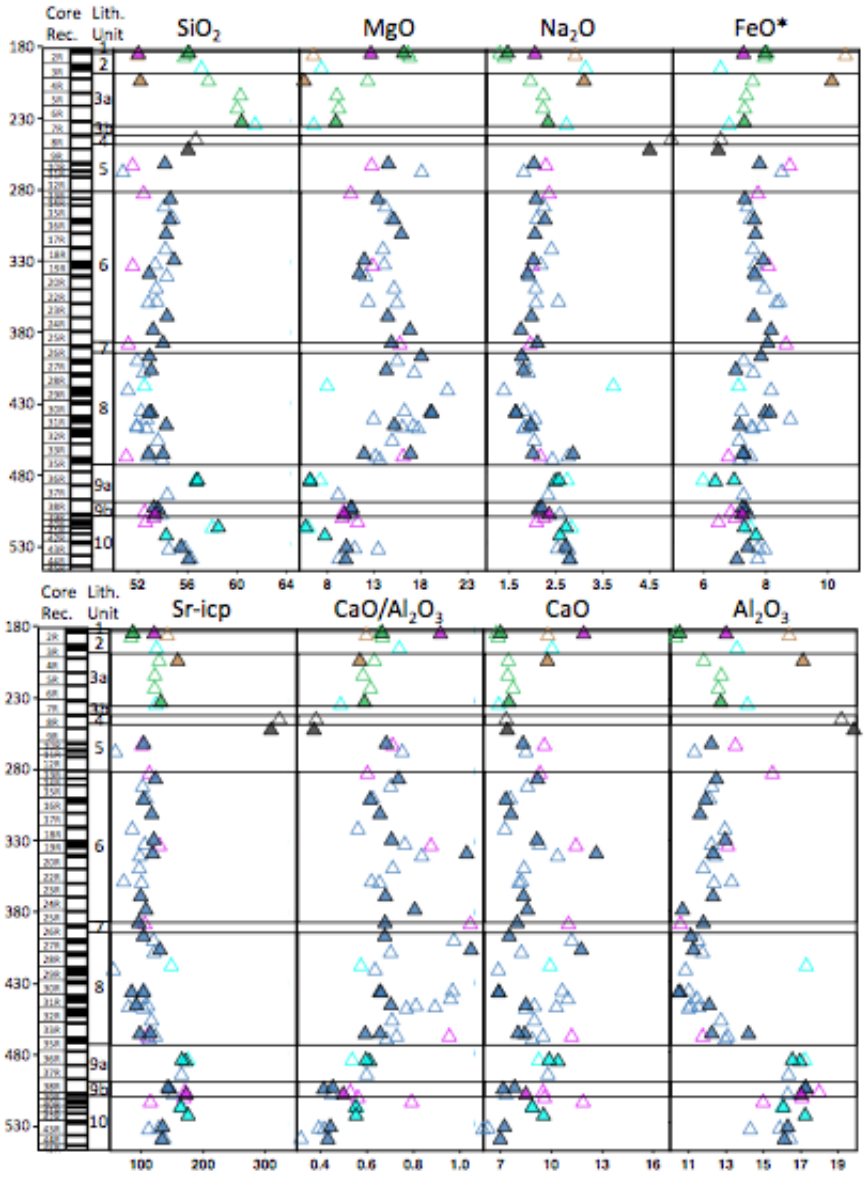

Figure 26. U1439C Depth plots. Unfilled symbols are pool samples from Godard et al., in prep. Symbols same as Figure 4 (Appendix A).

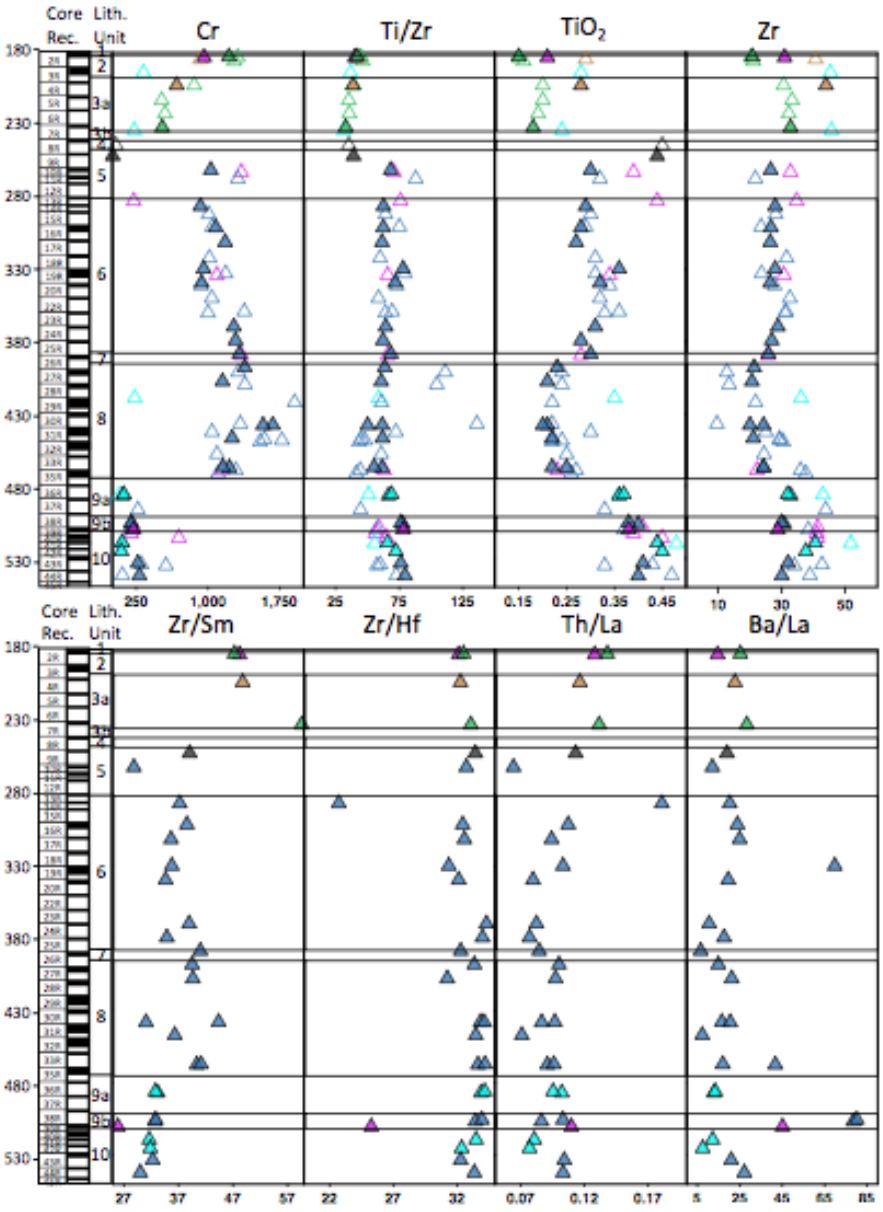

Figure 27. U1439C Depth plots. Unfilled symbols are pool samples from Godard et al., in prep. Symbols same as Figure 4 (Appendix A).

Like core U1442A, the uppermost portion of core U1439C is dominated by HSB with higher SiO_2 lower CaO and Ti/Zr than LSB in the lower core. BB is found throughout the core in both HSB and LSB regimes.

Samples that plot within the FAB region on the MgO-SiO_2 diagram from core U1439C are found within the uppermost HSB regime. Because they plot with boninite in terms of Ti/Zr, Ba/La, Ti/V, and TiO_2, but plot with FAB in terms of FeO, MgO, CaO, and Al_2O_3, they are considered Absolute-FAB, or Ab-FAB. These are the only FAB-like samples within the boninite dominated cores.

GEOCHEMICAL MODELING

Geochemical modeling is used to determine how the source mantle melted to produce the observed FAB and boninite samples. This method applies Salters and Stracke (2004) Depleted MORB Mantle (DMM) as the starting composition for the model. DMM is used because it is a general mantle composition that is likely the source of MORB, and is thought to be basic asthenospheric component in arc magmas as well, prior to the addition of subduction components.

This source evolves as melt is extracted in either the spinel lherzolite or garnet lherzolite stability field. Modes and melt proportions for spinel lherzolite and garnet lherzolite are from Niu (1997), along with calculated spinel harzburgite from the spinel lherzolite values. Here we explore three possible melt models to match the observed FAB and DFAB samples. Primitive FAB and DFAB samples were chosen as well as three primitive boninite samples (Figure 28). Primitive samples are based on high MgO and lowest REE concentrations. In all the following melt models, the MORB-normalized concentration of 1.0

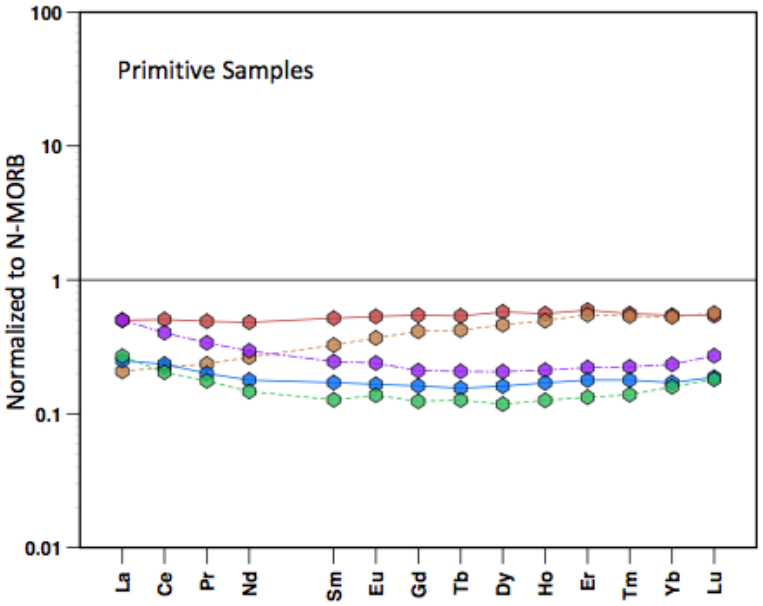

Figure 28. Primitive samples used in modeling. FAB – red, DFAB – brown, BB – purple, LSB – blue, HSB – green. All symbols used for modelling described in Appendix C.

means that the model reproduces MORB melt extraction.

FAB and DFAB Melt Models

Spinel lherzolite melting is possible up to 28% melt, after which clinopyroxene is depleted from the source and changes the source from lherzolite to harzburgite. As melting continues into the spinel harzburgite field, mode and melt proportions must change to that of spinel harzburgite. To put these models into perspective, MORB is generated by about 10-15% melting of DMM source; the model used here requires 10% melting to produce “normal” MORB.

The spinel lherzolite model is shown in Figure 29. At 20% melt, the model appears to match both the FAB and DFAB in the HREE, however DFAB is

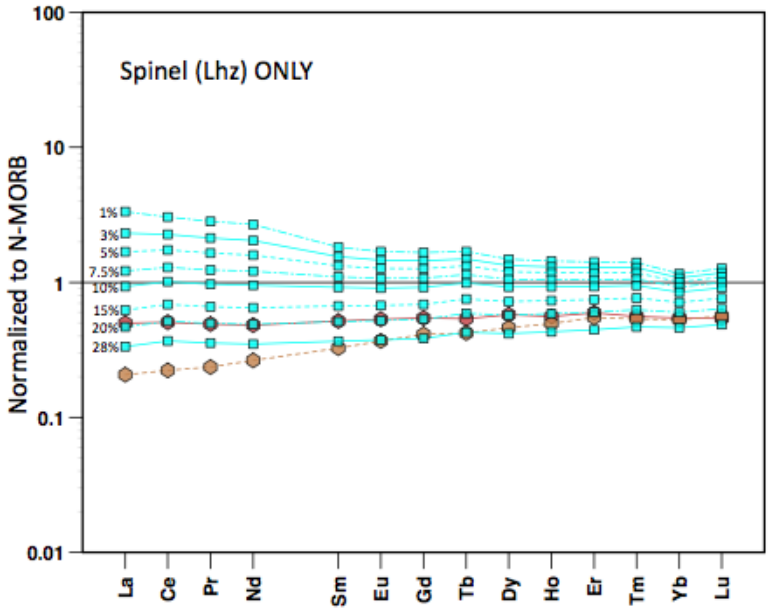

Figure 29. Spinel lherzolite field melting. Model up to 28% melt. Observed samples are FAB and DFAB. All symbols used for modelling described in Appendix C.

depleted in LREE compared to this model. A low LREE/HREE value indicates garnet field melting. Both the FAB and DFAB have low LREE/HREE values, indicating melt occurred in the garnet field to some extent.

The next model considered requires a small amount of garnet lherzolite melt to be removed from the system prior to spinel lherzolite melt. This removal may happen just before spinel lherzolite melts, or could have occurred at any time previously. Removing garnet lherzolite melt lowers LREE/HREE ratios required for FAB and DFAB. The garnet lherzolite melt is removed from a DMM source, leaving a residue that continues to melt in the spinel lherzolite field.

The model spinel lherzolite melt after 1% garnet lherzolite melt has been removed is shown in Figure 30. Although this model can match the observed

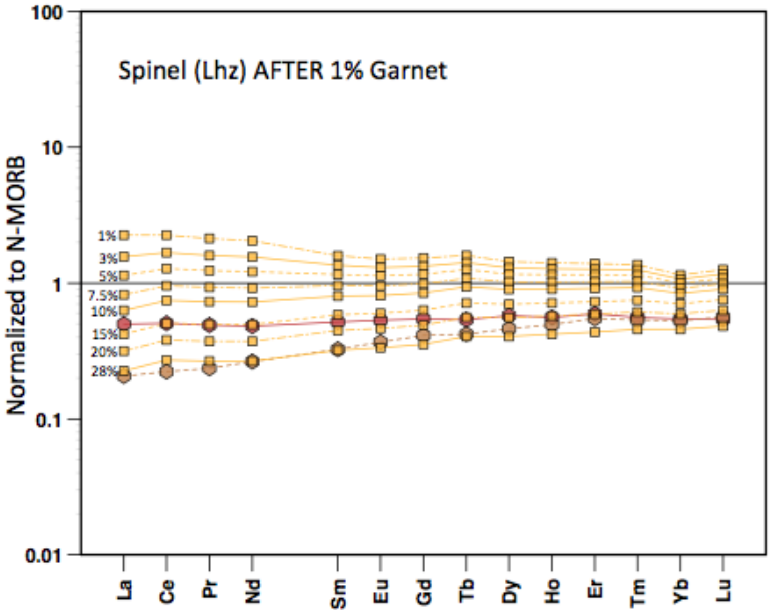

Figure 30. 1% Garnet melt removed. 1% garnet lherzolite field melt removed before continued spinel lherzolite field melting. Observed samples are FAB and DFAB. All symbols used for modelling described in Appendix C.

samples in the HREE spectrum, it does not match in the LREE. In the case of FAB, the model is too depleted in LREE. In the case of DFAB, the model is not depleted enough in LREE.

Removing 2% garnet lherzolite melt before melting spinel lherzolite produces a new model that matches the DFAB closely (Figure 31). By removing more garnet melt, the model is becoming depleted in LREE but the HREE concentrations remain the same. The observed DFAB sample has such low amounts of LREE that garnet melting had to have occurred at some point in the source history.

At 23% spinel lherzolite melt after 2% garnet lherzolite melt has been removed from the system gives a close match of the REE (Figure 32A). The

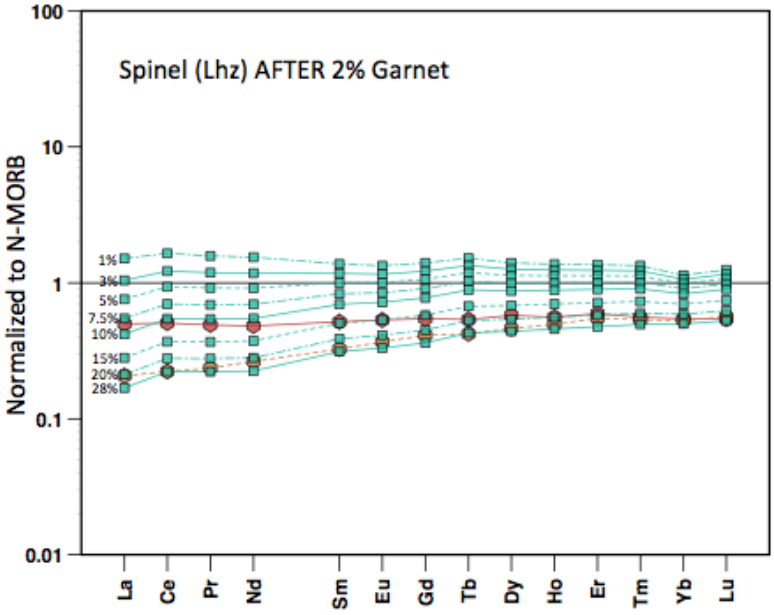

Figure 31. 2% Garnet melt removed. 2% garnet lherzolite field melt removed before continued spinel lherzolite field melting. Observed samples are FAB and DFAB. All symbols used for modelling described in Appendix C.

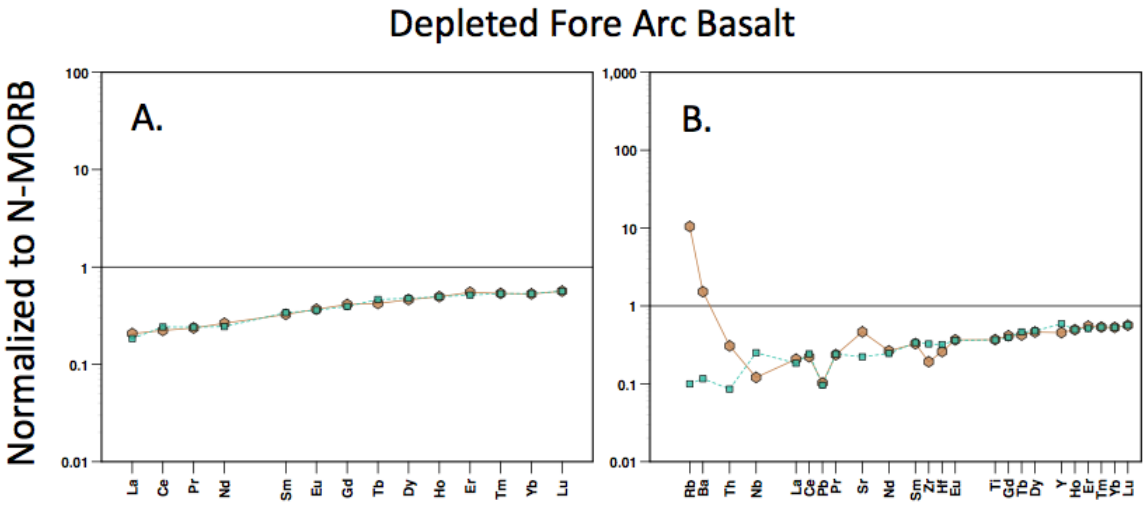

Figure 32. DFAB closest match. 23% spinel lherzolite field melt after 2% garnet lherzolite field melt has been removed is a close match for the D-FAB. A) Rare Earth Element Plot; B) Spider Diagram. All symbols used for modelling described in Appendix C.

corresponding spider diagram shows enrichments in the fluid mobile elements Rb, Ba, Th, and Sr (Figure 32B). However, there are depletions in the elements Nb, Zr, and Hf.

The final model considers a melt that is a combination of spinel lherzolite and garnet lherzolite melt. Like the previous model, this model requires a small amount of garnet lherzolite melt to be removed from a DMM source. This residue is then used to melt spinel lherzolite. The two melts are pooled to produce the model in Figure 33.

Spinel lherzolite pooled with 1% garnet lherzolite melt produces the model in Figure 33. At 20% spinel lherzolite melt mixed with 1% garnet lherzolite melt,

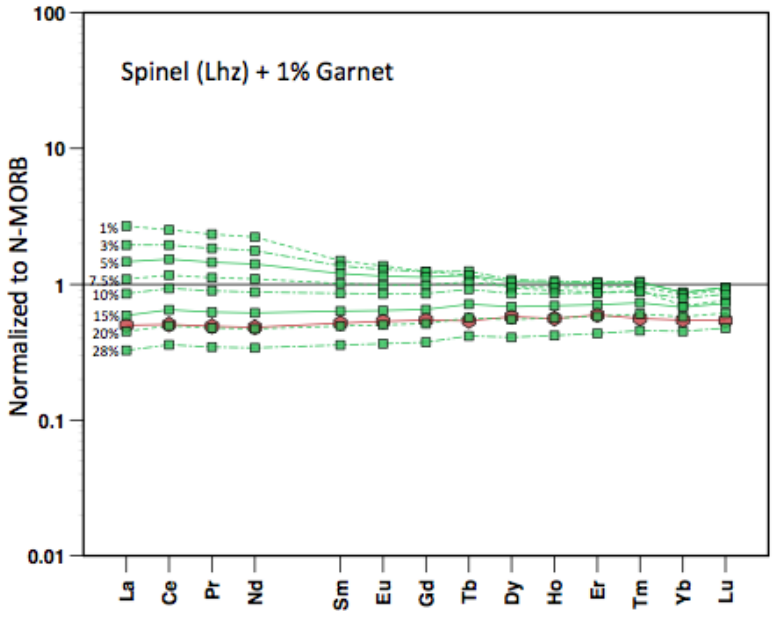

Figure 33. 1% Garnet pooled with spinel melt. 1% garnet lherzolite field melt before continued spinel lherzolite field melt. Pooled melt. Observed sample is FAB. All symbols used for modelling described in Appendix C.

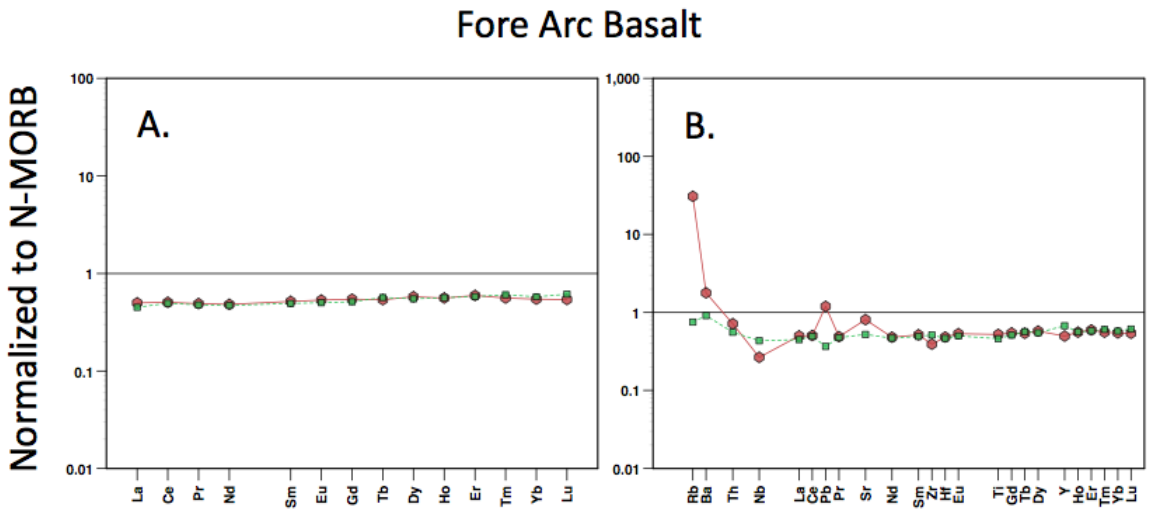

Figure 34. FAB closest match. 20% spinel lherzolite field melting plus 1% garnet lherzolite field melting is a close match for FAB. A) Rare Earth Element Plot; B) Spider Diagram. All symbols used for modelling described in Appendix C.

there is a match in the REE (Figure 34A). The spider diagram shows enrichments in the fluid mobile elements Rb, Ba, Th, Pb, and Sr (Figure 34B). However, there are depletions in Nb and Zr.

Boninite Melt Models

Boninite modeling requires modeling of each of the three boninite types: BB, LSB, and HSB. One sample was chosen from each class based on highest MgO value and lowest REE concentration. These primitive samples are modeled here (Figure 28).

Boninite is believed to be the result of FAB residue melting. This is because boninite is produced from a depleted melt at shallow depth and high temperatures as well as the proximity in time and space to the FAB melt (Green 1973; Umino and Kushiro, 1989; van der Laan et al., 1989; Stern and Bloomer,

1992; Pearce et al., 1992; Falloon and Danyushevsky, 2000; Ishikawa et al 2002; Parman and Grove, 2004; Reagan et al., 2010). The boninite models will use FAB residue as the initial starting composition.

FAB is modeled to have been produced by a 20% spinel lherzolite and 1% garnet lherzolite melt. This means that the source has been depleted by 20% spinel lherzolite melt, leaving 8% spinel lherzolite melt before the clinopyroxene is depleted and melt must continue into the harzburgite field.

Melting of FAB residue in the spinel lherzolite field for the remaining 8% gives the model in Figure 35. The model is too depleted to match the boninite samples. An additional melt must be added to bring the values up to match with

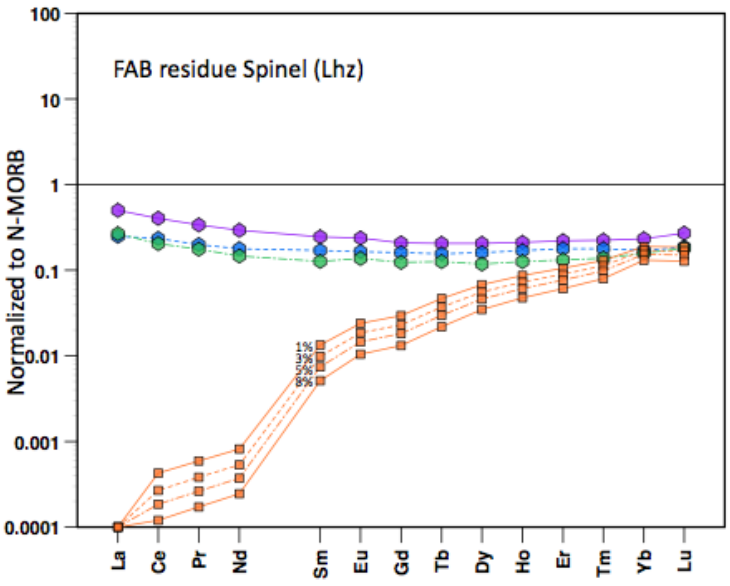

Figure 33. Continued spinel melt from FAB residue. FAB residue starting composition. Continued melting for remaining 8% spinel lherzolite field melt. Observed samples are BB, LSB, and HSB. All symbols used for modelling described in Appendix C.

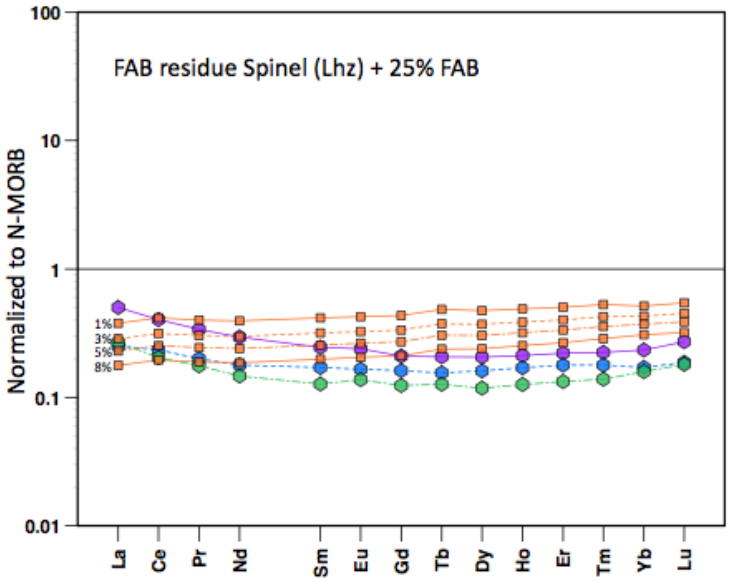

Figure 34. Continued spinel melt from FAB residue pooled with 25% FAB melt. 8% spinel lherzolite field melting plus 25% FAB melt. FAB melt added to bring values up. Observed samples are BB, LSB, and HSB. All symbols used for modelling described in Appendix C.

the boninite samples. In this case, we chose to add 25% FAB melt to the melt (Figure 36). This brings all the values up high enough for additional melt to match the boninite samples. This is the maximum amount of FAB melt that can be added to the melt and still be able to match the boninite samples. FAB melt is chosen because it is still being produced at the same time as the boninite.

Continued melting into the spinel harzburgite field creates the model in Figure 37. This model will be used to determine the best fit for all three boninite samples because through the length of the core, all three boninite types are interbedded. While this model can match any of the three boninite types, we chose to match it to the Low Silica Boninite (LSB). LSB was chosen because it is the lowest, first produced, of the boninite in the cores (Figures 24-27).

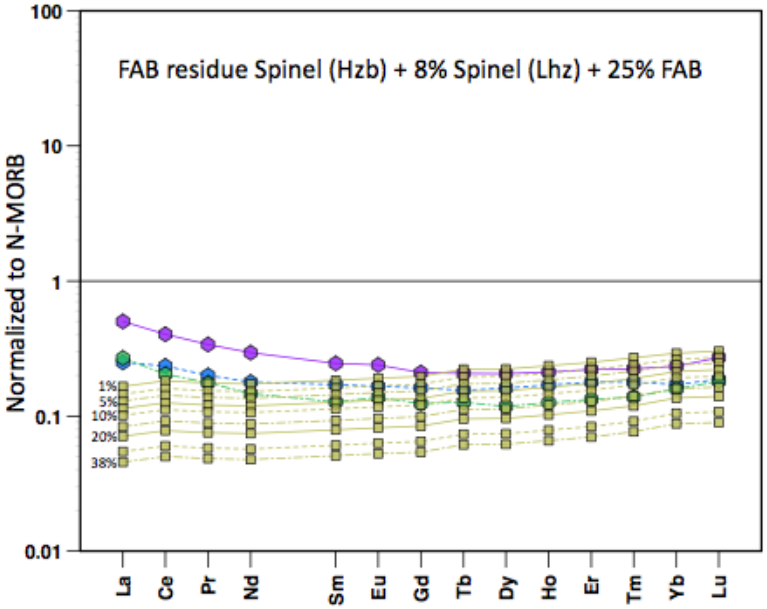

Figure 35. Continued melt into spinel harzburgite field. Continued melting into the spinel harzburgite field as CPX is depleted. Observed samples are BB, LSB, and HSB. All symbols used for modelling described in Appendix C.

The model matches LSB at 7.5% spinel harzburgite melt added to 8% spinel lherzolite melt, mixed with 25% FAB melt (Figure 38). Spinel lherzolite melts and spinel harzburgite melts must be added together because the model is continued melting of spinel harzburgite which is added to the spinel lherzolite. The spider diagram shows enrichment in the fluid mobile elements Rb, Ba, Th, Pb, and Sr, as well as enrichment in the melt mobile elements Nb, Zr, and Hf (Figure 38).

In order to model HSB and BB, we use the residue from the LSB melt. HSB and BB are interbedded in the core, implying they have the same source composition, but they are distinct from LSB.

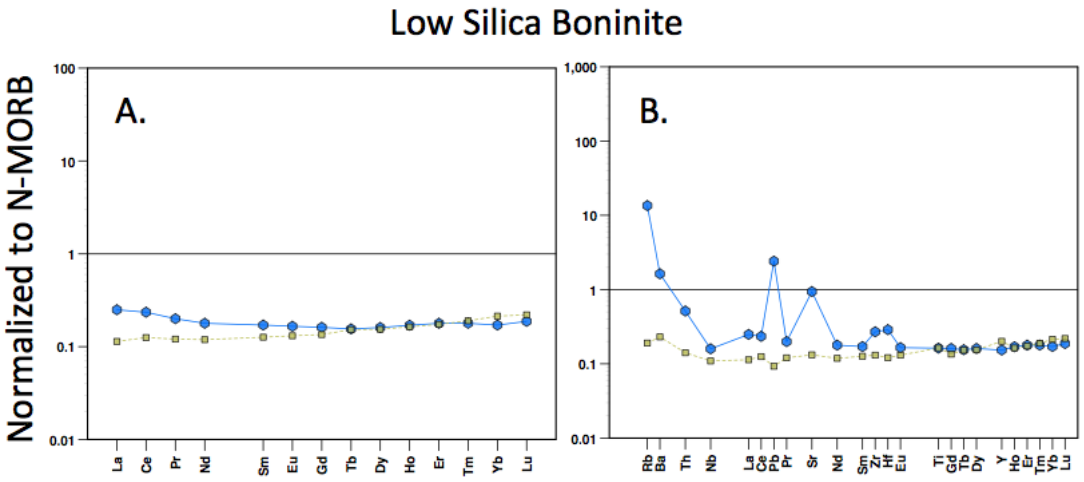

Figure 38. LSB closest match. 7.5% spinel harzburgite field melting + 8% spinel lherzolite field melting + 25% FAB is a close match for LSB. A) Rare Earth Element Plot; B) Spider Diagram. All symbols used for modelling described in Appendix C.

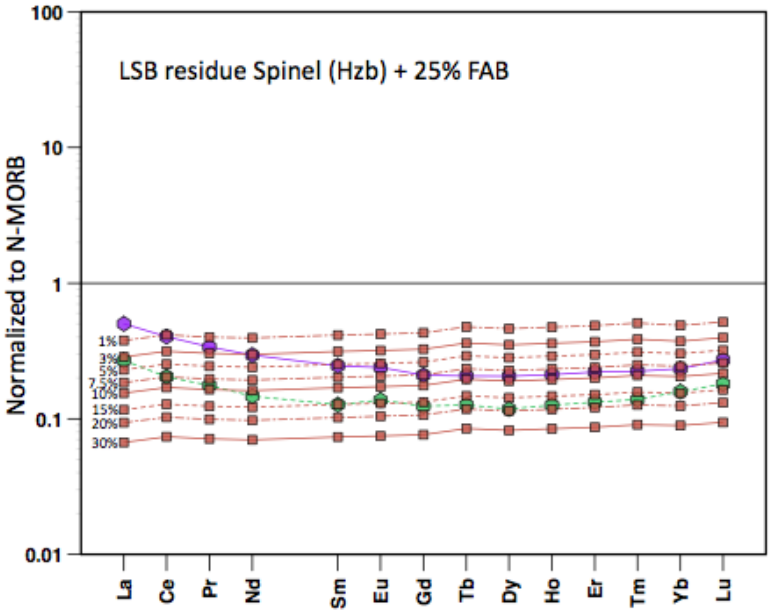

Figure 36. Continued melt from LSB residue. LSB residue starting composition. Spinel harzburgite field melting up to 25% melt. Observed samples are BB and HSB. All symbols used for modelling described in Appendix C.

Continued melting in the harzburgite field with LSB residue starting composition gives the model shown in Figure 39. There are matches for both BB and HSB samples.

BB has a close match at 7.5% spinel harzburgite melting with the addition of 25% FAB (Figure 40). The REE pattern is depleted relative to the sample in LREE. The spider diagram shows enrichment in fluid mobile elements Rb, Ba, Th, Pb, and Sr, as well as the melt mobile elements Nb, Zr, and Hf (Figure 40).

HSB has a close match at 20% spinel harzburgite melting with 25% FAB melt added in Figure 41. The model REE pattern is depleted relative to the samples in LREE and the HREE Yb and Lu. The spider diagram shows

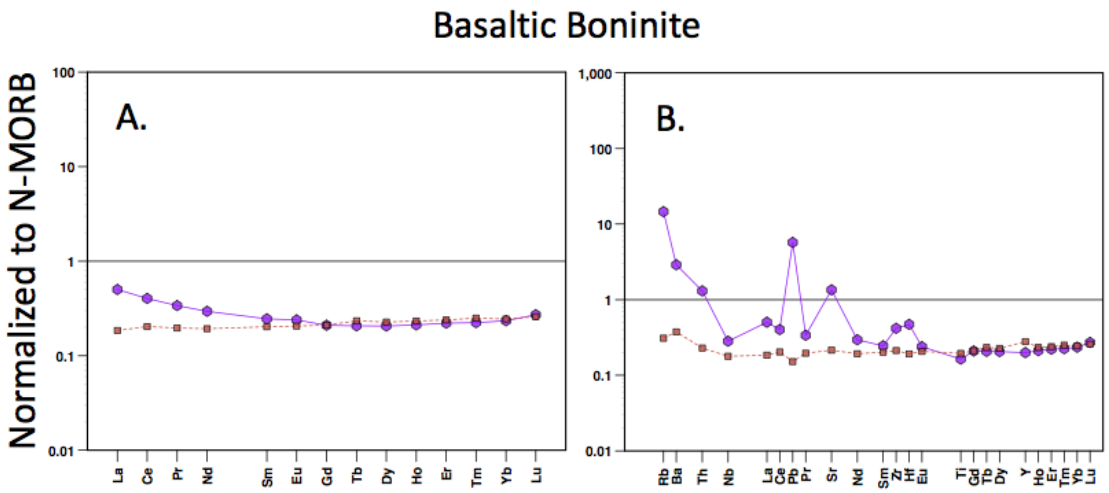

Figure 40. BB closest match. BB close match from LSB residue starting composition. 7.5% spinel harzburgite field melting required. A) Rare Earth Element Plot; B) Spider Diagram. All symbols used for modelling described in Appendix C.

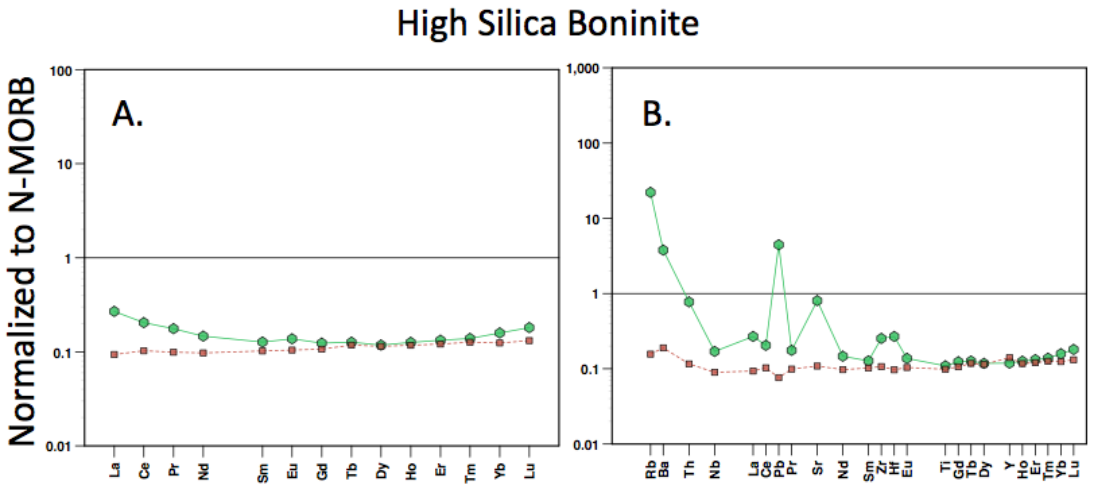

Figure 41. HSB closest match. HSB close match from LSB residue starting composition. 20% spinel harzburgite field melt required. A) Rare Earth Element Plot; B) Spider Diagram. All symbols used for modelling described in Appendix C.

enrichment in the fluid mobile elements Rb, Ba, Th, Pb, and Sr, as well as the melt mobile elements Nb, Zr, and Hf (Figure 41).

An alternative model is that BB is generated at the same time as LSB from a FAB source. In this case, BB is matched at 3% spinel harzburgite plus the 8% spinel lherzolite it takes to transition into harzburgite and the addition of 25% FAB (Figure 42). The REE pattern is still depleted relative to the sample in LREE and the spider diagram has enrichments in the fluid mobile and melt mobile elements (Figure 42).

HSB is considered to have a LSB starting composition because very little LSB is produced after HSB appears in the cores. Conversely, BB is found interbedded with both LSB and HSB, implying it is separate from both and being produced simultaneously.

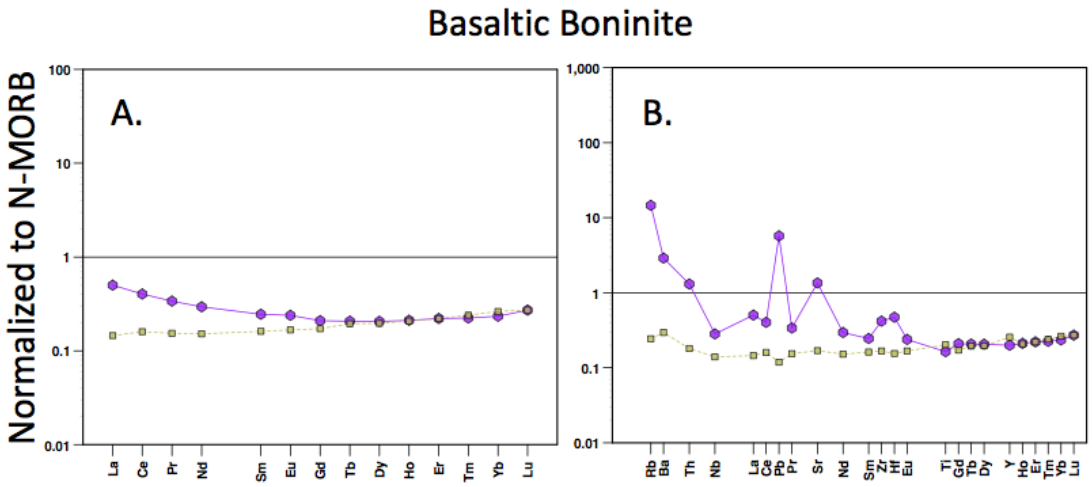

Figure 42. BB closest match from FAB residue. BB close match from FAB starting composition. 3% spinel harzburgite + 8% spinel lherzolite + 25% FAB required. A) Rare Earth Element Plot; B) Spider Diagram. All symbols used for modelling described in Appendix C.

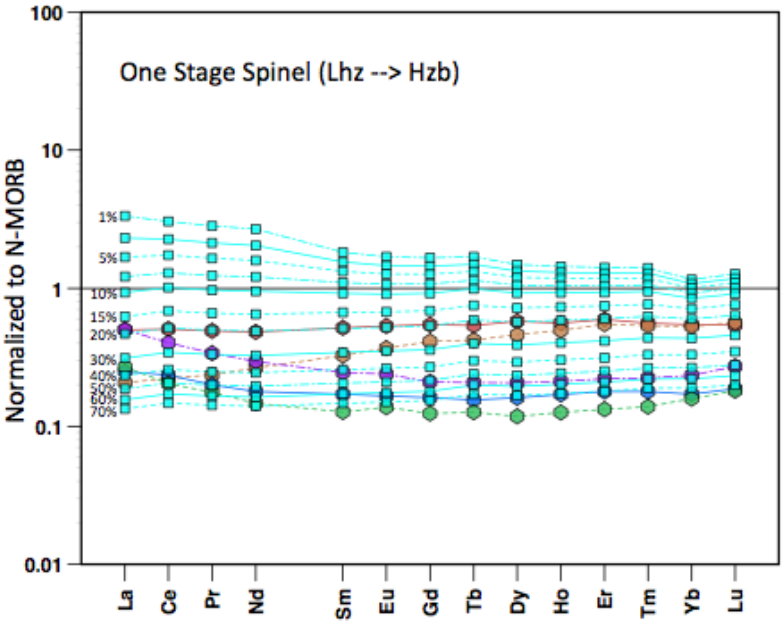

Figure 43. One-stage spinel melt. One-stage melting with a DMM starting composition. Spans spinel lherzolite field melting and spinel harzburgite field melting. BB closest match at 60% melt. Observed samples are FAB, DFAB, BB, LSB, and HSB. All symbols used for modelling described in Appendix C.

What if boninite is not from FAB residue? Modeling of one-stage melt shows that in order to match boninite it requires up to 60% melt to match BB, more to match HSB (Figure 43). In this case, melting would span the spinel lherzolite field, the spinel harzburgite field, and into the dubious dunite field to match HSB. It is unlikely that such large melt fractions can be generated in the mantle without separating from the residue. As a result, we focus on boninite being generated from FAB residue.

Total Melt Extraction (TME)

Total Melt Extraction (TME) of the initial mantle source is determined by taking a percentage of the remaining melt. FAB is produced from 1% garnet lherzolite taken from 100% source to produce 1% TME. Continuing melting takes 20% spinel lherzolite melt from the remaining 99% source, producing 19.8% melt. Combining 1% and 19.8%, FAB has a TME of 20.8%.

The next melt extraction is LSB from a FAB residue starting composition. Starting with 79.2% residual source, 8% spinel lherzolite was melted, resulting in 6.3% melt and a residual source (relative to the starting mass) of 72.9%. An additional 7.5% spinel harzburgite was removed from 72.9%, resulting in 5.5% melt and a residue remaining of 67.4%. Combining the FAB melt extract, spinel lherzolite melt, and spinel harzburgite melt, LSB has a TME of 32.6%.

HSB is a product of LSB, requiring a starting composition of 67.4% source relative to the starting mass. HSB is 20% spinel harzburgite from 67.4% residual source remaining, resulting in 13.5% melt and a residue of 53.9% remaining.

Combining the LSB melt extraction, HSB as a TME of 46.1%. If BB is modeled from LSB residue, then the starting composition would be 67.4% source relative to the starting mass. BB is 7.5% spinel harzburgite must be removed from 67.4% residual source remaining, resulting in 5.1% melt and a residue of 62.3% remaining. Combining the LSB melt extract, BB has a TME of 37.7%.

Alternatively, if BB is modeled from a FAB starting composition, then the starting composition would be 79.2% source relative to the starting mass. Starting with 79.2% residual source, 8% spinel lherzolite was melted, resulting in 6.3% and a residual source (relative to the starting mass) of 72.9%. BB is 3% spinel harzburgite from 72.9% residual source, resulting in 2.2% melt and a residue of 70.7% remaining. Combining the FAB melt extract, spinel lherzolite melt, and spinel harzburgite melt, BB has a TME of 29.3%.

The starting composition was DMM, a lherzolitic mantle source. After 46.1% melt has been removed from it, the remaining source is depleted harzburgitic, nearly dunite.

Enriched Element Addition

Both fluid mobile elements and melt mobile elements must be added to the boninite and FAB models to match the observed sample values. There is variation in each of the 124 samples as to how much of each element must be added to each sample, as a result, some values in Figure 44 are averages where the observed sample is negative compared to the model. These elements include Nb and Zr in FAB, Ti in LSB, and Ti in BB where original samples are negative.

Figure 44 is a logarithmic histogram of the amount of each element that must be added.

Fluid mobile elements are added to all samples as observed in Figure 44a. The greatest amount added to an element is 100 ppm Sr in BB (Figure 44a). A considerable amount of Rb, Ba, and Sr are added to all samples Table 5. Rb addition is greater for FAB (~16 ppm) and least for LSB (~7 ppm). Ba addition is greatest for HSB (~22 ppm) at four times the amount of FAB (~5 ppm) and twice the amount of LSB (~9 ppm). Th addition is lowest for FAB (~0.02 ppm) and highest for BB (~0.14 ppm), but still under 1 ppm addition. Pb addition is lowest for FAB (~0.25 ppm) and greatest for BB (~1.7 ppm), but still around 1 ppm addition. Sr addition is ~25 ppm for FAB and ~100 ppm for BB.

Melt mobile elements are added to all samples as observed in the normalized histogram (Figure 44b). The element with the most addition is Ti at ~1000 ppm addition for BB (Note, this is an average value across all BB samples). Zr has the next highest addition at ~18 ppm for BB. Addition of the other elements are less than 1 ppm (Figure 44a). There is no Nb value or FAB due to an average depletion of that element compared to the model. BB requires the greatest amount of element addition of all samples represented, in general at least twice as much as HSB and LSB. FAB requires the least amount of addition, as expected. Except for Ti, HSB and LSB require very similar addition for the elements.

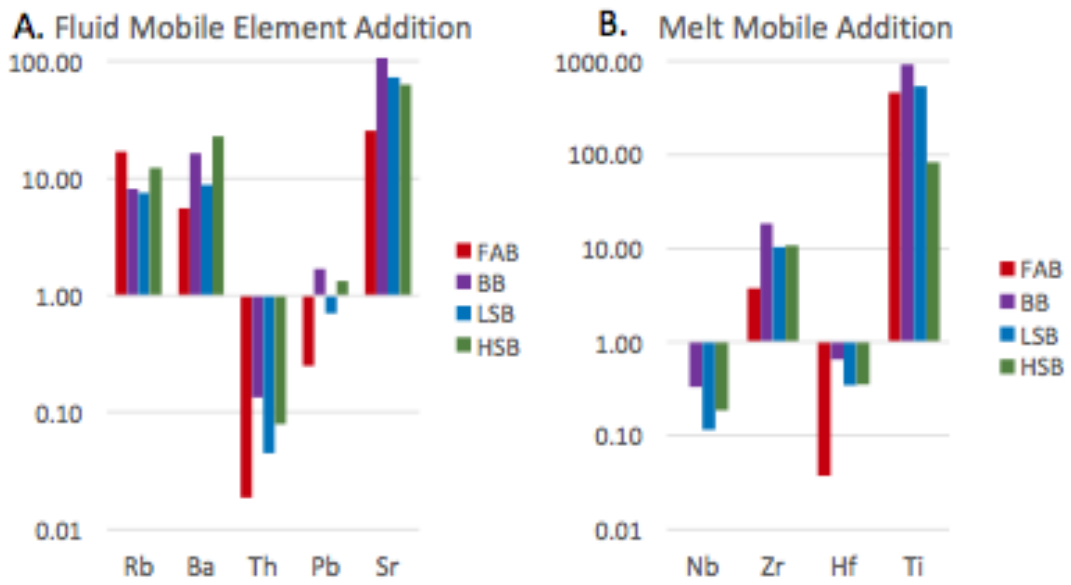

Figure 7. Difference between modeled and observed samples. These graphs show the amount of each element that must be added to the model to match the observed samples. Logarithmic scale in ppm. A. Fluid Mobile Element Addition where Rb and Sr are mobile at low temperatures and Ba, Th, and Pb are mobile at high temperatures. B. Melt Mobile, also known as High Field Strength Incompatible Element, addition. Primitive samples chosen to model resulted in negative values, so an average of certain elements was chosen: Zr in FAB, Ti in LSB and BB. Nb in FAB is a negative value and does not appear here.

Table 5. Enriched Element Addition. Difference between observed primitive samples and models. FME include: Rb, Ba, Th, Pb, and Sr. HFSE include: Nb, Zr, Hf, and Ti.

	FAB			LSB		
	Model	Observed	Added	Model	Observed	Added
Rb	0.42	17.27	16.85	0.11	7.57	7.47
Ba	5.74	11.22	5.48	1.45	10.27	8.82
Th	0.07	0.09	0.02	0.02	0.06	0.04
Pb	0.11	0.36	0.25	0.03	0.72	0.70
Sr	46.99	72.48	25.49	11.89	84.65	72.76
Nb	1.01	1.00	-0.01	0.26	0.37	0.11
Zr	38.09	41.85	3.76	9.68	19.97	10.29
Hf	0.96	0.99	0.04	0.25	0.59	0.34
Ti	3503.28	3958.72	455.44	1242.22	1778.82	536.59

	HSB			BB		
	Model	Observed	Added	Model	Observed	Added
Rb	0.09	12.36	12.27	0.14	8.19	8.05
Ba	1.19	23.80	22.60	1.85	18.20	16.34
Th	0.01	0.09	0.08	0.02	0.16	0.13
Pb	0.02	1.33	1.31	0.04	1.72	1.68
Sr	9.77	72.16	62.39	15.18	120.97	105.79
Nb	0.21	0.40	0.19	0.33	0.66	0.33
Zr	7.92	18.70	10.78	12.36	30.86	18.50
Hf	0.20	0.55	0.35	0.32	0.96	0.65
Ti	749.66	832.00	82.34	1538.49	2466.01	927.52

CHAPTER IV

DISCUSSION

Modeling

Geochemical modeling of FAB and boninite provide some basic constraints on the origins of these magmas: (1) FAB and DFAB both require a small amount of melting in the garnet field in order to produce the observed LREE/HREE ratios; (2) boninite may be produced from FAB residue only at high degrees of melting, and with addition of a second melt; (3) all samples, boninite and FAB, are enriched in fluid mobile elements Rb, Sr, and Ba relative to the model equivalents; (4) boninites require the addition of melt mobile elements including the High-Field Strength incompatible Elements (HFSE) Nb, Zr, Hf, and Ti as well as the LREE-MREE.

Small amounts of melting in the garnet field reduces the concentration of LREE-MREE without affecting the HREE. Increasing amounts of melting severely depletes the LREE-MREE and increases HREE slightly. A small amount of garnet field melting is required to model FAB and DFAB due to the LREE-MREE depleted nature of the samples. However, because the HREE are also depleted relative to MORB, melting must continue into the spinel field to lower all the REE to the appropriate concentrations.

As seen in Figure 43, one-stage spinel field melting up to 70% TME could provide matches for the boninite samples. However, it is unlikely that a melt of that magnitude would remain pooled without separating from the molten source

region. More likely, the residue from FAB melting is melted through hydrous flux from the descending slab at depth. That melt may then be affected by fluids and sediment melting off the subducting plate. As the melt rises in the fore arc, it encounters the decompression melt zone that produced the FAB and mixes with a small portion of the decompression melt before erupting. This occurs largely in the mantle source region, but pooling of these melts is observed by magma mixing in the cores U1439C and U1442A reported by the shipboard scientists of IODP Expedition 352 (Reagan et al., 2015).

TME values for the boninites are high, ~33-46% melt. A typical MORB will have a TME of ~10%. Although this high TME seems improbable, lherzolite and harzburgite have been retrieved from the fore arc (Pearce et al., 1992). In order to deplete the mantle from lherzolite to clinopyroxene-free harzburgite, a minimum of 28% melt must occur (from the models here). Thus, is it likely that the high TME for the boninites is not an error, but an actual process.

Evidence supporting decompression melting continuing as fluid flux melting occurs is observed in the FAB samples found within the HSB regime of core U1439C. The decompression melt residue supplies boninite production as well, indicating it must still be occurring. Interbedded boninite, BB within LSB and HSB, could be a factor in the amount of decompression residue that is melted. If the decompression residue is melted only a few percent, BB is generated. If it melts more than that, LSB is generated. HSB is modeled to be generated when the LSB residue is melted again.

The generation of HSB also requires a greater addition of silica-rich melt

from the sediment melt off the descending slab than the other boninites. This process may not require as much TME as we modeled here for HSB.

Magma Mixing

Magma mixing has been identified petrographically in the cores as well as geochemically (Reagan et al, 2015). There are several instances of variable element concentration observed in the chemostratigraphy reported here. Units 1, 3, and 5 in Core U1440B have a broad range of elemental values while other units have very tight ranges (Figures 20-21). Cores U1439C and U1442A have alternating, interbedded rock types of HMA and BB in the LSB and HSB regimes. FAB samples from the data reported here and the pool samples, are observed within the HSB regime of core U1439C.

The variability of rock types within the same lithographic unit, as defined by the Scientists of IODP Expedition 352 (Reagan et al., 2015), indicates that more than one type of magma is present. If there was only one magma body contributing to the flows, then within a given unit we would be able to see fractionation. We should be able to observe the evolution of one rock type to higher SiO_2, lower MgO, and so on. Instead, what we see is fraction interrupted with samples that do not plot on the fractionation lines. Typically, the LSB or HSB samples will be fractionating and a BB or HMA sample with plot at the same depth in the element v depth plots (Figures 24-27).

If there are multiple magma chambers contributing to the same flow, then mixing may occur. Mixing is not complete, or there would be no variable rock

types present.

FME Addition

High FME/HFSE ratios indicate hydrous fluid flux from the subducting plate into the depleted mantle source, enriching the FME (MacPherson and Hall, 2001). Subduction initiation models show that fluid is driven off the descending slab as soon as it begins to be thrust under the upper plate (Gerya and Meilick, 2010; Leng et al., 2012). This could explain why FAB has variable FME enrichment compared to the models and N-MORB. Alternatively, the FME addition experienced by FAB could be a product of seawater alteration post eruption.

The elements susceptible to seawater alteration include Rb, K, U and to a lesser extent Sr, Ba, and Na_2O (Staudigel et al., 1996). Many elements, such as U and Na_2O, are deposited as secondary minerals such as zeolites or carbonates. The concentration of Rb, Ba, K, Pb, and Sr in these samples tend to be highly enriched, suggesting that there was seawater alteration post-eruption (Figures 18-19). U is enriched from the seawater as a secondary mineral in carbonate deposition, has high solubility in oxidizing conditions, and a large percent (~70%) is derived from the subducting slab (Staudigel et al., 1996). U is highly enriched in these samples relative to MORB, indicating a portion must have come from the descending plate. This implies that while seawater alteration post-eruption has occurred, it is not the only source of FME.

A significant FME addition of the models to match the observed samples is

required for low-temperature FME based on Rb, Ba, and Sr, but a much smaller amount for those elements not mobile in seawater alteration, Th, Ba, and Pb. This also indicates that there were two process occurring to give high FME concentrations in the samples. The less mobile elements are not as enriched as the more mobile elements, but they are enriched relative to MORB and the models.

HFSE Addition

Elements that are immobile at low-temperatures include the HFSE Nb, Zr, Hf, and Ti. These elements tend to be enriched relative to the models, and not necessarily to NMORB. In order to enrich these elements, a melt is required. The melt may be a second magmatic source or the melt of sediments from the descending slab.

The boninite models require a second melt to increase the REE concentrations of the FAB residue models to match the observed samples. However, the secondary magma used does not enrich those elements, indicating that there must be a third melt or that the secondary melt is more enriched than what we used. If a secondary melt were to provide the enriched elements here, it would have to be enriched in those elements, but still depleted in HREE.

More likely, HFSE addition is derived from melt from the subducting plate. At depth, sediment and some basaltic crust is melted and, like fluids, is added to the mantle melt (specifically in this case to the initial boninite melt). The composition of sediment will determine the concentration of the elements and

thus how much sediment melt would be required to enrich the samples we see. Generally, sediment melt will enrich the mantle in SiO_2, LREE-MREE, HFSE, and some FME. More work is necessary to determine the sediment composition, elemental concentration, and partition coefficients to determine how much sediment melt is added to these samples. We can say that some amount of sediment melt has pooled with the initial boninite concentrations because we do see enrichment in elements that require a melt to be mobile.

In addition to the HFSE elements, LREE-MREE must be added to the boninite models to get the U-shaped REE pattern observed in boninites. Using the element enrichment graphs in Figure 44, we can see that a small amount of Nb and Hf are required, but a significant amount of Ti is required to be added. Using the N-MORB normalized models, we see that only a small amount of REE are needed to match the model with the observed samples (Figures 32, 34, 38, 40, 41, and 42).

Subduction Initiation

Subduction initiation models for the IBM have matured over time and incorporate more factors of actual subduction such as water content, rates of convergence, plate strength, plate composition, plate age, and volcanic products (Hall et al., 2003; Gurnis et al., 2004; Leng and Gurnis, 2011; Leng et al., 2012). These models simulate computationally what is observed in the field. A recent model that attempts to match observed with modeled chemistry is performed by Leng and others (2012). The model A01 from Leng and others (2012) shows

continuous subduction with infant arc spreading and the effects of water (figure 3 in paper). The parameters for this model include a fixed subducting plate age of 82 m.y. and an imposed velocity of 4 cm/yr with fixed plate strength parameters. They successfully modeled the volcanic transition from MORB-like tholeiite to boninitic composition with the effects of water. In their model, slab foundering causes adiabatic melting beneath the spreading center that forms tholeiitic volcanic rocks. As the slab continues to founder, the spreading center and volcanic composition change moves with trench retreat. When water is added, the mantle entering the mantle wet zone is residual to the melt extraction beneath the infant-arc spreading center and is re-melted due to the water injection into this zone. This process gives rise to boninite. Volcanic composition changes taking place are modeled via batch melting and using values from Workman and Hart (2005).

The subduction initiation model described above has some similarities to the processes required by the geochemical modeling performed here, however, there are discrepancies. Differences include plate ages, actual volcanic composition and the methods they performed to determine them, location of these volcanic composition changes, and timing of their extrusion onto the surface. The Pacific Plate that subducts beneath the Philippine plate is Jurassic in age. The volcanic compositions in Leng et al., 2012 are from Workman and Hart (2005) whereas those described here are from Salters and Stracke (2004). The method used in Leng and others (2012) employs batch melting to model the compositional change, whereas we use fractional melting and pooling of the melt.

Their model requires the volcanic composition change to follow trench retreat, meaning the boninitic compositions would be closest to the trench and MORB-like farther from the trench, we find the opposite with FAB closer to the trench and boninite further away. Their timing is modeled to all occur at the same time, however from previous research, we know the FAB (MORB-like) precedes the boninite with no hiatus (Reagan et al., 2010), and may overlap boninite (Shervais et al., 2016; GSA Abstract).

Geochemical modeling suggests a variation to the subduction initiation model described above. Our model is theoretical and uses the subduction initiation models of Leng and others as geodynamic support (Figure 45).

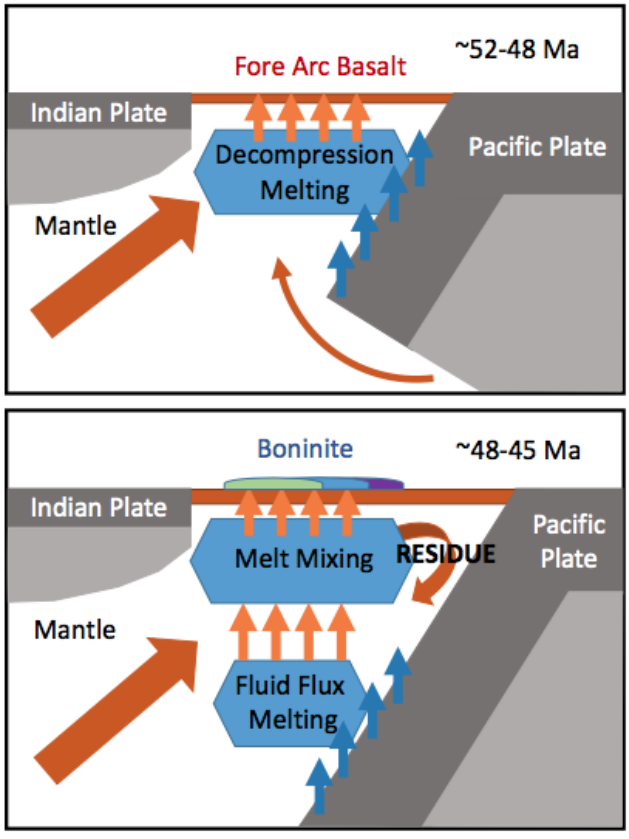

Figure 45. Subduction Initiation Model. DMM produces FAB, residue is melted via hydrous flux, mixes with sediment and FAB melt.

Subduction initiated in the western Pacific at approximately 52 Ma as the Pacific plate began subducting beneath the Philippine Plate (Meijer et al., 1983; Cosca et al., 1998; Ishizuka et al., 2006; Reagan et al., 2010; Wu et al., 2016). Geodynamic subduction initiation models show a period of convergence as one plate is thrust beneath another before plate foundering occurs (Hall et al., 2003; Gurnis et al., 2004; Leng and Gurnis, 2011; Leng et al., 2012). The Pacific plate founders, detaching from the upper Philippine plate and begins its rapid descent into the mantle. As the plate descends, hot asthenospheric mantle rises into the space created by the falling slab.

As the Pacific plate founders, trench rollback occurs. As the trench retreats, the Philippine plate undergoes extension. Thinning of the upper plate along with rising hot mantle leads to adiabatic decompression melting of the mantle. This melt is then erupted onto the extended Philippine plate as FAB from ~52-48 Ma (Ishizuka et al., 2006, Ishizuka et al., 2011). As the plate subducts, water is driven off and interacts with the melt, enriching FME.

The residual mantle after the production of FAB is dragged down the subduction channel with the descending plate. At depths approximately ≥ 1 GPa, water driven off the subducting plate interacts with the residual depleted mantle and lowers the melting temperature, allowing the residual mantle to melt and enriching FME. At the same time as water is being driven of the slab, sediment on the slab is melted. This melt is added to the fluid flux melt of the residual mantle, enriching HFSE.

The fluid flux melt rises into the decompression melt zone where it mixes

with a small amount of decompression melt. The melt is then erupted as boninite, specifically LSB and BB with variable amounts of melt, from ~48-45 Ma (Ishizuka et al., 2006, Ishizuka et al., 2011). The residual melt from the fluid flux melting that produces LSB is re-melted in the fluid flux zone and follows the same pathway as the other boninite. It mixes with sediment melt and rises to mix with decompression melt that is then erupted as HSB.

This model is based on induced subduction initiation with a fixed convergence between the plates. Other researchers have been working on the spontaneous subduction initiation of the IBM (Arculus et al., 2015; Leng and Gurnis, 2015). Spontaneous initiation would require a large age and compositional difference between the plates at a weak zone (Leng and Gurnis, 2015). The model from Leng and Gurnis (2015) requires a thermal rejuvenation of the Philippine plate through a relic arc to alter the chemical composition and reset the age. With such a vast difference in age and composition, the gravitational instability of the older denser Pacific Plate would allow it to sink and initiate subduction. The weak zone between plates can be an old fault, weakened through fluid flux, or some other type of weak zone.

This spontaneous model would have extension in the fore arc as the Philippine plate is thinned from trench rollback experienced as the Pacific plate rapidly descends into the mantle. There would be no initial uplift in the upper plate before the slab subducts because there is no convergence driving the plates together. The sequence of melting remains the same as previous models.

The work performed here gives no indication of whether subduction initiation was induced or spontaneous, but it does shed some light on what happens in the mantle regardless of initiation style. Both types of initiation require the mantle to undergo decompression melting then fluid flux melting, which creates different types of volcanics observed in the arc.

CHAPTER V

CONCLUSION

Modeling the evolution of fore arc magmatic processes is much more complex than originally believed. While it is possible to model FAB from a DMM source melt, in order to model boninite from the FAB an additional melt must be added. Theoretically, it is possible to match all samples on a spinel melt model that spans lherzolite to harzburgite field melt, but extreme amounts of melt, >70%, are required to match the most depleted HSB sample. In addition to the extreme melts to match HREE patterns, some amount of sediment melt from the descending plate must be incorporated to enrich the LREE concentrations relative to the MREE in the boninite samples.

Those elements that are enriched likely come from two sources: sediment melt and fluid from the descending slab, as well as seawater alteration post eruption. To determine the input from the slab, we use HFSE that are immobile at low temperature alteration such as Hf, Nb, and Zr. To determine the sea water alteration, we look to those FME Rb, Ba, Pb, and Sr. In many samples, all the elements considered here are enriched, and all samples have enrichments in multiple combinations of the elements. This indicates that element enrichment takes place during and after genesis of the samples.

Chemostratigraphy of the core tracks the magmatic evolution of the fore arc system, particularly for the core U1439C and U1442A. The base of the cores shows a transition from FAB into boninite with emphasis on the elements Cr,

TiO_2, Zr, and Al_2O_3 (Figures 24-27). LSB is erupted initially for both cores with some interbedded HMA and minor BB. The upper portion of the core is dominated by HSB with minor BB and one sample of LSB in core U1493C. This indicates a changing magmatic system from FAB to LSB to HSB. BB is syngenetically produced throughout the boninite regime.

The FAB dominated cores U1440B and U1441A have similar chemistry throughout the cores with same major difference between units. Units 1, 3, and 5 in U1440B show large variation and possibly a magma mixing signature. U1441A has too few samples between the units to determine a lot about them, however it does appear to be more altered up section.

Magma mixing is observed petrographically and chemically in cores U1439C and U1442A, supporting the idea that two melts may mix to form the boninite melt. The models here use a second melt of 25% FAB melt to bring the modeled REE concentrations up to match the observed REE. The actual melt may have different concentrations of elements, greater or less percent melt, or could be a completely different melt altogether.

These observations and models allow us to create a simplified model of the magmatic evolution of the fore arc of a nascent subduction zone immediately after subduction initiates. Our fore arc model is supported by the geochemical models of Leng and others in several papers (Hall et al., 2003; Gurnis et al., 2004; Leng and Gurnis, 2011; Leng et al., 2012). While the geometry of subduction initiation changes and the effects of the crust may change, the genesis of the magmas remains similar throughout the proposed models.

REFERENCES

Adam J., and Green T., 2006, Trace element partitioning between mica- and amphibole-bearing garnet lherzolite and hydrous basanitic melt: 1. Experimental results and the investigation of controls on partitioning behavior: Contributions to Mineralogy and Petrology, v. 152, p. 1-17, doi:10.1007/s00410-006-0085-4.

Arculus, R.J., Pearce, J.A., Murton, B.J., and Van der Laan, S.R., 1992, Igneous stratigraphy and major element geochemistry of Holes 786A and 786B: In Proceedings of the Ocean Drilling Program, Scientific Results, v. 125, p. 143-169. Ocean Drilling Program, College Station, TX.

Arculus, R., et al., 2015, A record of spontaneous subduction initiation in the Izu-Bonin-Mariana arc: Nature Geoscience, v. 8, no. 9, p. 728–733, doi: 10.1038/ngeo2515.

Barth, M.G., and Gluhak, T.M., 2009, Geochemistry and tectonic setting of mafic rocks from the Othris Ophiolite, Greece: Contributions to Mineralogy and Petrology, v. 157, p. 23-40, doi:10.1007/s00410-008-0318-9.

Bédard, J.H., Lauzière, K., Tremblay, A., and Sangster, A., 1998, Evidence for forearc seafloor-spreading from the Betts Cove ophiolite, Newfoundland: oceanic crust of boninitic affinity: Tectonophysics, v. 284, p. 233–245, http://dx.doi.org/10.1016/S0040-1951(97)00182-0

Bloomer, S.H., 1983, Distribution and origin of igneous rocks from the landward slopes of the Mariana Trench: Implications for its structure and evolution:

Journal of Geophysical Research: Solid Earth, v. 88, p. 7411-7428.

Brenan J.M., Ryerson F.J., and Shaw H.F., 1998, The role of aqueous fluids in the slab-to-mantle transfer of boron, beryllium, and lithium during subduction: Experiments and models: Geochimica et Cosmochimica Acta, V. 62, p. 3337-3347, http://doi.org/10.1016/S0016-7037(98)00224-5.

Brenan, J.M., Shaw, H.F., and Ryerson, F.J., 1995, Experimental evidence for the origin of lead enrichment in convergent-margin magmas: Nature v. 378, p. 54.

Cameron, W.E., Nisbet, E.G., and Dietrich, V.J., 1979, Boninities, komatiites and ophiolitic basalts: Nature, v. 280, p. 550-553, doi:10.1038/280550a0.

Canil, D., 1999, Vanadium partitioning between orthopyroxene, spinel and silicate melt and the redox states of mantle source regions for primary magmas: Geochimica et Cosmochimica Acta, v. 63, p. 557-572. http://doi.org/10.1016/S0016-7037(98)00287-7.

Coish, R. A., Hickey, R., and Frey, F. A.,1982, Rare earth element geochemistry of the Betts Cove ophiolite, Newfoundland: complexities in ophiolite formation: Geochimica et Cosmochimica Acta, v. 46, p. 2117-2134, https://doi.org/10.1016/0016-7037(82)90189-2.

Cosca, M., Arculus, R., Pearce, J., and Mitchell, J., 1998, 40Ar/ 39Ar and K-Ar geochronological age constraints for the inception and early evolution of the Izu-Bonin - Mariana arc system: The Island Arc, v. 7, no. 3, p. 579–595, doi: 10.1111/j.1440-1738.1998.00211.x

Crawford, A.J., Falloon, T.J., and Green, D.H.,1989, Classification, petrogenesis

and tectonic setting of boninites: Boninites and related rocks, p. 1-49.

DeBari, S., Taylor, B., Spencer, K., and Fujioka, K., 1999, A trapped Philippine Sea plate origin for MORB from the inner slope of the Izu–Bonin trench: Earth and Planetary Science Letters, v. 174, no. 1-2, p. 183–197, doi: 10.1016/S0012-821X(99)00252-6.

Deschamps, A., and Lallemand, S., 2003, Geodynamic setting of Izu-Bonin-Mariana boninites: Geological Society, London, Special Publications, v. 219, p. 163-185. doi: 10.1144/GSL.SP.2003.219.01.08.

Dilek, Y., and Furnes, H., 2009, Structure and geochemistry of Tethyan ophiolites and their petrogenesis in subduction rollback systems: Lithos, v. 113, p. 1-20, http://doi.org/10.1016/j.lithos.2009.04.022.

Dilek, Y., Furnes, H., and Shallo, M., 2007, Suprasubduction zone ophiolite formation along the periphery of Mesozoic Gondwana: Gondwana Research, v. 11, p. 453-475, http://doi.org/10.1016/j.gr.2007.01.005.

Dilek, Y., Furnes, H., and Shallo, M., 2008, Geochemistry of the Jurassic Mirdita Ophiolite (Albania) and the MORB to SSZ evolution of a marginal basin oceanic crust: Lithos, v. 100, p. 174-209, http://doi.org/10.1016/j.lithos.2007.06.026.

Elkins, L., Gaetani, G., and Sims, K., 2008, Partitioning of U and Th during garnet pyroxenite partial melting: Constraints on the source of alkaline ocean island basalts: Earth and Planetary Science Letters, v. 265, p. 270-286, http://doi.org/10.1016/j.epsl.2007.10.034.

Falloon, T.J., and Crawford, A.J., 1991, The petrogenesis of high-calcium boninite

lavas dredged from the northern Tonga ridge: Earth and Planetary Science Letters, v. 102, p. 375-394, https://doi.org/10.1016/0012-821X(91)90030-L.

Falloon, T.J., and Danyushevsky, L.V., 2000, Melting of refractory mantle at 1· 5, 2 and 2· 5 GPa under anhydrous and H2O-undersaturated conditions: implications for the petrogenesis of high-Ca boninites and the influence of subduction components on mantle melting: Journal of Petrology, v. 41, p. 257-283, https://doi.org/10.1093/petrology/41.2.257.

Gaetani, G.A., and Grove, T.L., 1998, The influence of water on melting of mantle peridotite: Contrib Mineral Petrol, v. 131, p. 323, doi:10.1007/s004100050396.

Gaetani, G.A., Kent, A.J.R., Grove, T.L., Hutcheon, I.D., and Stolper, E.M., 2003, Mineral/melt partitioning of trace elements during hydrous peridotite partial melting: Contrib Mineral Petrol, v. 145, p. 391-405, doi:10.1007/s00410-003-0447-0.

Gerya, T.V., and Meilick, F.I., 2010, Geodynamic regimes of subduction under an active margin: effects of rheological weakening by fluids and melts: Journal of Metamorphic Geology, v. 29, p. 7-31, doi:10.1111/j.1525-1314.2010.00904.x.

Green, T.H., Blundy, J.D., Adam, J., and Yaxley, G.M., 2000, SIMS determination of trace element partition coefficients between garnet, clinopyroxene and hydrous basaltic liquids at 2-7.5 Gpa and 1080-1200C.: Lithos, v. 53, p. 165-187, http://doi.org/10.1016/S0024-4937(00)00023-2.

Green, D.H., 1973, Experimental melting studies on a model upper mantle composition at high pressure under water saturated and water-undersaturated conditions: Earth Planet. Sci. Lett., v. 19, p. 37–53, doi:10.1016/0012-821X(73)90176-3.

Gurnis, M., Hall, C., and Lavier, L., 2004, Evolving force balance during incipient subduction: Geochemistry, Geophysics, Geosystems, v. 5, p. 7, 10.1029/2003GC000681.

Hall, C.E., Gurnis, M., Sdrolias, M., Lavier, L.L., and Müller, R.D., 2003, Catastrophic initiation of subduction following forced convergence across fracture zones: Earth and Planetary Science Letters, v. 212, p. 15-30, http://doi.org/10.1016/S0012-821X(03)00242-5.

Hart, S.R., and Dunn, T., 1993, Experimental cpx/melt partitioning of 24 trace elements: Contributions to Mineralogy and Petrology, v. 113, p. 1-8, doi:10.1007/BF00320827.

Hauri, E.H., Wagner, T.P., and Grove, T.L., 1994, Experimental and natural partitioning of Th, U, Pb and other trace elements between garnet, clinopyroxene and basaltic melts: Chemical Geology, v. 117, p. 149-166, doi: 10.1016/0009-2541(94)90126-0.

Hickey-Vargas, R., 1989, Boninites and tholeiites from DSDP Site 458, Mariana forearc: Boninites and Related Rocks, p. 339-356.

Hickey, R., and Frey, F., 1982, Geochemical characteristics of boninite series volcanics: implications for their source: Geochimica et Cosmochimica Acta, v. 46, no. 11, p. 2099–2115, doi: 10.1016/0016-7037(82)90188-0.

Horn, I., Foley, S.F., Jackson, S.E., and Jenner, G.A., 1994, Experimentally determined partitioning of high field strength- and selected transition elements between spinel and basaltic melt: Chemical Geology, v. 117, p. 193-218, doi: 10.1016/0009-2541(94)90128-7.

Hussong, D.M., and Uyeda, S., 1982, Tectonic processes and the history of the Mariana arc-a synthesis of the results of deep-sea drilling Project Leg-60: Initial Reports of the Deep Sea Drilling Project, v. 60, p. 909-929.

Ishikawa, T., Nagaishi, K., and Umino, S., 2002, Boninitic volcanism in the Oman ophiolite: Implications for thermal condition during transition from spreading ridge to arc: Geology, v. 30, no. 10, p. 899, doi: 10.1130/0091-7613(2002)030<0899:BVITOO>2.0.CO;2.

Ishizuka, O., Kimura, J.-I., Li, Y., Stern, R., Reagan, M., Taylor, R., Ohara, Y., Bloomer, S., Ishii, T., Hargrove, U., and Haraguchi, S., 2006, Early stages in the evolution of Izu–Bonin arc volcanism: New age, chemical, and isotopic constraints: Earth and Planetary Science Letters, v. 250, no. 1-2, p. 385–401, doi: 10.1016/j.epsl.2006.08.007

Ishizuka, O., Tani, K., Reagan, M., Kanayama, K., Umino, S., Harigane, Y., Sakamoto, I., Miyajima, Y., Yuasa, M., and Dunkley, D., 2011, The timescales of subduction initiation and subsequent evolution of an oceanic island arc: Earth and Planetary Science Letters, v. 306, no. 3-4, p. 229–240, doi: 10.1016/j.epsl.2011.04.006.

Jean, M.M., Shervais, J.W., Choi, S.H., and Mukasa, S.B., 2010, Melt extraction and melt refertilization in mantle peridotite of the Coast Range ophiolite:

an LA–ICP–MS study: Contributions to Mineralogy and Petrology, v. 159, p. 113, doi:10.1007/s00410-009-0419-0.

Johannsen, A., 1937, A descriptive petrography of the igneous rocks: GFF, v. 59, p. 363-364, http://dx.doi.org/10.1080/11035893709444968

Johnson, K.T.M., Dick, H.J.B., and Shimizu, N., 1990, Melting in the oceanic upper mantle; an ion microprobe study of diopsides in abyssal peridotites: J Geophys Res, v. 95, p.2661-2678.

Johnson, K.T.M., 1998, Experimental determination of partition coefficients for rare earth and high-field-strength elements between clinopyroxene, garnet, and basaltic melt at high pressures: Contrib Mineral Petrol, v. 133, p. 60-68, doi:10.1007/s004100050437.

Johnson, L.E., and Fryer, P., 1990, The first evidence for MORB-like lavas from the outer Mariana forearc: geochemistry, petrography and tectonic implications: Earth and Planetary Science Letters, v. 100, p. 304–316, http://dx.doi.org/10.1016/0012-821X(90)90193-2

Keppler, H., 1996, Constraints from partitioning experiments on the composition of subduction-zone fluids: Nature, v. 380, p. 237.

Kikuchi, Y., 1890, On pyroxenic components in certain volcanic rocks from Bonin Island.

Klemme, S., and Blundy, J.D., 2002, Experimental constraints on major and trace element partitioning during partial melting of eclogite: Geochimica et Cosmochimica Acta, v. 66, p. 109-3,123, http://doi.org/10.1016/S0016-7037(02)00859-1.

Kostopoulos, D.K., and Murton, B.J., 1992, Origin and distribution of components in boninite genesis: significance of the OIB component: Geological Society, London, Special Publications, v. 60, p. 133-154, doi: 10.1144/GSL.SP.1992.060.01.08.

Kuroda, N., Shiraki, K., and Urano, H., 1978, Boninite as a possible calc-alkalic primary magma: Bulletin Volcanologique, v. 41, p. 563-575, doi:10.1007/BF02597387.

Leng, W., and Gurnis, M., 2011, Dynamics of subduction initiation with different evolutionary pathways: Geochemistry, Geophysics, Geosystems, v. 12, doi10.1029/2011GC003877.

Leng, W., and Gurnis, M., 2015, Subduction initiation at relic arcs: Geophysical Research Letters, v. 42, p. 7014-7021, doi10.1002/2015GL064985.

Leng, W., Gurnis, M., and Asimow, P., 2012, From basalts to boninites: The geodynamics of volcanic expression during induced subduction initiation: Lithosphere, vol. 4, p. 511-523, ddi10.1130/L215.1.

Macpherson, C. G., and Hall, R., 2001, Tectonic setting of Eocene boninite magmatism in the Izu–Bonin–Mariana forearc: Earth and Planetary Science Letters, vol. 186, p. 215-230, http://doi.org/10.1016/S0012-821X(01)00248-5.

Mallman, G., and O'Neill, H.S.C., 2009, The Crystal/Melt Partitioning of V during Mantle Melting as a Function of Oxygen Fugactiy Compared with some other Elements (Al, P, Ca, Sc, Ti, Cr, Fe, Ga, Y, Zr and Nb): Journal of Petrology, vol. 50, p. 1765-1794, https://doi.org/10.1093/petrology/egp053.

McDade, P., Blundy, J.D., and Wood, B.J., 2003, Trace element partitioning between mantle wedge peridotite and hydrous MgO-rich melt: Amer Min, vol. 88, p. 1825-1831, https://doi.org/10.2138/am-2003-11-1225.

McDonough, W.F., and Sun, S.S., 1995, The composition of the Earth: Chemical Geology, vol. 120, p. 223-253, https://doi.org/10.1016/0009-2541(94)00140-4.

Meijer, A., Anthony, E., and Reagan, M., 1982, Petrology of the fore-arc sites: Initial Rep. Deep Sea Drill. Proj., vol. 60, p. 709–730.

Meijer, A., Reagan, M., Ellis, H., Shafiqullah, M., Sutter, J., Damon, P., and Kling, S., 1983, Chronology of volcanic events in the eastern Philippine Sea: The Tectonic and Geologic Evolution of Southeast Asian Seas and Islands: Part 2, p. 349-359, DOI: 10.1029/GM027p0349.

Metcalf, R.V., and Shervais, J.W., 2008, Suprasubduction-zone ophiolites: Is there really an ophiolite conundrum?: Geological Society of America Special Papers, vol. 438, p. 191-222, doi: 10.1130/2008.2438(07).

Morris, J.D., and Hart, S.R., 1983, Isotopic and incompatible element constraints on the genesis of island arc volcanics from Cold Bay and Amak Island, Aleutians, and implications for mantle structure: Geochimica et Cosmochimica Acta, vol. 47, p. 2015-2030, https://doi.org/10.1016/0016-7037(83)90217-X.

Murton, B.J., Peate, D.W., Arculus, R.J., Pearce, J.A., and Van der Laan, S., 1992, 12. Trace-element geochemistry of volcanic rocks from site 786: the Izu-Bonin Forearc: Proceedings of Ocean Drilling Program, Scientific

Results, vol. 125, p. 211-235.

Niu, Y., 1997, Mantle melting and melt extraction processes beneath ocean ridges: evidence from abyssal peridotites: Journal of Petrology, vol. 38, p. 1047-1074, ddi: https://doi.org/10.1093/petroj/38.8.1047.

Parman, S.W., and Grove, T.L., 2004, Harzburgite melting with and without H2O: Experimental data and predictive modeling: J. Geophys. Res., vol. 109, doi:10.1029/ 2003JB002566.

Pearce J.A. and Robinson P.T., 2010, The Troodos ophiolitic complex probably formed in a subduction initiation, slab edge setting. Gondwana Research, vol. 18, Issue 1, p. 60–81: doi:10.1016/j.gr.2009.12.003.

Pearce, J.A., van der Laan, S.R., Arculus, R.J., Murton, B.J., Ishii, T., Peate, D.W., and Parkinson, I.J., 1992, Boninite and harzburgite from Leg 125 (Bonin-Mariana forearc): a case study of magma genesis during the initial stages of subduction: In Fryer, P., Pearce, J.A., Stokking, L.B., et al., Proceedings of the Ocean Drilling Program, Scientific Results, 125: College Station, TX (Ocean Drilling Program), p. 623–659. http://dx.doi.org/10.2973/odp.proc.sr.125.172.1992

Petersen, J., 1891, Der Boninit von Peel Island. Nachtrag zu den Beitragen zur Petrographie von Sulphur Island usw, Jahrb. Hambg. Wiss. Aust, vol. 8, p. 341-349.

Portnyagin, M.V., Danyushevsky, L.V., and Kamenetsky, V.S., 1997, Coexistence of two distinct mantle sources during formation of ophiolites: a case study of primitive pillow-lavas from the lowest part of the volcanic section of the

Troodos Ophiolite, Cyprus: Contributions to Mineralogy and Petrology, vol. 128, p. 287-301, doi:10.1007/s004100050309.

Reagan, M.K., Pearce, J.A., Petronotis, K., and the Expedition 352 Scientists, 2015, Izu-Bonin-Mariana fore arc: Testing subduction initiation and ophiolite models by drilling the outer Izu-Bonin-Mariana fore arc: Proceedings of the International Ocean Discovery Program Volume 352 publications.iodp.org

Reagan, M., et al., 2010, Fore-arc basalts and subduction initiation in the Izu-Bonin-Mariana system: Geochemistry, Geophysics, Geosystems, v. 11, no. 3, doi: 10.1029/2009GC002871

Reagan, M.K., McClelland, W.C., Girard, G., Goff, K.R., Peate, D.W., Ohara, Y., and Stern, R.J., 2013, The geology of the southern Mariana fore-arc crust: implications for the scale of Eocene volcanism in the western Pacific: Earth and Planetary Science Letters, vol. 380, p. 41. http://dx.doi.org/10.1016/j.epsl.2013.08.013

Robinson, J.A.C., and Wood, B.J., 1998, The depth of the spinel to garnet transition at the peridotite solidus: Earth and Planetary Science Letters, vol. 164, p. 277-284, http://doi.org/10.1016/S0012-821X(98)00213-1.

Rogers, N.W., MacLeod, C.J., and Murton, B.J., 1989, Petrogenesis of boninitic lavas from the Limassol Forest Complex, Cyprus: In Boninites and related rocks, pp. 288-313.

Rollinson, H., 1993, Using geochemical data: Evaluation, presentation, interpretation: Essex, England, Pearson Education Limited, Prentice Hall

Publishers, 352 p.

Salters, V.J.M., and Stracke, A., 2004, Composition of the depleted mantle: Geochem Geophys Geosyst, vol. 5, doi:10.1029/2003GC000597

Shervais, J., 1982, Ti-V plots and the petrogenesis of modern and ophiolitic lavas: Earth and Planetary Science Letters, v. 59, no. 1, p. 101–118, doi: 10.1016/0012-821X(82)90120-0

Shervais et al., 2016, Chemostratigraphy of subduction initiation: IODP Expedition 352 Boninite and FAB: Geological Society of America Abstracts with Programs, vol. 48, no. 7, doi: 10.1130/abs/2016AM-283837

Shiraki, K., and Kuroda, N., 1977, The boninite revisited: J. Geol. Soc. Japan, vol. 86, p. 34-55, http://doi.org/10.5026/jgeography.86.3_174

Sobolev, A.V., and Danyushevsky, L.V., 1994, Petrology and geochemistry of boninites from the north termination of the Tonga Trench: constraints on the generation conditions of primary high-Ca boninite magmas: Journal of Petrology, vol. 35, p. 1183-1211, ddi: https://doi.org/10.1093/petrology/35.5.1183.

Staudigel, H., Plank, T., White, B., and Schmincke, H. U., 1996, Geochemical fluxes during seafloor alteration of the basaltic upper oceanic crust: DSDP Sites 417 and 418:Subduction top to bottom, p. 19-38, DOI: 10.1029/GM096p0019.

Stern, R.J., 2002, Subduction zones: Rev. Geophys., vol. 40, p. 1012, doi:10.1029/2001RG000108, 2002.

Stern, R.J., Reagan, M., Ishizuka, O., Ohara, Y., and Whattam, S., 2012, To

understand subduction initiation, study forearc crust: To understand forearc crust, study ophiolites: Lithosphere, vol. 4, p. 469-483, DOI: 10.1130/L183.1

Stern, R.J., and Bloomer, S.H., 1992, Subduction zone infancy: examples from the Eocene Izu-Bonin-Mariana and Jurassic California arcs: Geological Society of America Bulletin, vol. 104, p. 1621–1636, http://dx.doi.org/10.1130/0016-7606(1992)104<1621:SZIEFT>2.3.CO;2

Sun, S.S., and Nesbitt, R.W., 1978, Geochemical regularities and genetic significance of ophiolitic basalts: Geology, vol. 6, p. 689-693, doi: 10.1130/0091-7613(1978) 6<689:GRAGSO> 2.0.CO;2.

Taylor, B., 1992, Rifting and the volcanic-tectonic evolution of the Izu-Bonin-Mariana arc: In Proceedings of the Ocean Drilling Program, Scientific Results, vol. 126, pp. 627-651.

Taylor, R.N., Lapierre, H., Vidal, P., Nesbitt, R.W., and Croudace, I.W., 1992, Igneous geochemistry and petrogenesis of the Izu-Bonin forearc basin: In Proceeding of the Ocean Drilling Program Scientific Results, pp. 311-316, Texas A & M University Ocean Drilling Program.

Taylor, R.N., and Nesbitt, R.W., 1994, Arc volcanism in an extensional regime at the initiation of subduction: a geochemical study of Hahajima, Bonin Islands, Japan: Geological Society, London, Special Publications, vol. 81, p. 115-134, doi: 10.1144/GSL.SP.1994.081.01.07.

Taylor, R.N., Nesbitt, R.W., Vidal, P., Harmon, R.S., Auvray, B., and Croudace, I.W., 1994, Mineralogy, chemistry, and genesis of the boninite series

volcanics, Chichijima, Bonin Islands, Japan: Journal of Petrology, vol. 35, p. 577-617, ddi: https://doi.org/10.1093/petrology/35.3.577.

Umino, S., and Kushiro, I., 1989, Experimental studies on boninite petrogenesis: in Crawford, A.J., ed., Boninite and related rocks: London, Unwin Hyman, p. 89–111.

Umino, S., Kitamura, K., Kanayama, K., Tamura, A., Sakamoto, N., Ishizuka, O., and Arai, S., 2015 Thermal and chemical evolution of the subarc mantle revealed by spinel-hosted melt inclusions in boninite from the Ogasawara (Bonin) Archipelago, Japan: Geology, vol. 43, p. 151-154, doi: 10.1130/G36191.1.

Van der Laan, S.R., Flower, M.F.J., and Koster van Groos, A.F., 1989, Experimental evidence for the origin of boninites: near-liquidus phase relations to 7.5 kbar. Boninites: Unwin Hyman, London, p. 112-147.

Walter, M.J., 1998, Melting of garnet peridotite and the origin of komatiite and depleted lithosphere: J Petrol, vol. 39, p. 29-60, ddi: https://doi.org/10.1093/petroj/39.1.29.

Witt-Eickschen, G., and O'Neil H.S.C., 2005, The effect of temperature on the equilibrium distribution of trace elements between clinopyroxene, orthopyroxene, olivine and spinel in upper mantle peridotite: Chem Geol, vol. 221, p. 65-101, http://doi.org/10.1016/j.chemgeo.2005.04.005.

Workman, R.K., and Hart, S.R., 2005, Major and trace element composition of the depleted MORB mantle (DMM): Earth and Planetary Science Letters, vol. 231, p. 53-72, http://doi.org/10.1016/j.epsl.2004.12.005

Wu, J., Suppe, J., Lu, R., and Kanda, R., 2016, Philippine Sea and East Asian plate tectonics since 52 Ma constrained by new subducted slab reconstruction methods: Journal of Geophysical Research: Solid Earth, vol. 121, p. 4670-4741, doi10.1002/2016JB012923.

Yuan, C., Sun, M., Zhou, M.F., Xiao, W., and Zhou, H., 2005, Geochemistry and petrogenesis of the Yishak Volcanic Sequence, Kudi ophiolite, West Kunlun (NW China): implications for the magmatic evolution in a subduction zone environment: Contributions to Mineralogy and Petrology, vol. 150, p. 195-211, doi:10.1007/s00410-005-0012-0.

APPENDICES

Appendix A. Geochemical Legend

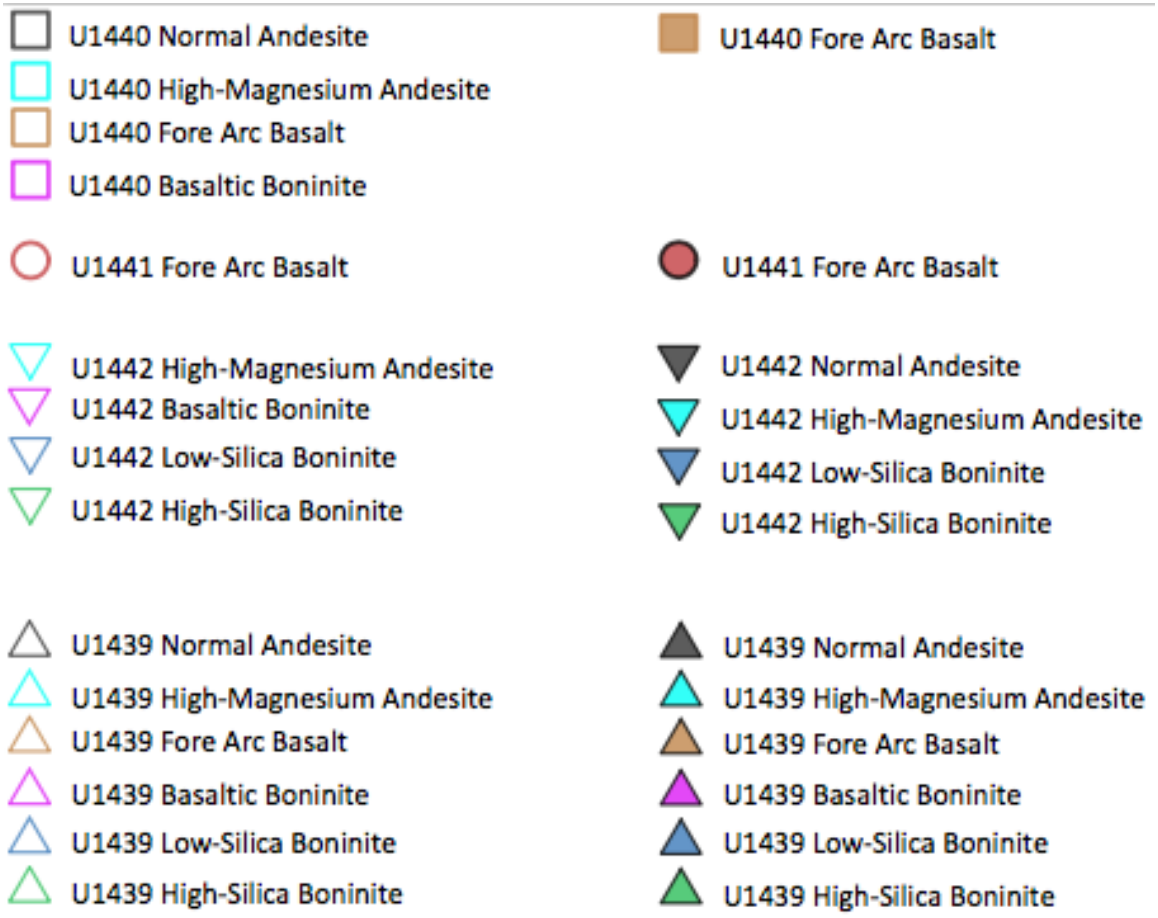

Appendix B. Geochemistry of core.

Table 1. IODP 352-U1440B. Major and trace element geochemistry.

Sample	10R-1-W 104/107	10R-1-W 39/42	10R-2-W 46/50	4R-1-W 126/129	4R-1-W 86/88	4R-2-W 15/18	6R-1-W 16/19
Depth (mbsf)	144.51	144.58	145.16	116.64	116.23	115.53	127.08
Lith. unit	2	2	2	2	2	2	2
Rock Type	FAB	FAB	FAB	FAB	FAB	FAB	FAB
Sum	101.50	98.93	98.65	97.65	97.78	96.57	98.07
LOI	0.04	-0.02	0.59	0.93	1.09	1.07	0.32
Total wFeO	100.12	97.54	97.74	96.98	97.69	96.21	96.95
SiO_2	50.60	50.89	52.39	49.04	50.35	50.39	52.32
TiO_2	0.96	0.93	0.98	1.22	0.61	1.13	0.96
Al_2O_3	15.50	15.11	14.07	16.97	16.11	15.54	14.14
Fe_2O_3	12.34	12.69	13.88	14.82	10.54	13.44	13.46
FeO*	11.10	11.42	12.49	13.34	9.48	12.09	12.11
MnO	0.18	0.19	0.20	0.16	0.13	0.18	0.20
MgO	6.97	7.11	6.39	4.33	7.98	5.97	6.64
CaO	11.83	11.80	10.83	11.35	12.85	11.60	11.03
Na_2O	2.60	2.20	2.18	2.92	2.03	2.53	2.25
K_2O	0.16	0.28	0.40	0.54	0.39	0.45	0.27
P_2O_5	0.09	0.08	0.08	0.13	0.07	0.12	0.08
Zr		7.8	11.5	17.3		26.4	5.9
Sr	84	76	78	99	87	88	84
Sc	35.4	47.1	38.2	40.9	37.4	41.3	42.5
V	405	398	383	494	270	418	373
Cr	85	78	65	51	301	35	34
Ni	58	65	50	45	93	48	48

Table 1. IODP 352-U1440B. (cont.)

Sample	10R-1-W 104/107	10R-1-W 39/42	10R-2-W 46/50	4R-1-W 126/129	4R-1-W 86/88	4R-2-W 15/18	6R-1-W 16/19
Lith. unit	2	2	2	2	2	2	2
Rock Type	FAB	FAB	FAB	FAB	FAB	FAB	FAB
Sc	42.0	37.9	36.2	41.6	44.4	44.4	36.8
V	393.8	377.0	384.9	462.5	304.5	424.1	372.6
Cr	55.8	51.6	42.9	42.0	290.0	41.8	20.7
Co	55.2	55.6	53.7	37.0	43.7	48.5	61.8
Ni	55.9	60.1	47.3	45.9	96.7	54.0	56.0
Rb	2.6	2.4	7.1	9.8	9.8	6.6	2.9
Sr	60.4	56.3	61.6	79.5	70.2	75.9	62.4
Y	22.6	22.1	23.5	26.9	14.7	27.7	25.6
Zr	36.4	34.0	35.5	47.2	15.8	44.2	36.5
Nb	0.947	0.871	0.953	1.229	0.664	1.284	0.977
Ba	8.6	4.9	17.4	14.2	6.4	7.2	20.7
La	1.570	1.435	1.572	1.981	1.343	1.864	1.682
Ce	4.940	4.626	4.992	6.124	3.151	5.418	5.271
Pr	0.871	0.821	0.845	1.082	0.597	1.000	0.916
Nd	4.943	4.692	4.963	6.276	3.295	5.621	5.186
Eu	0.794	0.764	0.774	0.957	0.549	0.881	0.812
Sm	1.945	1.868	1.927	2.435	1.274	2.255	2.090
Gd	3.008	2.938	3.146	3.698	2.068	3.584	3.273
Tb	0.564	0.548	0.556	0.673	0.377	0.682	0.605
Dy	4.023	3.955	4.117	4.869	2.580	4.739	4.351
Ho	0.893	0.871	0.917	1.064	0.598	1.056	0.976
Er	2.948	2.900	3.017	3.584	1.705	3.355	3.307
Tm	0.435	0.427	0.466	0.536	0.259	0.505	0.490
Yb	2.761	2.845	3.028	3.386	1.722	3.358	3.267
Lu	0.406	0.425	0.468	0.520	0.259	0.510	0.522
Hf	1.310	1.232	1.323	1.753	0.644	1.522	1.335
Ta	0.076	0.070	0.078	0.092	0.140	0.257	0.078
Pb	0.148	0.343	0.154	0.538	0.369	0.386	0.168
Th	0.106	0.091	0.101	0.127	0.071	0.134	0.101
U	0.235	0.307	0.075	0.396	0.201	0.414	0.037

Table 1. IODP 352-U1440B. (cont.)

Sample	7R-1-W 52/55	8R-1-W 112/115	8R-1-W 27/30	12R-1-W 128/129	12R-1-W 33/35	12R-1-W 82/86	12R-2-W 132/135
Depth (mbsf)	134.94	136.69	137.54	164.44	164.89	163.94	163.82
Lith. unit	2	2	2	3	3	3	3
Rock Type	FAB	FAB	FAB	FAB	FAB	FAB	FAB
Sum	98.81	100.96	100.80	97.88	99.27	99.86	98.05
LOI	0.58	0.61	0.42	0.54	-0.14	0.34	0.26
Total wFeO	97.94	99.50	99.26	97.26	97.68	99.10	96.77
SiO_2	50.86	51.44	51.52	50.13	51.09	50.97	49.93
TiO_2	0.95	0.98	0.92	0.57	0.99	0.56	1.35
Al_2O_3	14.64	14.86	14.36	16.02	14.84	15.77	14.72
Fe_2O_3	13.63	12.82	13.87	10.25	13.50	9.91	14.32
FeO*	12.26	11.53	12.48	9.23	12.15	8.92	12.88
MnO	0.21	0.22	0.19	0.17	0.20	0.16	0.20
MgO	6.98	7.11	6.83	8.24	6.44	8.22	6.51
CaO	11.54	11.30	11.08	13.41	11.48	13.31	11.34
Na_2O	2.17	2.22	2.17	1.71	2.31	1.67	2.46
K_2O	0.30	0.25	0.37	0.44	0.41	0.37	0.49
P_2O_5	0.09	0.08	0.08	0.08	0.10	0.06	0.13
Zr	17.5				4	18	17.5
Sr	71	95	90	78	79	56	79
Sc	46	47.5	42.4	43.2	34.6	47.7	35
V	373	410	401	254	417	272	490
Cr	59	68	49	257	56	231	108
Ni	53	71	53	99	50	97	73

Table 1. IODP 352-U1440B. (cont.)

Sample	7R-1-W 52/55	8R-1-W 112/115	8R-1-W 27/30	12R-1-W 128/129	12R-1-W 33/35	12R-1-W 82/86	12R-2-W 132/135
Lith. unit	2	2	2	3	3	3	3
Rock Type	FAB	FAB	FAB	FAB	FAB	FAB	FAB
Sc	38.5	43.7	44.1	40.9	44.6	42.0	43.5
V	368.9	394.7	390.9	268.3	425.4	277.7	500.4
Cr	26.9	48.0	28.8	238.4	42.4	239.8	99.3
Co	61.3	91.9	59.6	57.5	55.9	51.3	55.1
Ni	57.0	63.0	61.7	95.6	52.7	97.9	83.6
Rb	3.0	4.1	8.8	6.4	5.8	5.1	9.7
Sr	59.2	64.7	65.1	53.4	63.4	52.8	64.8
Y	26.1	26.0	23.4	15.4	24.6	15.7	33.4
Zr	37.0	36.2	36.1	21.3	36.8	21.6	54.1
Nb	0.974	1.009	1.783	0.577	0.995	0.570	1.226
Ba	6.2	16.8	13.7	6.4	13.7	5.1	9.8
La	1.706	1.656	1.477	0.970	1.584	1.008	1.872
Ce	5.153	5.064	4.662	3.035	4.917	3.061	6.155
Pr	0.930	0.899	0.850	0.525	0.887	0.550	1.148
Nd	5.419	5.094	4.606	3.058	5.046	3.096	6.567
Eu	0.826	0.813	0.758	0.487	0.792	0.503	1.018
Sm	2.103	1.976	1.888	1.199	2.013	1.252	2.786
Gd	3.352	3.216	3.004	1.958	3.144	1.936	4.407
Tb	0.609	0.597	0.596	0.362	0.590	0.375	0.813
Dy	4.466	4.319	3.963	2.592	4.314	2.741	5.688
Ho	1.011	0.977	0.938	0.595	0.950	0.610	1.292
Er	3.387	3.056	2.819	1.942	3.065	1.912	4.156
Tm	0.504	0.459	0.469	0.291	0.447	0.291	0.596
Yb	3.386	3.099	2.820	1.887	2.862	1.918	3.892
Lu	0.511	0.476	0.465	0.285	0.449	0.295	0.599
Hf	1.332	1.231	1.494	0.772	1.314	0.745	1.888
Ta	0.073	0.106	0.785	0.057	0.084	0.058	0.101
Pb	0.181	0.244	1.755	0.200	0.364	0.151	0.492
Th	0.097	0.102	0.194	0.067	0.097	0.072	0.126
U	0.567	0.174	0.079	0.140	0.393	0.170	0.360

Table 1. IODP 352-U1440B. (cont.)

Sample	12R-2-W 20/24	12R-2-W 41/44	13R-1-W 117/120	13R-1-W 49/52	15R-1-W 55/58	17R-1-W 70/72	18R-1-W 117/121
Depth (mbsf)	164.03	164.94	193.21	174.49	193.27	212.91	220.74
Lith. unit	3	3	4	4	4	5	5
Rock Type	FAB	FAB	FAB	FAB	FAB	FAB	FAB
Sum	97.96	98.24	98.85	97.37	98.87	97.44	99.13
LOI	0.38	0.56	0.27	0.33	0.27	2.20	0.86
Total wFeO	97.21	97.65	97.55	96.16	97.57	98.24	98.50
SiO_2	50.28	50.40	50.15	49.92	49.79	48.93	50.32
TiO_2	0.57	0.58	1.34	1.36	1.36	0.95	1.13
Al_2O_3	16.10	15.98	14.76	14.88	14.93	15.88	14.86
Fe_2O_3	9.97	10.24	14.45	14.38	14.43	12.44	13.85
FeO*	8.97	9.21	13.00	12.94	12.99	11.19	12.46
MnO	0.17	0.16	0.20	0.20	0.19	0.19	0.19
MgO	8.29	8.23	6.35	6.35	6.33	6.62	6.68
CaO	13.43	13.25	11.33	11.43	11.33	13.13	11.34
Na_2O	1.69	1.67	2.38	2.44	2.52	2.42	2.41
K_2O	0.43	0.45	0.37	0.35	0.42	0.55	0.50
P_2O_5	0.07	0.06	0.12	0.12	0.14	0.14	0.09
Zr			23.6	19.2	19.2	11.5	44.9
Sr	75	72	77	77	86	93	61
Sc	37.1	44.9	45.1	41.2	35.8	43.5	34
V	263	266	465	457	516	364	434
Cr	270	232	78	98	112	247	92
Ni	109	95	71	77	66	109	72

Table 1. IODP 352-U1440B. (cont.)

Sample	12R-2-W 20/24	12R-2-W 41/44	13R-1-W 117/120	13R-1-W 49/52	15R-1-W 55/58	17R-1-W 70/72	18R-1-W 117/121
Lith. unit	3	3	4	4	4	5	5
Rock Type	FAB	FAB	FAB	FAB	FAB	FAB	FAB
Sc	41.4	40.7	42.1	43.8	43.0	38.4	42.7
V	277.0	273.8	466.7	469.3	495.8	347.6	425.0
Cr	241.5	235.5	94.9	96.8	101.3	212.8	108.9
Co	51.3	49.2	50.6	53.8	52.5	53.0	57.6
Ni	102.1	90.3	73.9	90.3	74.5	117.9	85.6
Rb	6.0	6.8	5.4	5.3	8.3	6.0	10.0
Sr	53.7	52.1	62.9	64.1	65.5	74.3	64.3
Y	15.1	15.3	34.7	35.2	32.1	24.8	26.6
Zr	21.5	21.5	54.3	53.8	52.8	41.0	43.2
Nb	0.575	0.590	1.198	1.188	1.198	0.882	1.002
Ba	6.7	4.5	7.1	7.0	9.6	17.3	19.4
La	0.978	1.010	1.897	1.932	1.870	1.671	1.568
Ce	2.997	3.063	6.091	6.444	6.039	4.856	5.101
Pr	0.531	0.535	1.143	1.162	1.123	0.884	0.921
Nd	3.056	3.040	6.558	6.753	6.481	5.068	5.280
Eu	0.496	0.512	1.002	1.028	1.008	0.760	0.853
Sm	1.217	1.210	2.700	2.823	2.689	1.985	2.221
Gd	1.838	1.863	4.282	4.364	4.204	3.098	3.429
Tb	0.360	0.365	0.816	0.837	0.804	0.583	0.639
Dy	2.586	2.559	5.786	5.882	5.551	4.136	4.651
Ho	0.598	0.592	1.309	1.312	1.229	0.929	1.030
Er	1.861	1.936	4.124	4.268	3.978	2.997	3.265
Tm	0.285	0.278	0.614	0.652	0.586	0.459	0.468
Yb	1.830	1.892	4.132	4.253	3.861	2.995	3.104
Lu	0.279	0.290	0.640	0.642	0.588	0.454	0.463
Hf	0.738	0.759	1.845	1.834	1.854	1.406	1.551
Ta	0.060	0.053	0.084	0.099	0.112	0.098	0.100
Pb	0.156	0.184	0.936	0.843	0.623	1.135	0.417
Th	0.064	0.070	0.114	0.116	0.116	0.106	0.101
U	0.183	0.159	0.490	0.522	0.225	0.140	0.362

Table 1. IODP 352-U1440B. (cont.)

Sample	18R-1-W 4/9	18R-1-W 52/55	19R-1-W 2/6	19R-1-W 42/44	20R-1-W 5/8	21R-1-W 52/56	22R-1-W 5/9
Depth (mbsf)	221.39	220.27	227.13	226.74	231.77	236.94	242.13
Lith. unit	5	5	6	6	7	7	7
Rock Type	FAB	FAB	FAB	FAB	FAB	FAB	FAB
Sum	98.15	98.50	99.64	97.27	97.11	97.34	98.78
LOI	0.79	1.11	0.35	1.93	0.97	0.93	0.94
Total wFeO	97.49	98.14	98.56	97.78	96.68	96.87	98.31
SiO_2	50.38	49.59	52.15	52.70	50.18	50.48	50.37
TiO_2	1.29	1.17	1.02	1.09	1.07	1.08	1.05
Al_2O_3	15.46	15.17	14.68	14.68	14.96	15.15	15.33
Fe_2O_3	13.12	13.38	13.37	13.16	13.04	12.87	12.81
FeO*	11.81	12.04	12.03	11.84	11.73	11.58	11.53
MnO	0.19	0.19	0.21	0.15	0.17	0.18	0.17
MgO	6.26	6.68	5.67	6.46	7.54	7.29	7.39
CaO	11.80	12.19	10.63	8.83	11.30	11.36	11.20
Na_2O	2.34	2.35	2.84	3.13	2.40	2.42	2.37
K_2O	0.34	0.49	0.62	0.90	0.51	0.36	0.49
P_2O_5	0.13	0.13	0.17	0.22	0.12	0.10	0.11
Zr	23.9	13.4	120.9	126.6	22.5	11.7	13.2
Sr	75	81	58	65	59	69	67
Sc	42.9	40.1	34.7	35.1	35.7	43.9	38.9
V	444	447	289	273	437	396	381
Cr	180	136	80	62	132	108	125
Ni	90	78	55	57	74	75	77

Table 1. IODP 352-U1440B. (cont.)

Sample	18R-1-W 4/9	18R-1-W 52/55	19R-1-W 2/6	19R-1-W 42/44	20R-1-W 5/8	21R-1-W 52/56	22R-1-W 5/9
Lith. unit	5	5	6	6	7	7	7
Rock Type	FAB	FAB	FAB	FAB	FAB	FAB	FAB
Sc	44.0	43.4	39.1	31.8	41.4	41.2	41.6
V	445.8	458.4	302.6	246.4	426.7	381.5	376.3
Cr	175.2	120.9	59.5	62.6	114.9	92.0	121.0
Co	50.4	57.0	40.9	37.8	50.1	54.5	47.1
Ni	96.2	98.0	59.3	54.1	76.2	70.7	80.2
Rb	4.3	9.7	7.0	13.8	7.3	6.5	9.8
Sr	64.7	65.6	61.4	73.1	49.7	61.4	53.8
Y	35.5	27.8	61.5	75.9	26.2	28.3	25.8
Zr	50.8	44.9	112.1	141.5	38.3	40.9	38.2
Nb	1.108	1.041	2.241	3.546	0.797	0.985	0.848
Ba	6.5	15.3	15.6	10.8	5.0	6.1	4.7
La	1.953	1.695	3.883	4.731	1.302	1.593	1.359
Ce	6.275	5.211	12.214	15.465	4.403	4.943	4.451
Pr	1.130	0.984	2.172	2.814	0.794	0.930	0.834
Nd	6.521	5.639	12.942	15.909	4.935	5.413	4.929
Eu	1.012	0.887	1.644	2.007	0.772	0.865	0.817
Sm	2.755	2.304	5.057	6.218	2.042	2.201	2.111
Gd	4.314	3.632	7.985	9.689	3.270	3.534	3.205
Tb	0.829	0.662	1.508	1.863	0.629	0.691	0.635
Dy	5.948	4.613	10.441	12.832	4.502	4.861	4.538
Ho	1.361	1.041	2.348	2.947	1.019	1.099	1.014
Er	4.422	3.352	7.574	8.949	3.292	3.439	3.339
Tm	0.652	0.498	1.139	1.407	0.497	0.512	0.496
Yb	4.257	3.227	7.361	8.941	3.335	3.385	3.294
Lu	0.651	0.489	1.096	1.388	0.514	0.525	0.506
Hf	1.726	1.596	3.933	4.944	1.341	1.398	1.369
Ta	0.084	0.100	0.157	0.983	0.121	0.249	0.164
Pb	0.241	0.360	0.522	0.972		0.280	
Th	0.112	0.106	0.217	0.476	0.082	0.134	0.097
U	0.877	0.360	0.249	0.431	0.196	0.320	0.252

Table 1. IODP 352-U1440B. (cont.)

Sample	22R-1-W71/75	23R-1-W 64/68	24R-1-W 43/52	25R-1-W 5/9	25R-1-W 80/83	26R-1-W 52/55	27R-1-W 2/6
Depth (mbsf)	241.47	246.76	251.58	261.62	260.87	271.04	280.75
Lith. unit	7	7	7	8	8	8	9
Rock Type	FAB	FAB	FAB	FAB	FAB	FAB	FAB
Sum	100.89	97.46	98.45	98.56	97.44	98.40	101.26
LOI	0.93	0.79	0.79	0.76	0.85	0.29	1.04
Total wFeO	99.41	96.87	97.73	98.05	96.82	97.37	99.73
SiO_2	50.09	49.99	50.02	51.11	51.55	50.37	50.72
TiO_2	1.02	1.10	1.00	1.07	0.99	1.02	0.96
Al_2O_3	15.38	15.59	14.66	15.18	13.89	14.91	13.96
Fe_2O_3	13.03	12.75	13.96	11.40	13.80	11.98	13.70
FeO*	11.73	11.47	12.56	10.26	12.41	10.78	12.33
MnO	0.17	0.17	0.20	0.16	0.16	0.18	0.15
MgO	7.51	7.24	7.37	7.67	6.92	7.58	7.91
CaO	11.18	11.25	11.31	11.76	11.20	12.44	10.92
Na_2O	2.42	2.56	2.22	2.54	2.22	2.30	2.65
K_2O	0.41	0.52	0.55	0.15	0.57	0.30	0.33
P_2O_5	0.09	0.11	0.10	0.10	0.10	0.11	0.07
Zr		9.5	16.6	29	18.7	18.4	
Sr	78	72	58	74	69	74	79
Sc	51.8	32.6	45.5	38.4	30.8	39.8	26.2
V	406	401	407	317	309	354	393
Cr	127	109	81	252	236	272	122
Ni	88	69	76	119	82	101	78

Table 1. IODP 352-U1440B. (cont.)

Sample	22R-1-W71/75	23R-1-W 64/68	24R-1-W 43/52	25R-1-W 5/9	25R-1-W 80/83	26R-1-W 52/55	27R-1-W 2/6
Lith. unit	7	7	7	8	8	8	9
Rock Type	FAB	FAB	FAB	FAB	FAB	FAB	FAB
Sc	40.6	46.6	42.5	41.7	38.7	41.3	36.5
V	384.6	423.5	392.2	319.1	320.9	323.8	374.3
Cr	124.5	114.9	119.0	247.6	228.3	265.2	98.4
Co	48.9	51.1	50.1	62.1	41.7	45.7	47.3
Ni	81.2	73.1	78.5	118.7	81.1	93.0	70.0
Rb	8.4	9.9	10.1	2.8	17.9	4.9	10.9
Sr	49.9	56.8	57.4	64.3	55.3	57.8	51.6
Y	23.9	26.0	29.5	29.0	26.4	30.5	22.9
Zr	37.1	40.1	35.7	52.0	47.3	48.5	33.7
Nb	0.794	0.855	0.774	1.081	0.954	0.981	0.740
Ba	3.4	7.8	6.9	6.9	4.4	6.7	4.1
La	1.208	1.369	1.648	1.677	1.391	1.578	1.114
Ce	4.041	4.545	5.728	5.657	4.781	5.353	3.745
Pr	0.774	0.835	0.967	1.042	0.895	0.989	0.709
Nd	4.574	4.999	5.734	6.013	5.231	5.795	4.275
Eu	0.762	0.828	0.897	0.930	0.825	0.882	0.719
Sm	1.894	2.152	2.350	2.573	2.184	2.456	1.815
Gd	3.094	3.420	3.819	3.859	3.379	3.757	2.969
Tb	0.582	0.637	0.685	0.728	0.631	0.722	0.562
Dy	4.251	4.517	4.877	5.137	4.596	5.083	3.991
Ho	0.942	1.029	1.097	1.144	1.028	1.157	0.909
Er	3.121	3.251	3.592	3.582	3.248	3.660	2.822
Tm	0.460	0.483	0.520	0.549	0.497	0.559	0.455
Yb	3.082	3.181	3.391	3.593	3.306	3.638	3.002
Lu	0.463	0.473	0.518	0.548	0.510	0.556	0.466
Hf	1.296	1.431	1.314	1.844	1.592	1.660	1.241
Ta	0.100	0.072	0.063	0.078	0.067	0.078	0.073
Pb		0.433	0.858	0.379	0.288	0.262	
Th	0.084	0.087	0.096	0.113	0.094	0.099	0.063
U	0.165	0.313	0.107	0.249	0.072	0.245	0.043

Table 1. IODP 352-U1440B. (cont.)

Sample	27R-1-W 43/46	28R-1-W 1/4	28R-1-W 19/22	28R-1-W 43/46	29R-1-W 36/40	29R-1-W 59/63	29R-1-W 75/78
Depth (mbsf)	280.34	290.21	290.03	290.45	300.08	300.31	300.47
Lith. unit	9	10	10	10	12	12	12
Rock Type	FAB	FAB	FAB	FAB	FAB	FAB	FAB
Sum	101.43	101.29	101.63	101.83	101.55	101.09	101.63
LOI	1.05	1.82	1.32	0.56	1.64	0.51	0.79
Total wFeO	100.00	99.92	100.27	100.30	100.17	99.72	100.25
SiO_2	51.25	51.35	52.45	50.23	52.75	50.34	50.21
TiO_2	1.03	1.04	1.00	1.05	1.05	0.95	0.94
Al_2O_3	15.25	15.33	14.91	14.50	14.44	15.24	15.17
Fe_2O_3	12.48	11.93	11.83	13.81	12.31	12.00	12.16
FeO*	11.23	10.73	10.65	12.43	11.08	10.79	10.94
MnO	0.15	0.14	0.14	0.19	0.15	0.19	0.19
MgO	7.83	7.20	7.31	7.49	7.18	7.80	7.87
CaO	10.79	11.47	10.78	11.62	10.66	12.36	12.29
Na_2O	2.36	2.56	2.37	2.25	2.45	2.02	2.08
K_2O	0.03	0.11	0.31	0.16	0.16	0.23	0.22
P_2O_5	0.08	0.08	0.08	0.09	0.08	0.08	0.08
Zr		2.5	3.1	9.1	4.6	0.1	4.2
Sr	84	82	79	78	80	78	75
Sc	49.9	50.5	60.3	37.7	35.3	52.1	46.1
V	437	348	409	398	338	405	361
Cr	62	192	129	106	66	153	178
Ni	87	86	81	69	67	97	90

Table 1. IODP 352-U1440B. (cont.)

Sample	27R-1-W 43/46	28R-1-W 1/4	28R-1-W 19/22	28R-1-W 43/46	29R-1-W 36/40	29R-1-W 59/63	29R-1-W 75/78
Lith. unit	9	10	10	10	12	12	12
Rock Type	FAB	FAB	FAB	FAB	FAB	FAB	FAB
Sc	42.3	38.5	38.9	39.2	38.7	39.0	39.9
V	435.1	355.6	391.3	408.7	360.4	379.9	371.5
Cr	81.9	144.9	140.3	71.2	66.1	150.6	155.7
Co	58.4	51.0	47.2	52.9	48.1	56.3	52.0
Ni	74.1	81.5	75.5	67.3	60.5	91.8	83.6
Rb	0.2	1.6	8.3	5.0	3.6	2.0	2.7
Sr	53.2	60.0	57.6	56.2	57.6	55.9	56.0
Y	22.4	22.6	20.8	27.2	24.0	23.3	23.5
Zr	34.9	38.8	39.4	41.1	40.8	36.8	37.1
Nb	0.762	0.853	0.893	0.956	0.969	0.916	0.914
Ba	5.4	10.7	5.5	4.6	10.2	5.6	3.9
La	1.139	1.310	1.200	1.427	1.471	1.334	1.318
Ce	3.788	4.258	3.966	4.738	4.847	4.219	4.298
Pr	0.720	0.779	0.729	0.867	0.884	0.785	0.802
Nd	4.160	4.701	4.410	5.145	5.190	4.632	4.706
Eu	0.721	0.756	0.737	0.839	0.786	0.747	0.748
Sm	1.729	1.869	1.743	2.070	2.094	1.861	1.891
Gd	2.783	2.943	2.823	3.387	3.159	2.838	3.064
Tb	0.535	0.575	0.518	0.635	0.620	0.564	0.570
Dy	3.893	4.028	3.756	4.613	4.392	4.060	4.204
Ho	0.894	0.880	0.841	1.057	0.985	0.928	0.922
Er	2.822	2.785	2.603	3.380	3.147	2.997	2.916
Tm	0.422	0.414	0.383	0.515	0.449	0.456	0.425
Yb	2.782	2.695	2.568	3.322	3.010	3.068	2.922
Lu	0.423	0.408	0.366	0.504	0.442	0.452	0.441
Hf	1.240	1.303	1.382	1.451	1.482	1.270	1.323
Ta	0.075	0.070	0.090	0.086	0.087	0.084	0.074
Pb	0.386						
Th	0.075	0.088	0.083	0.091	0.093	0.089	0.089
U	0.049	0.348	0.452	0.135	0.618	0.164	0.204

Table 1. IODP 352-U1440B. (cont.)

Sample	30R-1-W 1/5	30R-1-W 38/42	30R-1-W 48/51	31R-1-W 12/17	31R-1-W 45/50	31R-1-W 93/95	32R-1-W 21/25
Depth (mbsf)	310.00	309.90	309.53	320.14	319.35	319.68	329.23
Lith. unit	13	13	13	14	14	14	15
Rock Type	FAB	FAB	FAB	FAB	FAB	FAB	FAB
Sum	102.09	101.39	101.15	101.74	100.00	101.84	102.06
LOI	2.18	1.80	1.47	1.64	3.43	2.80	1.07
Total wFeO	100.76	100.05	99.82	100.37	98.52	100.42	100.77
SiO_2	52.03	50.16	50.53	51.62	50.48	51.61	52.63
TiO_2	1.03	0.90	0.88	1.03	0.97	0.98	1.02
Al_2O_3	16.40	15.43	15.45	16.58	15.43	14.40	15.00
Fe_2O_3	12.04	11.82	11.48	12.26	13.27	12.65	11.41
FeO*	10.84	10.64	10.33	11.03	11.94	11.39	10.27
MnO	0.16	0.17	0.15	0.16	0.14	0.13	0.13
MgO	6.58	7.69	8.30	5.85	7.53	8.41	7.86
CaO	9.44	12.52	11.58	10.10	9.30	10.61	10.74
Na_2O	2.73	2.20	2.47	2.86	3.01	2.17	2.23
K_2O	0.69	0.20	0.22	0.67	1.07	0.21	0.05
P_2O_5	0.11	0.09	0.08	0.09	0.12	0.08	0.09
Zr	42.8			12.4		14.3	26.9
Sr	109	89	100	125	136	75	76
Sc	39.6	37.4	33.6	28.8	30.8	47.4	41.9
V	353	338	325	358	317	387	392
Cr	33	201	270	68	38	148	176
Ni	44	93	95	53	51	81	78

Table 1. IODP 352-U1440B. (cont.)

Sample	30R-1-W 1/5	30R-1-W 38/42	30R-1-W 48/51	31R-1-W 12/17	31R-1-W 45/50	31R-1-W 93/95	32R-1-W 21/25
Lith. unit	13	13	13	14	14	14	15
Rock Type	FAB	FAB	FAB	FAB	FAB	FAB	FAB
Sc	34.1	33.5	35.3	34.3	28.8	33.8	35.2
V	348.3	326.7	310.8	336.8	292.5	370.5	363.9
Cr	42.5	190.9	193.6	42.4	39.7	127.7	157.5
Co	39.1	42.7	48.7	41.3	37.6	48.8	52.6
Ni	44.0	80.5	89.4	45.6	45.4	75.1	78.4
Rb	7.7	4.5	12.5	9.5	13.7	5.4	0.2
Sr	99.8	63.0	65.8	101.1	89.8	58.1	59.7
Y	26.0	23.5	20.4	24.3	28.3	23.4	23.6
Zr	44.8	39.2	37.8	44.4	40.1	39.3	46.4
Nb	1.827	0.808	0.765	1.793	1.622	0.949	1.083
Ba	10.9	4.9	16.2	9.7	12.7	6.2	7.1
La	2.619	1.429	1.366	2.286	2.468	1.402	1.613
Ce	7.598	4.684	4.451	7.100	7.159	4.636	5.221
Pr	1.229	0.842	0.797	1.184	1.261	0.808	0.949
Nd	6.743	4.965	4.515	6.548	6.951	4.789	5.380
Eu	0.906	0.730	0.712	0.884	0.950	0.773	0.859
Sm	2.319	1.918	1.812	2.320	2.488	1.917	2.079
Gd	3.386	3.055	2.815	3.456	3.620	3.089	3.216
Tb	0.632	0.552	0.498	0.610	0.643	0.574	0.587
Dy	4.410	4.033	3.623	4.266	4.515	4.212	4.346
Ho	0.962	0.886	0.802	0.926	1.018	0.917	0.926
Er	3.056	2.816	2.448	3.005	3.236	2.961	2.954
Tm	0.459	0.426	0.358	0.429	0.488	0.457	0.447
Yb	3.086	2.924	2.396	2.873	3.172	2.944	3.007
Lu	0.469	0.436	0.344	0.440	0.504	0.450	0.444
Hf	1.548	1.376	1.275	1.516	1.429	1.388	1.536
Ta	0.158	0.081	0.067	0.127	0.125	0.076	0.080
Pb			0.359				
Th	0.150	0.088	0.080	0.162	0.144	0.090	0.101
U	0.110	0.269	0.167	0.117	0.175	0.389	0.062

Table 1. IODP 352-U1440B. (cont.)

Sample	33R-1-W 113/116	33R-1-W 22/25	33R-1-W 95/98	34R-1-W 17/21	34R-1-W 77/80	35R-1-W 17/20	35R-1-W 77/82
Depth (mbsf)	338.94	339.85	339.67	348.59	349.19	358.90	358.29
Lith. unit	15	15	15	15	15	15	15
Rock Type	FAB	FAB	FAB	FAB	FAB	FAB	FAB
Sum	101.91	101.35	101.50	101.14	101.52	101.94	101.27
LOI	0.80	1.48	1.86	1.34	1.04	1.71	2.27
Total wFeO	100.41	99.92	100.13	99.70	100.01	100.72	100.16
SiO_2	51.31	50.75	51.31	51.33	51.60	51.37	51.35
TiO_2	1.06	0.95	0.97	1.24	1.13	0.83	0.81
Al_2O_3	14.18	14.60	14.56	14.26	14.03	15.21	15.57
Fe_2O_3	13.56	12.72	12.16	12.94	13.60	10.59	9.51
FeO*	12.20	11.45	10.94	11.65	12.24	9.53	8.55
MnO	0.22	0.15	0.15	0.17	0.15	0.14	0.13
MgO	6.73	8.30	7.99	6.81	7.31	7.90	8.46
CaO	11.55	11.05	11.30	11.74	10.55	12.36	12.82
Na_2O	2.37	2.29	2.20	2.42	2.52	2.14	2.15
K_2O	0.29	0.39	0.51	0.30	0.40	0.43	0.07
P_2O_5	0.09	0.08	0.08	0.10	0.09	0.07	0.08
Zr	7.8		4	8	1.7		0.4
Sr	76	87	83	84	81	79	83
Sc	30.7	47	29.7	38.2	27.6	32.6	41.6
V	411	381	341	437	417	332	322
Cr	65	169	172	40	25	327	311
Ni	66	78	82	48	59	94	104

Table 1. IODP 352-U1440B. (cont.)

Sample	33R-1-W 113/116	33R-1-W 22/25	33R-1-W 95/98	34R-1-W 17/21	34R-1-W 77/80	35R-1-W 17/20	35R-1-W 77/82
Lith. unit	15	15	15	15	15	15	15
Rock Type	FAB	FAB	FAB	FAB	FAB	FAB	FAB
Sc	35.9	34.4	35.2	37.4	34.5	35.0	33.8
V	398.6	356.6	318.2	420.0	385.5	330.3	311.4
Cr	74.4	162.5	161.6	23.0	39.0	258.6	264.6
Co	50.6	38.8	41.6	55.7	46.3	47.1	51.0
Ni	62.8	70.6	77.6	48.7	56.7	87.3	97.7
Rb	41.7	17.8	28.5	19.0	57.8	32.9	0.3
Sr	57.9	58.7	58.4	60.7	56.6	59.8	57.9
Y	24.6	24.8	23.1	26.3	24.5	18.4	21.5
Zr	17.3	37.6	38.6	43.3	41.6	33.5	34.1
Nb	1.039	0.909	0.916	1.119	1.041	0.803	0.799
Ba	7.1	16.4	14.0	9.8	7.8	8.8	6.7
La	1.639	1.657	1.502	1.757	1.610	1.148	1.291
Ce	5.235	5.147	4.648	5.465	5.168	3.684	4.373
Pr	0.941	0.933	0.846	1.008	0.955	0.684	0.784
Nd	5.504	5.468	4.820	5.833	5.379	3.843	4.631
Eu	0.834	0.816	0.744	0.862	0.805	0.641	0.707
Sm	2.164	2.185	1.905	2.259	2.083	1.542	1.882
Gd	3.466	3.489	3.066	3.630	3.327	2.352	2.888
Tb	0.636	0.632	0.554	0.663	0.603	0.446	0.553
Dy	4.409	4.523	3.987	4.591	4.189	3.210	3.970
Ho	0.981	1.011	0.878	1.026	0.959	0.706	0.891
Er	3.075	3.299	2.795	3.228	3.064	2.302	2.745
Tm	0.473	0.469	0.421	0.476	0.446	0.351	0.429
Yb	3.138	3.069	2.829	3.169	3.110	2.364	2.881
Lu	0.457	0.468	0.411	0.482	0.456	0.362	0.445
Hf	0.857	1.328	1.367	1.542	1.497	1.122	1.136
Ta	0.084	0.076	0.071	0.086	0.079	0.063	0.064
Pb							
Th	0.060	0.088	0.084	0.095	0.095	0.083	0.076
U	0.086	0.094	0.065	0.180	0.105	0.443	0.055

Table 1. IODP 352-U1440B. (cont.)

Sample	36R-1-W 42/45	36R-1-W 93/96
Depth (mbsf)	368.24	368.75
Lith. unit	15	15
Rock Type	FAB	FAB
Sum	101.58	101.74
LOI	1.97	1.68
Total wFeO	100.27	100.47
SiO_2	51.43	51.25
TiO_2	0.85	0.82
Al_2O_3	15.02	15.24
Fe_2O_3	11.32	11.08
FeO*	10.19	9.97
MnO	0.14	0.14
MgO	9.18	9.17
CaO	11.00	11.27
Na_2O	2.07	2.02
K_2O	0.05	0.04
P_2O_5	0.07	0.07
Zr		
Sr	79	75
Sc	48.6	37.3
V	340	324
Cr	320	288
Ni	95	99

Table 1. IODP 352-U1440B. (cont.)

Sample	36R-1-W 42/45	36R-1-W 93/96
Lith. unit	15	15
Rock Type	FAB	FAB
Sc	38.3	35.8
V	347.3	321.5
Cr	275.5	267.2
Co	50.2	48.2
Ni	96.4	91.7
Rb	0.2	0.2
Sr	55.4	53.6
Y	17.7	16.9
Zr	31.2	28.8
Nb	0.747	0.669
Ba	5.3	5.2
La	1.086	1.048
Ce	3.476	3.353
Pr	0.629	0.608
Nd	3.659	3.439
Eu	0.601	0.606
Sm	1.489	1.417
Gd	2.282	2.261
Tb	0.427	0.420
Dy	3.044	3.053
Ho	0.692	0.683
Er	2.186	2.128
Tm	0.328	0.335
Yb	2.202	2.323
Lu	0.343	0.345
Hf	1.059	1.025
Ta	0.065	0.054
Pb		
Th	0.072	0.068
U	0.023	0.020

Table 2. IODP 352-U1441A. Major and trace element geochemistry.

Sample	10R-2-W 22/25	13R-1-W 42/45	16R-1-W 108/112	17R-1-W 35/38	19R-1-W 44/47	20R-1-W 31/34	20R-1-W 10/13
Depth (mbsf)	83.235	112.535	142.4	151.365	170.955	180.525	180.315
Lith. unit	1	1	1	2	3	4	4
Rock Type	FAB	FAB	FAB	FAB	FAB	FAB	FAB
Sum	101.38	100.47	101.44	100.28	100.54	99.92	101.05
LOI	2.32	4.53	3.30	0.88	1.72	0.95	0.25
Total wFeO	98.88	98.75	98.67	98.58	98.81	98.55	98.73
SiO_2	50.84	50.19	50.40	49.82	48.99	49.41	50.34
TiO_2	0.66	0.74	0.78	0.87	0.47	0.99	0.87
Al_2O_3	16.78	16.75	15.91	15.57	16.32	15.49	15.51
Fe_2O_3	9.97	11.13	11.96	12.61	10.18	12.70	11.22
FeO*	8.97	10.02	10.77	11.35	9.16	11.42	10.09
MnO	0.12	0.11	0.16	0.18	0.15	0.18	0.17
MgO	7.88	9.05	7.77	7.41	8.91	7.68	7.78
CaO	11.65	9.04	10.70	12.10	13.91	12.01	12.65
Na_2O	2.22	1.84	1.75	2.06	1.52	2.11	2.02
K_2O	0.81	2.19	1.64	0.57	0.49	0.61	0.49
P_2O_5	0.07	0.07	0.12	0.08	0.08	0.10	0.08
Zr			6.2				
Sr	99	93	100	86	73	90	81
Sc	35.4	40.1	47.8	43.5	40	45.2	40.7
V	285	259	325	354	254	390	331
Cr	105	108	118	157	591	222	212
Ni	84	81	89	95	161	88	95

Table 2. IODP 352-U1441A. (cont.)

Sample	10R-2-W 22/25	13R-1-W 42/45	16R-1-W 108/112	17R-1-W 35/38	19R-1-W 44/47	20R-1-W 31/34	20R-1-W 10/13
Lith. unit	1	1	1	2	3	4	4
Rock Type	FAB	FAB	FAB	FAB	FAB	FAB	FAB
Sc	34.9	35.9	37.9	53.9	34.8	39.1	38.2
V	266.9	248.3	285.2	462.6	263.7	383.9	335.8
Cr	85.4	86.7	85.9	193.7	481.3	199.6	155.7
Co	46.3	32.6	44.9	70.7	56.2	53.2	57.6
Ni	76.7	73.6	77.7	111.0	157.4	92.1	85.8
Rb	17.3	21.3	19.4	9.7	5.9	8.7	5.7
Sr	72.5	59.2	77.7	69.3	41.6	57.4	51.7
Y	13.9	16.7	25.9	26.4	12.7	24.5	21.3
Zr	28.9	31.1	33.0	41.5	14.2	37.2	30.8
Nb	0.620	0.681	0.708	1.038	0.281	0.765	0.773
Ba	11.2	13.0	33.7	14.2	9.6	10.4	9.5
La	1.248	1.611	3.435	1.506	0.517	1.301	1.286
Ce	3.791	3.837	4.918	5.152	1.667	4.407	4.015
Pr	0.646	0.809	1.098	0.914	0.311	0.799	0.752
Nd	3.512	4.491	5.821	5.393	1.927	4.728	4.443
Eu	0.543	0.665	0.801	0.878	0.374	0.776	0.714
Sm	1.359	1.654	2.012	2.213	0.857	1.935	1.793
Gd	2.005	2.466	3.178	3.595	1.518	3.225	2.892
Tb	0.360	0.443	0.581	0.654	0.282	0.581	0.541
Dy	2.617	3.077	4.124	4.850	2.100	4.301	3.782
Ho	0.564	0.664	0.947	1.047	0.499	0.952	0.847
Er	1.767	2.079	3.077	3.493	1.629	3.203	2.824
Tm	0.255	0.293	0.450	0.520	0.243	0.471	0.403
Yb	1.663	1.871	2.931	3.295	1.610	2.916	2.756
Lu	0.246	0.270	0.442	0.502	0.256	0.471	0.418
Hf	0.993	1.059	1.163	1.504	0.530	1.358	1.159
Ta	0.077	0.059	0.064	0.121	0.045	0.068	0.065
Pb	0.359	0.452	0.450	0.951	0.031	0.239	0.100
Th	0.086	0.088	0.098	0.127	0.037	0.081	0.087
U	0.182	0.254	0.285	0.488	0.139	0.279	0.460

Table 2. IODP 352-U1441A. (cont.)

Sample	21R-1-W 13/16	21R-1-W 60/63
Depth (mbsf)	190.045	190.515
Lith. unit	4	4
Rock Type	FAB	FAB
Sum	100.67	100.43
LOI	1.34	1.45
Total wFeO	98.66	98.68
SiO_2	50.22	50.28
TiO_2	0.98	0.99
Al_2O_3	15.51	15.83
Fe_2O_3	11.85	11.55
FeO*	10.67	10.39
MnO	0.16	0.15
MgO	8.03	7.94
CaO	11.65	11.31
Na_2O	2.25	2.41
K_2O	0.43	0.60
P_2O_5	0.10	0.11
Zr		
Sr	83	88
Sc	39.8	38.1
V	337	394
Cr	206	182
Ni	97	93

Table 2. IODP 352-U1441A. (cont.)

Sample	21R-1-W 13/16	21R-1-W 60/63
Lith. unit	4	4
Rock Type	FAB	FAB
Sc	37.6	42.3
V	338.7	377.2
Cr	181.8	201.3
Co	47.3	55.6
Ni	88.3	93.8
Rb	7.9	10.8
Sr	53.6	59.5
Y	25.7	25.5
Zr	34.8	37.2
Nb	0.730	0.798
Ba	3.8	7.7
La	1.310	1.336
Ce	4.365	4.389
Pr	0.787	0.821
Nd	4.725	4.794
Eu	0.761	0.791
Sm	1.992	2.051
Gd	3.248	3.275
Tb	0.591	0.617
Dy	4.349	4.388
Ho	0.968	0.991
Er	3.208	3.169
Tm	0.472	0.450
Yb	3.155	3.044
Lu	0.464	0.463
Hf	1.263	1.327
Ta	0.067	0.096
Pb	0.174	0.101
Th	0.073	0.085
U	0.301	0.310

Table 3. IODP 352-U1442A. Major and trace element geochemistry.

Sample	10R-3-W 43/46	12R-1-W 30/33	15R-1-W 54/58	16R-1-W 45/48	17R-1-W 80/83	19R-1-W 49/52	21R-1-W 64/67
Depth (mbsf)	83.935	101.515	119.26	123.965	131.215	150.405	169.955
Lith. unit	1a	1a	1b	1b	1c	1c	1c
Rock Type	HMA	HSB	HSB	HSB	HMA	HSB	HSB
Sum	98.63	99.07	98.33	96.67	97.72	97.31	97.97
LOI	1.64	1.57	2.51	3.76	2.49	3.09	1.96
Total wFeO	99.28	99.70	99.76	99.36	99.34	99.45	99.07
SiO_2	55.38	59.92	55.78	57.34	60.16	60.29	60.93
TiO_2	0.33	0.20	0.14	0.18	0.27	0.21	0.26
Al_2O_3	16.81	12.63	11.15	10.97	13.84	12.02	13.59
Fe_2O_3	8.78	8.22	8.83	8.64	7.43	7.99	7.11
FeO*	7.90	7.40	7.94	7.78	6.68	7.19	6.40
MnO	0.12	0.13	0.15	0.15	0.12	0.14	0.12
MgO	7.00	9.07	15.12	13.65	7.91	10.33	8.16
CaO	8.78	7.92	7.79	7.51	7.75	7.01	7.07
Na_2O	2.70	2.18	1.39	1.75	2.68	2.28	2.98
K_2O	0.92	0.51	0.51	0.62	0.54	0.49	0.46
P_2O_5	0.06	0.04	0.03	0.05	0.05	0.04	0.05
Zr	27	30.7	9.5	3.4	11.1	15	15.9
Sr	204	125	75	112	188	158	211
Sc	25	29.8	22.2	31.2	26.8	27.6	28.4
V	137	166	151	152	191	145	126
Cr	244	467	1204	937	300	543	394
Ni	106	117	277	276	94	111	129

Table 3. IODP 352-U1442A. (cont.)

Sample	10R-3-W 43/46	12R-1-W 30/33	15R-1-W 54/58	16R-1-W 45/48	17R-1-W 80/83	19R-1-W 49/52	21R-1-W 64/67
Lith. unit	1a	1a	1b	1b	1c	1c	1c
Rock Type	HMA	HSB	HSB	HSB	HMA	HSB	HSB
Sc	28.5	30.3	30.1	27.0	24.8	24.8	21.0
V	192.0	181.7	159.6	146.0	163.9	145.9	134.6
Cr	358.5	336.6	911.4	512.5	275.7	473.2	251.7
Co	56.9	62.3	73.0	65.1	51.2	58.9	54.9
Ni	94.0	111.7	273.3	261.0	84.2	110.9	127.7
Rb	12.9	13.7	12.4	14.8	10.8	11.4	8.9
Sr	138.7	122.6	72.2	95.1	169.5	141.3	191.9
Y	5.1	5.4	3.3	5.2	6.8	5.3	6.8
Zr	30.6	33.1	18.7	27.7	39.0	33.0	41.7
Nb	0.573	0.580	0.396	0.590	0.624	0.538	0.608
Ba	28.7	28.4	23.8	26.0	25.4	27.4	28.7
La	1.319	1.284	0.670	1.101	1.531	1.290	1.647
Ce	3.165	3.086	1.533	2.579	3.982	3.236	4.216
Pr	0.453	0.438	0.232	0.394	0.605	0.474	0.625
Nd	2.074	2.153	1.070	1.865	2.918	2.296	2.990
Eu	0.232	0.222	0.140	0.212	0.334	0.249	0.340
Sm	0.646	0.645	0.334	0.573	0.881	0.660	0.914
Gd	0.742	0.786	0.455	0.739	1.048	0.796	1.143
Tb	0.125	0.134	0.085	0.125	0.185	0.137	0.182
Dy	0.857	0.967	0.536	0.873	1.199	0.926	1.175
Ho	0.199	0.206	0.127	0.199	0.271	0.202	0.264
Er	0.597	0.634	0.393	0.599	0.805	0.600	0.771
Tm	0.094	0.102	0.063	0.090	0.117	0.095	0.113
Yb	0.685	0.723	0.483	0.666	0.804	0.672	0.804
Lu	0.111	0.115	0.082	0.107	0.131	0.100	0.120
Hf	0.941	0.964	0.550	0.800	1.192	0.989	1.219
Ta	0.066	0.071	0.056	0.056	0.074	0.053	0.057
Pb	1.846	1.347	1.335	1.268	1.686	1.189	2.474
Th	0.187	0.169	0.093	0.135	0.187	0.163	0.202
U	0.150	0.145	0.081	0.113	0.137	0.119	0.131

Table 3. IODP 352-U1442A. (cont.)

Sample	23R-1-W 5/9	24R-1-W 73/76	26R-1-W 89/92	28R-1-W 0/5	32R-1-W 1/5	36R-2-W 3/7	38R-1-W7/10
Depth (mbsf)	188.77	199.145	218.805	237.425	276.33	315.35	334.885
Lith. unit	1d	1d	1e	1e	2a	2b	2b
Rock Type	HMA	HMA	HMA	HSB	AND	HMA	LSB
Sum	97.80	90.45	89.30	96.29	98.41	103.07	98.09
LOI	2.72	10.07	6.03	4.67	1.45		
Total wFeO	99.61	99.54	94.35	99.94	99.00	102.12	97.17
SiO_2	61.66	55.42	55.08	58.33	57.50	54.58	53.52
TiO_2	0.24	0.32	0.32	0.19	0.42	0.35	0.31
Al_2O_3	12.54	16.75	16.65	11.43	17.71	16.72	15.35
Fe_2O_3	7.86	8.52	8.98	8.45	7.74	7.85	7.87
FeO*	7.08	7.67	8.08	7.60	6.97	7.07	7.08
MnO	0.13	0.14	0.12	0.14	0.10	0.13	0.12
MgO	7.86	7.66	7.08	12.89	3.65	7.63	10.03
CaO	7.08	8.20	8.97	6.93	9.85	11.16	11.19
Na_2O	2.93	2.72	2.71	1.86	3.08	2.09	2.16
K_2O	0.44	1.10	0.94	0.58	0.64	0.20	0.18
P_2O_5	0.05	0.03	0.06	0.04	0.10	0.07	0.06
Zr	23.2	28.3	24.4	21.1	32.3		
Sr	173	175	188	109	207	151	130
Sc	20.1	23.1	26.1	22.9	31.5	32.3	33.9
V	146	112	149	158	216	185	155
Cr	330	132	249	872	46	267	552
Ni	67	99	97	233	31	148	205

Table 3. IODP 352-U1442A. (cont.)

Sample	23R-1-W 5/9	24R-1-W 73/76	26R-1-W 89/92	28R-1-W 0/5	32R-1-W 1/5	36R-2-W 3/7	38R-1-W7/10
Lith. unit	1d	1d	1e	1e	2a	2b	2b
Rock Type	HMA	HMA	HMA	HSB	AND	HMA	LSB
Sc	26.9	27.5	28.3	26.8	26.0	26.9	28.0
V	141.5	128.8	158.1	147.8	221.7	200.0	178.7
Cr	294.9	112.8	202.3	596.9	34.7	228.9	413.1
Co	57.5	44.5	33.9	57.3	34.1	54.9	44.9
Ni	69.2	101.5	93.1	218.5	57.3	133.3	192.1
Rb	9.4	12.8	9.9	13.4	10.3	2.9	2.6
Sr	163.3	155.1	182.5	100.4	199.3	125.0	112.4
Y	6.7	4.0	11.7	4.6	10.5	8.2	7.4
Zr	40.5	53.1	43.9	28.4	41.5	28.7	24.5
Nb	0.626	0.830	0.657	0.520	0.691	1.309	0.483
Ba	28.7	10.5	6.9	22.4	26.6	8.5	9.0
La	1.361	0.747	2.173	0.980	1.779	1.017	0.907
Ce	3.509	2.239	9.872	2.392	4.716	2.842	2.640
Pr	0.525	0.355	1.279	0.360	0.719	0.508	0.450
Nd	2.568	1.790	6.637	1.703	3.764	2.578	2.369
Eu	0.302	0.280	0.819	0.197	0.464	0.380	0.326
Sm	0.821	0.609	2.192	0.529	1.195	0.904	0.793
Gd	1.074	0.730	2.611	0.677	1.548	1.169	1.103
Tb	0.186	0.131	0.405	0.115	0.280	0.237	0.189
Dy	1.257	0.811	2.401	0.762	1.819	1.446	1.309
Ho	0.275	0.172	0.475	0.169	0.407	0.319	0.286
Er	0.808	0.478	1.268	0.496	1.212	0.976	0.877
Tm	0.114	0.080	0.173	0.083	0.180	0.163	0.132
Yb	0.828	0.600	1.180	0.598	1.194	0.941	0.912
Lu	0.128	0.093	0.187	0.099	0.184	0.175	0.141
Hf	1.208	1.657	1.323	0.811	1.265	1.171	0.784
Ta	0.061	0.090	0.062	0.055	0.056	0.709	0.113
Pb	1.462	4.431	2.175	1.136	1.030	0.895	0.518
Th	0.149	0.281	0.192	0.140	0.149	0.169	0.080
U	0.109	0.167	0.105	0.110	0.146	0.116	0.109

Table 3. IODP 352-U1442A. (cont.)

Sample	39R-1-W 2/4	40R-1-W 67/70	43R-1-W 113/117	46R-1-W 47/50	47R-1-W 7/10	57R-1-W 84/88
Depth (mbsf)	344.63	354.985	384.65	413.285	422.685	520.96
Lith. unit	2b	2b	2b	3	3	4
Rock Type	LSB	HMA	HMA	HMA	HMA	LSB
Sum	99.32	97.83	97.95	94.73	99.22	97.88
LOI		2.53	1.45	3.98		
Total wFeO	98.35	99.49	98.60	97.81	98.30	97.18
SiO_2	54.13	58.76	62.90	55.01	54.56	53.75
TiO_2	0.35	0.40	0.47	0.37	0.37	0.27
Al_2O_3	15.86	14.93	16.08	17.09	17.56	19.39
Fe_2O_3	8.49	7.61	7.25	8.21	8.15	6.11
FeO*	7.64	6.85	6.52	7.39	7.34	5.50
MnO	0.13	0.09	0.06	0.12	0.13	0.04
MgO	8.26	6.21	2.90	7.18	7.09	9.29
CaO	11.28	9.58	6.57	9.86	10.08	8.73
Na_2O	2.09	2.71	3.76	2.58	2.51	2.82
K_2O	0.21	0.39	0.66	0.35	0.27	0.17
P_2O_5	0.06	0.07	0.08	0.05	0.09	0.04
Zr	6.7	9.1	34.5	16.8	10.4	
Sr	132	160	190	187	192	232
Sc	32.3	19.4	23.9	22.5	29.6	30.1
V	193	165	192	183	202	146
Cr	363	186	15	95	104	106
Ni	161	31	10	40	37	55

Table 3. IODP 352-U1442A. (cont.)

Sample	39R-1-W 2/4	40R-1-W 67/70	43R-1-W 113/117	46R-1-W 47/50	47R-1-W 7/10	57R-1-W 84/88
Lith. unit	2b	2b	2b	3	3	4
Rock Type	LSB	HMA	HMA	HMA	HMA	LSB
Sc	26.1	26.9	20.5	24.0	24.6	22.1
V	192.8	183.4	225.5	191.9	200.1	139.4
Cr	300.7	151.9	1.3	82.9	86.5	91.7
Co	43.6	34.6	27.3	31.7	38.7	30.5
Ni	147.5	33.8	14.5	54.0	35.8	54.4
Rb	3.6	14.9	9.1	6.2	4.6	1.3
Sr	117.0	139.8	172.7	171.9	171.5	197.2
Y	8.3	10.3	11.5	8.3	15.2	4.7
Zr	28.4	34.5	52.9	34.0	34.5	25.0
Nb	0.532	1.190	0.858	0.704	0.701	0.415
Ba	10.1	15.1	30.0	10.6	11.2	5.2
La	1.019	1.243	2.018	1.204	2.651	1.122
Ce	3.009	3.591	5.551	3.400	7.070	2.993
Pr	0.505	0.624	0.871	0.551	1.049	0.456
Nd	2.621	3.230	4.349	2.772	5.079	2.218
Eu	0.346	0.444	0.495	0.379	0.548	0.299
Sm	0.922	1.122	1.379	0.944	1.564	0.735
Gd	1.185	1.455	1.752	1.235	2.110	0.815
Tb	0.211	0.281	0.308	0.220	0.359	0.145
Dy	1.445	1.779	2.051	1.486	2.503	0.959
Ho	0.318	0.402	0.463	0.325	0.555	0.198
Er	1.004	1.207	1.327	1.020	1.696	0.579
Tm	0.149	0.191	0.195	0.157	0.245	0.078
Yb	1.000	1.282	1.333	1.058	1.634	0.544
Lu	0.155	0.195	0.193	0.168	0.248	0.078
Hf	0.838	1.284	1.579	1.049	1.012	0.756
Ta	0.122	0.554	0.065	0.194	0.195	0.081
Pb	0.560	0.500	1.268	1.054	1.427	0.830
Th	0.088	0.164	0.199	0.142	0.137	0.107
U	0.085	0.173	0.202	0.151	0.594	0.234

Table 4. IODP 352-U1439C. Major and trace element geochemistry.

Sample	2R-2-W 56/60	2R-3-W 15/18	4R-2-W 30/36	7R-1-W 20/24	9R-1-W 27/31	10R-1-W 15/19	12R-1-W 13/19
Depth (mbsf)	182.58	182.165	201.93	231.22	250.89	260.57	270.56
Lith. unit	1	1	3	3	5	5	5
Rock Type	BB	HSB	FAB	HSB	AND	LSB	
Sum	94.83	97.68	98.57	98.44	97.58	98.94	87.86
LOI	4.81	2.53	1.92	1.78	1.86		10.77
Total wFeO	98.63	99.09	99.18	99.27	98.61	97.87	97.60
SiO_2	52.05	56.10	52.20	60.36	56.05	54.18	49.21
TiO_2	0.21	0.15	0.28	0.18	0.44	0.30	0.36
Al_2O_3	13.00	10.51	17.12	12.71	19.86	12.20	13.30
Fe_2O_3	8.07	8.85	11.25	8.11	7.18	8.66	8.54
FeO*	7.27	7.97	10.12	7.30	6.46	7.79	7.68
MnO	0.14	0.15	0.16	0.13	0.09	0.14	0.14
MgO	12.66	16.15	5.50	8.88	2.31	14.53	9.25
CaO	11.90	6.99	9.76	7.49	7.39	8.33	15.77
Na_2O	2.05	1.46	3.10	2.33	4.51	2.02	2.22
K_2O	0.66	0.50	1.69	0.57	2.77	0.46	1.99
P_2O_5	0.06	0.03	0.08	0.04	0.11	0.05	0.07
Zr	20.6		14.4	18.1	47.1	1.9	
Sr	125	101	173	137	328	134	115
Sc	34.5	29.4	31.7	31	25	28.5	31.7
V	180	132	177	141	180	174	148
Cr	960	1220	673	521	1	1031	807
Ni	286	368	143	129	47	362	147

Table 4. IODP 352-U1439C. (cont.)

Sample	2R-2-W 56/60	2R-3-W 15/18	4R-2-W 30/36	7R-1-W 20/24	9R-1-W 27/31	10R-1-W 15/19	12R-1-W 13/19
Lith. unit	1	1	3	3	5	5	5
Rock Type	BB	HSB	FAB	HSB	AND	LSB	
Sc	27.0	25.7	34.0	23.9	17.8	30.0	28.7
V	180.2	149.4	205.9	161.7	168.9	177.0	152.1
Cr	785.9	788.1	371.4	382.0	14.5	448.9	403.2
Co	62.7	68.5	38.8	49.6	28.5	49.9	37.5
Ni	271.6	340.2	134.7	129.1	40.5	307.6	135.5
Rb	8.2	11.8	64.7	16.6	25.6	9.4	19.9
Sr	121.0	86.2	158.9	131.5	308.9	103.9	102.6
Y	5.57	3.92	7.27	4.82	11.36	8.63	13.51
Zr	30.9	20.8	43.9	32.8	67.6	26.5	26.2
Nb	0.656	0.471	0.890	0.613	0.859	0.502	0.512
Ba	18.2	22.0	42.9	32.3	65.6	13.2	34.1
La	1.254	0.868	1.889	1.140	3.446	1.088	2.624
Ce	3.021	2.085	4.773	2.743	7.682	2.762	2.645
Pr	0.446	0.312	0.642	0.406	1.255	0.506	1.174
Nd	2.147	1.471	3.079	1.901	5.893	2.689	5.924
Eu	0.243	0.162	0.341	0.200	0.650	0.368	0.649
Sm	0.644	0.439	0.905	0.554	1.734	0.923	1.880
Gd	0.769	0.545	1.079	0.650	2.056	1.233	2.299
Tb	0.138	0.098	0.189	0.120	0.333	0.232	0.389
Dy	0.937	0.646	1.240	0.804	2.005	1.495	2.471
Ho	0.214	0.152	0.284	0.186	0.443	0.339	0.555
Er	0.657	0.485	0.863	0.581	1.272	0.986	1.554
Tm	0.102	0.079	0.132	0.090	0.189	0.148	0.232
Yb	0.713	0.575	0.881	0.652	1.180	0.974	1.496
Lu	0.123	0.094	0.143	0.109	0.177	0.150	0.225
Hf	0.965	0.641	1.364	0.990	2.019	0.807	0.794
Ta	0.122	0.078	0.124	0.080	0.095	0.080	0.078
Pb	1.716	0.692	1.978	1.573	2.718	0.371	0.434
Th	0.156	0.120	0.220	0.150	0.392	0.068	0.066
U	0.203	0.101	0.464	0.124	0.274	0.143	0.094

Table 4. IODP 352-U1439C. (cont.)

Sample	14R-2-W 56/59	16R-3-W 81/85	17R-1-W 122/125	19R-5-W 5/10	20R-1-W 43/46	20R-3-W 15/18	24R-1-W 103/106
Depth (mbsf)	285.675	300.33	310.535	328.875	338.945	338.665	368.845
Lith. unit	6	6	6	6	6	6	6
Rock Type	LSB	LSB	LSB	LSB		LSB	LSB
Sum	95.91	94.74	97.24	98.99	99.38	99.12	94.55
LOI	4.64	5.68	3.27				5.91
Total wFeO	99.53	99.34	99.42	97.92	98.20	98.08	99.37
SiO_2	54.61	54.57	54.28	54.93	50.34	52.91	54.36
TiO_2	0.29	0.28	0.27	0.36	0.34	0.32	0.31
Al_2O_3	12.48	11.90	11.60	12.96	12.96	12.30	12.30
Fe_2O_3	8.14	8.47	8.51	8.80	9.58	8.47	8.45
FeO*	7.32	7.62	7.66	7.92	8.62	7.62	7.61
MnO	0.13	0.13	0.14	0.14	0.15	0.13	0.11
MgO	13.38	15.11	15.92	11.95	11.98	11.41	14.46
CaO	9.18	7.31	7.61	9.15	12.68	12.65	8.36
Na_2O	2.07	2.26	2.05	2.01	1.93	1.89	1.97
K_2O	0.49	0.78	0.43	0.54	0.88	0.72	0.51
P_2O_5	0.05	0.04	0.05	0.06	0.12	0.05	0.03
Zr	10.5	8.6	7.5	4	13.5		29.8
Sr	137	116	132	136	121	151	104
Sc	24	24.5	24.3	27.1	36.4	31.7	24.1
V	120	120	134	170	164	155	163
Cr	920	1083	1180	955	1180	935	1270
Ni	314	372	408	249	351	263	477

Table 4. IODP 352-U1439C. (cont.)

Sample	14R-2-W 56/59	16R-3-W 81/85	17R-1-W 122/125	19R-5-W 5/10	20R-1-W 43/46	20R-3-W 15/18	24R-1-W 103/106
Lith. unit	6	6	6	6	6	6	6
Rock Type	LSB	LSB	LSB	LSB		LSB	LSB
Sc	24.6	22.8	22.7	24.5	25.7	22.1	25.6
V	147.7	136.6	140.9	151.8	157.2	130.5	154.2
Cr		277.2	292.4	284.4	321.5	274.3	369.5
Co	67.4	63.6	67.1	65.1	43.3	39.2	57.5
Ni	293.5	351.1	385.4	347.1	220.1	221.4	451.1
Rb	7.0	11.3	6.3	6.7	8.0	10.5	7.5
Sr	122.8	103.8	116.8	120.4	119.4	118.3	99.2
Y	6.76	6.09	6.43	6.84	7.37	6.63	5.54
Zr	28.0	26.6	26.4	27.9	29.1	26.4	28.8
Nb	1.335	0.558	0.499	0.666	0.501	0.456	0.462
Ba	19.0	20.1	21.2	67.8	12.1	17.3	9.0
La	0.940	0.843	0.852	0.967	0.972	0.879	0.851
Ce	2.645	2.407	2.474	2.859	2.986	2.471	2.579
Pr	0.461	0.400	0.415	0.467	0.466	0.435	0.396
Nd	2.299	2.118	2.121	2.372	2.541	2.272	2.077
Eu	0.305	0.277	0.275	0.302	0.332	0.311	0.319
Sm	0.752	0.687	0.744	0.778	0.840	0.759	0.738
Gd	0.993	0.867	0.922	1.091	1.116	1.024	0.900
Tb	0.194	0.166	0.176	0.195	0.203	0.178	0.158
Dy	1.186	1.108	1.119	1.229	1.287	1.196	1.033
Ho	0.282	0.243	0.257	0.281	0.299	0.268	0.225
Er	0.805	0.733	0.768	0.820	0.863	0.797	0.649
Tm	0.135	0.110	0.121	0.135	0.133	0.127	0.100
Yb	0.823	0.716	0.771	0.804	0.868	0.821	0.627
Lu	0.140	0.111	0.127	0.134	0.136	0.128	0.097
Hf	1.228	0.823	0.814	0.885	0.866	0.820	0.838
Ta	0.782	0.166	0.134	0.260	0.057	0.041	0.056
Pb	2.065	0.570	1.264	1.086	0.449	1.046	0.540
Th	0.174	0.086	0.084	0.100	0.082	0.070	0.073
U	0.069	0.049	0.055	0.055	0.052	0.047	0.223

Table 4. IODP 352-U1439C. (cont.)

Sample	25R-2-W 87/90	26R-2-W 50/53	26R-3-W 8/11	27R-4-W 15/18	28R-3-W 12/15	31R-2-W 99/102	31R-4-W 102/105
Depth (mbsf)	378.485	387.815	387.395	397.165	406.935	437.105	437.135
Lith. unit	6	6	6	7	8	8	8
Rock Type	LSB	LSB		LSB	LSB	LSB	LSB
Sum	94.67	99.67	86.92	93.32	100.37	99.89	94.14
LOI	5.46		14.17	8.38			4.92
Total wFeO	98.96	98.55	99.87	100.53	99.37	98.71	97.87
SiO_2	53.22	54.03	48.25	52.94	53.07	53.09	52.90
TiO_2	0.28	0.30	0.30	0.23	0.21	0.21	0.20
Al_2O_3	10.66	11.77	11.29	11.10	11.24	10.54	10.45
Fe_2O_3	9.07	8.96	9.26	8.72	7.82	8.86	9.03
FeO*	8.16	8.06	8.33	7.84	7.03	7.97	8.13
MnO	0.15	0.09	0.11	0.13	0.13	0.14	0.14
MgO	16.83	14.87	12.66	18.07	14.32	19.05	19.19
CaO	8.58	7.98	15.96	7.51	11.77	6.90	6.90
Na_2O	1.74	2.10	1.77	1.76	1.80	1.64	1.64
K_2O	0.33	0.75	1.23	0.37	0.39	0.41	0.39
P_2O_5	0.05	0.05	0.10	0.04	0.04	0.04	0.04
Zr	7	4.3		1.4	20.8		2.3
Sr	122	121	129	120	145	101	93
Sc	23.9	21.6	31.1	20.9	30.6	20.9	26.1
V	130	161	178	88	146	93	116
Cr	1289	1329	1247	1385	1151	1678	1577
Ni	445	361	331	564	395	668	640

Table 4. IODP 352-U1439C. (cont.)

Sample	25R-2-W 87/90	26R-2-W 50/53	26R-3-W 8/11	27R-4-W 15/18	28R-3-W 12/15	31R-2-W 99/102	31R-4-W 102/105
Lith. unit	6	6	6	7	8	8	8
Rock Type	LSB	LSB		LSB	LSB	LSB	LSB
Sc	20.6	20.5	20.9	18.3	20.1	17.3	28.2
V	138.0	147.0	156.5	114.5	132.9	112.3	170.3
Cr	312.8	309.6	359.2	337.7	296.2	300.6	602.2
Co	59.1	50.1	63.8	54.9	53.3	56.1	51.9
Ni	416.3	298.3	295.2	490.4	337.5	562.3	242.5
Rb	4.4	8.3	9.7	6.0	5.8	7.6	8.2
Sr	107.7	96.1	108.4	103.8	130.2	84.6	103.4
Y	6.21	4.90	6.82	4.53	5.17	4.28	7.24
Zr	26.9	25.8	25.5	21.3	20.6	20.0	24.2
Nb	0.440	0.423	0.418	0.362	0.382	0.370	0.530
Ba	16.0	5.5	6.8	10.5	15.3	10.3	16.6
La	0.910	0.828	1.128	0.704	0.718	0.623	0.808
Ce	2.598	2.412	2.862	1.988	1.849	1.761	2.383
Pr	0.433	0.358	0.470	0.320	0.308	0.263	0.412
Nd	2.210	1.882	2.424	1.629	1.524	1.300	2.265
Eu	0.287	0.278	0.297	0.203	0.199	0.169	0.307
Sm	0.766	0.627	0.787	0.535	0.519	0.448	0.776
Gd	0.952	0.833	1.024	0.651	0.702	0.593	1.057
Tb	0.168	0.144	0.182	0.122	0.125	0.104	0.194
Dy	1.105	0.890	1.154	0.810	0.877	0.730	1.304
Ho	0.245	0.203	0.262	0.182	0.204	0.171	0.285
Er	0.759	0.571	0.785	0.572	0.657	0.529	0.833
Tm	0.114	0.084	0.114	0.086	0.102	0.081	0.130
Yb	0.763	0.565	0.766	0.583	0.686	0.521	0.836
Lu	0.116	0.084	0.118	0.089	0.110	0.085	0.125
Hf	0.786	0.803	0.779	0.640	0.657	0.592	0.713
Ta	0.051	0.046	0.063	0.045	0.045	0.039	0.051
Pb	0.264	0.168	0.502	1.231	0.400	0.037	
Th	0.067	0.066	0.072	0.066	0.069	0.062	0.068
U	0.051	0.138	0.150	0.048	0.051	0.042	0.143

Table 4. IODP 352-U1439C. (cont.)

Sample	32R-1-W 25/28	32R-4-W 120/123	35R-1-W 117/120	35R-2-W 76/79	37R-1-W 101/104	37R-2-W 31/34	39R-2-W 131/134
Depth (mbsf)	446.065	447.015	466.485	466.075	485.825	485.125	505.625
Lith. unit	8	8	8	8	9	9	9
Rock Type	LSB		LSB	LSB	HMA	HMA	LSB
Sum	91.06	99.00	90.31	94.70	99.16	96.08	90.71
LOI	7.03		9.36	5.69	1.90	2.89	8.30
Total wFeO	97.07	98.01	98.62	99.33	100.26	98.11	98.08
SiO_2	54.27	49.50	54.02	52.88	56.70	56.80	53.64
TiO_2	0.22	0.20	0.25	0.22	0.36	0.37	0.40
Al_2O_3	12.09	10.54	14.20	12.23	16.96	16.55	17.27
Fe_2O_3	7.95	7.55	8.12	8.05	7.08	7.76	8.16
FeO*	7.15	6.80	7.31	7.25	6.37	6.98	7.34
MnO	0.12	0.12	0.13	0.14	0.09	0.07	0.14
MgO	15.16	14.54	11.93	16.91	6.17	6.12	10.57
CaO	8.49	16.23	8.42	8.04	10.39	9.87	7.16
Na_2O	1.95	1.64	2.86	2.00	2.48	2.56	2.12
K_2O	0.49	0.38	0.84	0.28	0.42	0.62	1.30
P_2O_5	0.07	0.06	0.05	0.05	0.06	0.06	0.06
Zr	1.6	4.3	15.8		16.8	13.4	22
Sr	108	142	112	131	184	178	153
Sc	27.1	34.5	23.2	24.2	22.6	24.2	30.4
V	133	136	122	107	184	170	175
Cr	1253	1283	1224	1156	108	120	200
Ni	405	413	465	518	41	42	58

Table 4. IODP 352-U1439C. (cont.)

Sample	32R-1-W 25/28	32R-4-W 120/123	35R-1-W 117/120	35R-2-W 76/79	37R-1-W 101/104	37R-2-W 31/34	39R-2-W 131/134
Lith. unit	8	8	8	8	9	9	9
Rock Type	LSB		LSB	LSB	HMA	HMA	LSB
Sc	19.2	15.8	22.5	21.8	29.9	28.0	36.2
V	136.7	108.9	128.4	122.7	208.7	187.0	221.9
Cr	287.9	245.9	286.0	288.2	98.1	98.3	211.3
Co	59.1	44.5	49.9	56.2	34.4	33.1	35.6
Ni	371.1	327.6	443.6	497.1	41.8	37.5	58.4
Rb	5.0	6.0	10.3	4.1	4.4	10.8	6.4
Sr	92.0	116.3	98.0	114.4	171.3	165.5	145.2
Y	5.32	4.51	4.90	4.98	8.99	8.00	8.45
Zr	21.1	18.7	24.2	24.3	32.9	31.8	30.8
Nb	0.371	0.361	0.385	0.399	0.642	0.563	0.530
Ba	7.3	12.3	27.6	12.4	17.8	17.0	91.1
La	0.986	0.656	0.657	0.729	1.372	1.261	1.162
Ce	2.477	1.771	2.262	2.202	3.720	3.517	3.542
Pr	0.362	0.283	0.373	0.348	0.588	0.569	0.550
Nd	1.807	1.417	1.873	1.780	3.031	2.860	2.793
Eu	0.228	0.193	0.260	0.235	0.413	0.384	0.383
Sm	0.580	0.483	0.602	0.588	0.990	0.971	0.937
Gd	0.758	0.633	0.762	0.758	1.312	1.215	1.252
Tb	0.135	0.114	0.136	0.132	0.240	0.223	0.228
Dy	0.885	0.793	0.887	0.900	1.549	1.447	1.532
Ho	0.209	0.180	0.204	0.198	0.361	0.325	0.336
Er	0.616	0.556	0.592	0.573	1.075	0.951	0.969
Tm	0.093	0.091	0.089	0.087	0.163	0.140	0.141
Yb	0.620	0.581	0.614	0.592	1.051	0.881	0.901
Lu	0.098	0.094	0.095	0.094	0.164	0.133	0.137
Hf	0.630	0.582	0.722	0.706	0.974	0.932	0.925
Ta	0.040	0.045	0.057	0.052	0.151	0.074	0.064
Pb	0.566	0.707	0.833	1.063	0.575	0.679	0.702
Th	0.067	0.066	0.064	0.068	0.136	0.122	0.099
U	0.131	0.054	0.033	0.042	0.133	0.095	0.140

Table 4. IODP 352-U1439C. (cont.)

Sample	39R-3-W 23/27	40R-2-W 33/37	42R-2-W 14/17	43R-2-W 60/63	45R-1-W 47/51	46G-1-W 57/60
Depth (mbsf)	504.55	509.45	518.455	524.415	541.29	532.585
Lith. unit	9	9	10	10	10	10
Rock Type	LSB	BB	HMA	HMA	LSB	LSB
Sum	91.42	93.69	99.08	96.07	98.95	93.98
LOI	8.52	5.51	2.29	2.92		5.80
Total wFeO	99.02	98.29	100.44	98.04	98.05	98.85
SiO_2	53.30	53.38	58.48	54.28	56.09	55.46
TiO_2	0.38	0.38	0.44	0.45	0.40	0.41
Al_2O_3	17.25	17.02	16.07	17.24	16.12	16.30
Fe_2O_3	8.06	8.04	8.12	8.54	7.84	8.23
FeO*	7.25	7.24	7.30	7.68	7.06	7.41
MnO	0.14	0.12	0.08	0.09	0.16	0.14
MgO	10.56	9.83	5.64	7.72	9.96	10.02
CaO	7.82	8.49	8.87	9.54	6.98	7.22
Na_2O	2.19	2.35	2.71	2.58	2.79	2.70
K_2O	1.07	1.13	0.34	0.32	0.39	0.28
P_2O_5	0.05	0.07	0.07	0.08	0.06	0.06
Zr	16.3	17.5	20.5	10.9	3.2	29.7
Sr	160	187	177	189	156	142
Sc	27.1	28.7	33.4	27.7	30.5	32.8
V	190	173	196	206	198	205
Cr	198	221	103	94	282	268
Ni	54	63	30	35	42	46

Table 4. IODP 352-U1439C. (cont.)

Sample	39R-3-W 23/27	40R-2-W 33/37	42R-2-W 14/17	43R-2-W 60/63	45R-1-W 47/51	46G-1-W 57/60
Lith. unit	9	9	10	10	10	10
Rock Type	LSB	BB	HMA	HMA	LSB	LSB
Sc	31.2	33.5	29.1	30.7	33.3	35.3
V	199.7	194.6	205.3	212.8	201.9	213.5
Cr	194.5	197.0	91.8	98.7	268.0	284.2
Co	37.1	32.6	34.3	34.7	34.1	34.9
Ni	54.8	57.4	33.6	37.8	48.5	46.2
Rb	5.9	6.9	2.7	3.1	1.7	1.1
Sr	143.0	172.6	163.8	175.2	133.1	134.5
Y	7.03	9.55	10.90	10.40	8.355	8.419
Zr	29.9	28.8	40.5	37.6	30.0	32.0
Nb	0.506	1.221	0.758	0.677	0.598	0.674
Ba	77.8	74.0	18.3	9.8	26.4	20.2
La	0.966	1.637	1.489	1.297	0.975	0.963
Ce	3.179	4.240	4.363	3.907	3.000	2.947
Pr	0.509	0.681	0.715	0.673	0.523	0.515
Nd	2.643	3.429	3.758	3.448	2.782	2.734
Eu	0.345	0.458	0.475	0.481	0.392	0.402
Sm	0.908	1.106	1.282	1.180	0.997	0.992
Gd	1.180	1.516	1.721	1.579	1.365	1.313
Tb	0.202	0.280	0.287	0.288	0.243	0.250
Dy	1.383	1.729	2.012	1.890	1.621	1.643
Ho	0.304	0.408	0.431	0.428	0.357	0.364
Er	0.846	1.121	1.256	1.247	1.026	1.030
Tm	0.132	0.187	0.185	0.185	0.154	0.158
Yb	0.862	1.132	1.293	1.164	0.956	1.022
Lu	0.130	0.203	0.192	0.182	0.138	0.150
Hf	0.883	1.138	1.207	1.163	0.904	0.993
Ta	0.082	0.652	0.097	0.082	0.108	0.208
Pb	0.583	0.901	0.486	0.750	0.572	0.666
Th	0.103	0.185	0.118	0.101	0.097	0.097
U	0.119	0.108	0.102	0.174	0.134	0.116

Appendix C. Modeling Legend

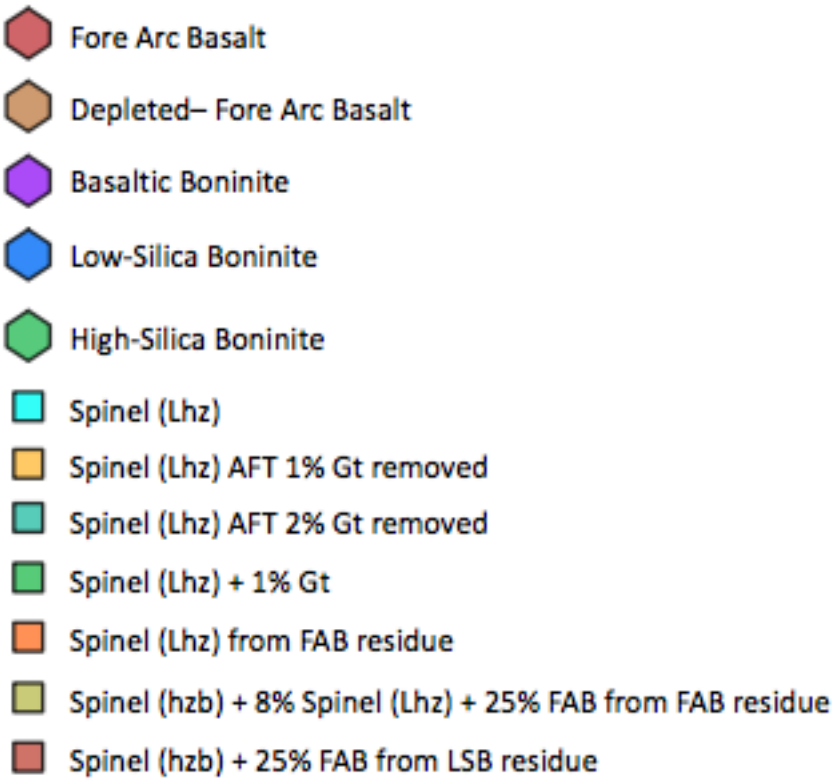

Appendix D. Geochemical Core Comparison

Core U1440

Core U1440 has 15 units. Unit 15 is a section of the dike and sill complex. Units 8-14 are part of the transition zone. All Units are dominantly FAB.

Unit 1

Depth: 115.36–115.88 mbsf

Thickness: 0.52 m

Rock type: heterolithic breccia

Deposit: talus breccia or similar

Unit 1 has 3 samples of FAB. The ranges from these three samples are: TiO2 - 0.61-1.22 wt%, Cr - 35-301 ppm, and Ti/Zr - 152.79-232.87.

Unit 1 samples create a range of values for major elements: FeO - 9.48-13.34 wt%, Na_2O - 2.03-2.92 wt%, Al_2O_3 - 15.54-16.97 wt%, CaO - 11.35-12.85 wt%. The samples are spread out indicating a possible mixing unit.

Unit 2

Depth: 115.9–164.2 mbsf

Thickness: 48.3 m

Rock type: aphyric basalt

Deposit: massive or sheet flows

Unit 2 is characterized by relatively low Cr (<60 ppm) and intermediate TiO_2 (0.8–1.2 wt%)

Unit 2 consists of 7 samples of FAB. The ranges on these samples are: TiO_2 - 0.92-0.98 wt%, Cr - 34-85 ppm, and Ti/Zr - 152.33-164.62. These samples fall within, or close to, the range determined but he shipboard definition of Unit 2.

Unit 2 samples create a range of values for major elements: FeO - 11.1-12.49 wt%, Na_2O - 2.03-2.92 wt%, Al_2O_3 - 14.07-15.5 wt%, CaO - 10.83-11.83 wt%. This unit has lower Al_2O_3 and slightly lower CaO than Unit 1.

Unit 3

Depth: 164.2–166.3 mbsf

Thickness: 2.14 m

Rock type: plagioclase-phyric basalt

Deposit: pillow lava

Unit 3 is chemically distinguished from the units above and below it by the combination of relatively high Cr concentrations (≥150 ppm), the lowest TiO_2 in Hole U1440 (~0.5 wt%), and the dominance of quench-textured mesostasis

Unit 3 has 6 FAB samples. These samples create the ranges: TiO_2 - 0.56-1.35 wt%, Cr - 56-270 ppm, and Ti/Zr - 149.68-161.84. These samples vary from the shipboard definition of Unit 3 by higher TiO_2 and higher Cr.

Unit 3 samples create a range of values for major elements: FeO - 8.92-12.88 wt%, Na_2O - 1.67-2.46 wt%, Al_2O_3 - 14.72-16.1 wt%, CaO - 11.34-13.43 wt%. Value ranges are spread out similar to Unit 1, indicating a possible mixing zone.

Unit 4

Depth: 166.3–212.4 mbsf

Thickness: 46.1 m

Rock type: aphyric basalt

Deposit: massive sheet flow

This 46.1 m thick unit is characterized by higher Ti than any of the other units (1.2–1.5 wt% TiO_2) and by low Cr (<85 ppm) relative to Unit 3.

Unit 4 has 3 FAB samples with ranges: TiO_2 - 1.34-1.36 wt%, Cr - 78-112 ppm, and Ti/Zr - 147.88-153.79. These samples have the highest TiO_2 of core U1440. Cr values are higher than defined but still within range of Unit 3.

Unit 4 samples create a range of values for major elements: FeO - 12.94-13 wt%, Na_2O - 2.38-2.52 wt%, Al_2O_3 - 14.76-14.93 wt%, CaO - 11.33-11.43 wt%. Some of the highest FeO values. Similar Na_2O, CaO, and Al_2O_3 to Unit 3.

Unit 5

Depth: 212.4–226.7 mbsf

Thickness: 14.3 m

Rock type: aphyric microcrystalline to fine-grained basalt

Deposit: pillow lavas

Unit 5 is clearly distinguished from the adjacent units on the basis of its color, macroscopic structures, and high Cr content (~100 ppm) relative to Units 4 and 6

Unit 5 has 4 FAB samples with the ranges: TiO_2 - 0.95-1.29 wt%, Cr - 92-

247 ppm, and Ti/Zr - 138.91-157.03. These samples fall within the shipboard definition by having high Cr content.

Unit 5 samples create a range of values for major elements: FeO - 11.19-12.46 wt%, Na_2O - 2.34-2.42 wt%, Al_2O_3 - 14.86-15.88 wt%, CaO - 11.34-13.13 wt%. Similar values to Unit 2.

Unit 6

Depth: 226.7–227.5 mbsf

Thickness: 0.8 m

Rock type: andesite vitrophyre

Deposit: hyaloclastite or glassy lava flow

Unit 6 is an andesite characterized chemically by its relatively high Zr concentrations (110–150 ppm) and relatively low Cr concentrations (<50 ppm).

Unit 6 has 2 FAB samples making the ranges: TiO_2 - 1.02-1.09 wt%, Cr - 62-80 ppm, Zr - 112.05-141.52 ppm, and Ti/Zr - 46.13-54.47. These samples have high Zr content and similar Cr content as the shipboard definitions. This unit has the lowest Ti/Zr ratio of core U1440.

Unit 6 samples create a range of values for major elements: FeO - 11.84-12.03 wt%, Na_2O - 2.84-3.13 wt%, Al_2O_3 - 14.68 wt%, CaO - 8.83-10.63 wt%. Some of the highest Na_2O and lowest CaO. FeO and Al_2O_3 values similar to Units 4 and 2.

Unit 7

Depth: 227.5–260.8 mbsf

Thickness: 33.3 m

Rock type: basalt vitrophyre and microcrystalline basalt

Deposit: sheet flows/hyaloclastite breccia

Unit 7 is clearly distinguishable chemically from Unit 6 by its lower Zr content.

Unit 7 has 7 FAB samples with the following ranges: TiO_2 - 0.99-1.1 wt%, Cr - 81-236 ppm, Zr - 35.68-47.25 ppm, and Ti/Zr - 125.71-168.6. These samples have less Zr than Unit 6 defined by the shipboard units. These samples also have higher Ti/Zr ratios than Unit 6.

Unit 7 samples create a range of values for major elements: FeO - 11.47-12.56 wt%, Na_2O - 2.22-2.54 wt%, Al_2O_3 - 13.89-15.59 wt%, CaO - 11.18-11.36 wt%. Chemically smilier to Units 2 and 4 on all elements.

Unit 8

Depth: 260.8–280.36 mbsf

Thickness: 19.5 m

Rock type: aphyric to augite-plagioclase phyric basalt

Deposit: sheet or massive flows and hyaloclastite

Unit 8 is characterized by high concentrations of Cr (150–220 ppm) relative to the units above and below it.

Unit 8 has 3 FAB samples with the ranges: TiO_2 - 0.99-1.07 wt%, Cr - 236-272 ppm, and Ti/Zr - 123.44-125.91. These samples have higher Cr than the

shipboard definition, however as the definition also is being higher than Unit 7 and 9, the defnition is sound.

Unit 8 samples create a range of values for major elements: FeO - 110.26-12.41 wt%, Na_2O - 2.22-2.54 wt%, Al_2O_3 - 13.89-15.18 wt%, CaO - 11.2-12.44 wt%. Very similar to Unit 7 but with a greater range in CaO and Al_2O_3.

Unit 9

Depth: 280.3–290.0

Thickness: 9.7 m

Rock type: aphyric basalt

Deposit: massive sheet flows

Unit 9 is distinguished from Unit 8 by its lower Cr (50–70 ppm) and from Unit 10 by lower TiO_2 (<1 wt%).

Unit 9 has 2 FAB samples making the ranges: TiO_2 - 0.96-1.03 wt%, Cr - 62-122 ppm, and Ti/Zr - 171.39-177.11. This unit has lower Cr than Unit 8 and has similar TiO_2 concentration to the shipboard definition.

Unit 9 samples create a range of values for major elements: FeO - 11.23-12.33 wt%, Na_2O - 2.36-2.65 wt%, Al_2O_3 - 13.96- 15.25 wt%, CaO - 10.79-10.92 wt%. Lower CaO than Unit 8, but otherwise very similar.

Unit 10

Depth: 290.0–290.4 mbsf

Thickness: 0.4 m

Rock type: aphyric basalt

Deposit: hyaloclastite breccia and pillow lava

It is distinguished from the adjacent units by its higher Cr concentrations (~110–120 ppm) and by its glass-rich horizons.

Unit 10 has 3 FAB samples defining the ranges: TiO_2 - 1-1.05 wt%, Cr - 106-192 ppm, and Ti/Zr - 151.88-160.82. These samples have higher Cr similar to the shipboard definition.

Unit 10 samples create a range of values for major elements: FeO - 10.65-12.43 wt%, Na_2O - 2.25-2.56 wt%, Al_2O_3 - 14.5-15.33 wt%, CaO - 10.78-11.62 wt%. Slightly lower Na_2O and FeO with slightly higher CaO than Unit 9.

Unit 11

Depth: 290.4–303.3 mbsf

Thickness: 12.9 m

Rock type: aphyric doleritic basalt

Deposit: intrusive sheet (dike/sill), or sheet flow

Unit 11 is distinguished from the adjacent units by its overall coarser grain size and low Cr concentrations (~70 ppm).

No data from samples analyzed here.

Unit 12

Depth: 300.3–309.5 mbsf

Thickness: 6.2 m

Rock type: aphyric basalt

Deposit: sheet flow (or intrusive sill)

It is essentially identical chemically to Unit 10 (above), implying that Unit 11 represents a dike or sill that intruded a single volcanic flow

Unit 12 has 3 samples defining the range of: TiO_2 - 0.94-1.05 wt%, Cr - 66-178 ppm, and Ti/Zr - 151.77-154.44. Unit 12 closely resembles Unit 10 chemically with minor variations.

Unit 12 samples create a range of values for major elements: FeO - 10.79-11.08 wt%, Na_2O - 2.02-2.45 wt%, Al_2O_3 - 14.44-15.24 wt%, CaO - 10.66-12.36 wt%. Chemically very similar to Unit 11.

Unit 13

Depth: 309.5–319.7 mbsf

Thickness: 10.2 m

Rock type: sparsely to moderately plagioclase- and augite-micro- phyric basalt

Deposit: pillow lava flows

Unit 13 volcanics are characterized by the highest Sr concentrations of any unit sampled (>80 ppm) and by relatively low Cr concentrations. In contrast, the dike is chemically similar to rocks in the overlying volcanic section, with Sr of <70 ppm and Cr of ≥150 ppm.

Unit 13 has 3 FAB samples making the ranges: TiO_2 - 0.88-1.03 wt%, Cr - 33-270 ppm, Sr - 89-109 ppm, and Ti/Zr - 137.34-140.45. Sr values are high similar to the shipboard definition, but the Cr values are also high.

Unit 13 samples create a range of values for major elements: FeO - 10.33-10.84 wt%, Na_2O - 2.2-2.73 wt%, Al_2O_3 - 15.43-16.4 wt%, CaO - 9.44-12.52 wt%. Slightly lower FeO and CaO with slightly higher Na_2O and Al_2O_3 than Unit 13.

Unit 14

Depth: 319.7–329.0 mbsf

Thickness: 9.3 m

Rock type: aphyric to augite or plagioclase-microphyric basalt

Deposit: hyaloclastite breccia

Unit 14 is chemically distinguished from Unit 13 by a 3- to 4-fold increase in Cr concentration.

Unit 14 has 3 FAB samples which define the range in values: TiO_2 - 0.97-1.03 wt%, Cr - 38-148 ppm, and Ti/Zr - 139.72-150.18. Cr levels are lower in these samples than Unit 13, unlike the shipboard definition.

Unit 14 samples create a range of values for major elements: FeO - 11.03-11.94 wt%, Na_2O - 2.17-3.01 wt%, Al_2O_3 - 14.4-16.58 wt%, CaO - 9.3-10.61 wt%. Slightly higher FeO and Na_2O with slightly lower Al_2O_3 and comparable CaO to Unit 13.

Unit 15

Depth: 329.0 mbsf

Thickness: NA

Rock type: aphyric to plagioclase-augite phyric basalts

Deposit: intrusive sheets: dike or sill complex

Unit 15 has 10 FAB samples which are all a part of the dike and sill complex and are separated into several subunits not discussed here. The ranges for these samples include: TiO_2 - 0.81-1.24 wt%, Cr - 25-327, and Ti/Zr 131.95-368.13.

Unit 15 samples create a range of values for major elements: FeO - 8.55-12.24 wt%, Na_2O - 2.02-2.52 wt%, Al_2O_3 - 14.03-15.57 wt%, CaO - 10.55-12.82 wt%. These samples span a large range with distinct units within.

Core U1441

Core U1441 has 4 Units. This core is heavily fractured and a large fault prevented further drilling of the core.

Unit 1

Depth: 83.0–151.0 mbsf

Thickness: 68.00 m thick (8.20 m recovered)

Rock type: aphyric basalt

Deposit: homolithic breccia

Volcanic blocks in Unit 1 are characterized by low TiO_2 (0.65– 0.70 wt%) and Cr (<100 ppm) and by Ti/Zr (150–170) ratios typical of Site U1440 FAB.

Unit 1 has 3 FAB samples with ranges of: TiO_2 - 0.66-0.78 wt%, Cr - 105-118 ppm, and Ti/Zr - 136.82-142.71. These samples have slightly higher TiO_2,

higher than reported Cr, and lower Ti/Zr.

Unit 1 samples create a range of values for major elements: FeO - 8.97-15.91 wt%, Na_2O - 1.75-2.22 wt%, Al_2O_3 - 15.91-16.78 wt%, CaO - 9.04-11.65 wt%. Highest Al_2O_3, lowest CaO, and a broad range of values for FeO and Na_2O.

Unit 2

Depth: 151.00–170.60 mbsf

Thickness: 19.6 m thick (0.86 m recovered)

Rock type: aphyric to sparsely clinopyroxene-phyric basalt

Deposit: basaltic pillow lava flow

Unit 2 is characterized by compositions similar to those of basalts at Site U1440, but slightly more depleted, with ~0.8 wt% TiO_2, ~130 ppm Cr, and Ti/Zr ratios of ~150–170.

Unit 2 has 1 FAB sample with chemistry: TiO_2 - 0.87 wt%, Cr - 157 ppm, and Ti/Zr - 126.19. This sample is approximately equal to the shipboard definition, however Ti/Zr is lower then listed values.

The Unit 2 sample has the following chemistry: FeO - 11.35 wt%, Na_2O - 2.06 wt%, Al_2O_3 - 15.57 wt%, CaO - 12.1 wt%. This sample has lower Al_2O_3 and higher CaO and FeO than Unit 1.

Unit 3

Depth: 170.60–180.25 mbsf

Thickness: 9.68 m (0.7 m recovered)

Rock type: clinopyroxene-plagioclase-phyric basalt (D-FAB)

Deposit: basalt lava flow

Unit 3 is the most depleted basalt composition recovered during this expedition and is characterized by low TiO_2 (~0.4 wt%) and extremely low Zr (~11–12 ppm), high Cr (350–480 ppm), and Ti/Zr ratios of ~220–240.

Unit 3 has 1 FAB sample with chemistry: TiO_2 - 0.47 wt%, Cr - 591 ppm, Zr - 14.17 ppm, and Ti/Zr - 197.19. This sample is similar to the shipboard definition with small variability.

This Unit 3 sample has the following chemistry: FeO - 9.16 wt%, Na_2O - 1.52 wt%, Al_2O_3 - 16.32 wt%, CaO - 13.91 wt%. Al_2O_3 and FeO values are similar to Unit 1. The CaO value is the highest in this core and Na_2O is the lowest.

Unit 4

Depth: 182.25–205.70 mbsf

Thickness: 25.45 m (1.19 m recovered)

Rock type: aphyric to sparsely clinopyroxene-bearing basalt

Deposit: basaltic massive lava flow

Unit 4 is characterized by compositions very similar to basalts at Site U1440, with ~1.0 wt%, TiO_2, ~150 ppm Cr, and Ti/Zr ratios of ~160–190.

Unit 4 has 4 FAB samples making the ranges of: TiO_2 - 0.87-0.99 wt%, Cr - 182-222 ppm, and Ti/Zr - 159.07-168.88. This sample has higher Cr, lower TiO_2, and is within range of Ti/Zr reported in the shipboard definition.

Unit 4 samples create a range of values for major elements: FeO - 10.09-11.42 wt%, Na_2O - 2.02-2.41 wt%, Al_2O_3 - 15.49-15.83 wt%, CaO - 11.31-12.65 wt%. Chemically very similar to Unit 2.

Core U1442

Core U1442 has 4 units with subunits 1a, 1b, 1c, 1d, 1e, 2a, and 2b. The upper portion of U1442, all of Unit 1, is dominated by HSB. The lower portion of core U1442 is dominated by LSB type boninite with a significant HMA component.

Unit 1a

Depth: 83.12–110.90 mbsf

Thickness: 27.78 m (2.42 m recovered)

Rock type: orthopyroxene ± olivine-phyric high-silica boninite

Deposit: hyaloclastite

Subunit 1a is characterized by low TiO_2 (<0.3 wt%), 300–500 ppm Cr, and low Ti/Zr ratios (30–50).

Subunit 1a has 2 samples: HSB and a high-magnesium andesite. The values for these samples create the range: TiO_2 - 0.2-0.33 wt%, Cr - 244-467 ppm, and Ti/Zr - 37.11-64.09. These samples do not fall within the shipboard definition exactly, higher TiO_2, lower Cr, and higher Ti/Zr. However, the HSB sample falls within shipboard definition, only the HMA does not.

Unit 1a samples create a range of values for major elements: FeO - 7.4-

7.9 wt%, Na_2O - 2.18-2.7 wt%, Al_2O_3 - 12.63-16.81 wt%, CaO - 78.92-8.78 wt%.

Unit 1b

Depth: 110.90–124.34 mbsf

Thickness: 13.44 m (1.78 m recovered)

Rock type: orthopyroxene-olivine-phyric high-silica boninite

Deposit: massive lava flow

Subunit 1b is characterized by low TiO_2 (≤0.2 wt%), 400–800 ppm Cr, and low Ti/Zr ratios (40–50).

Subunit 1b has 2 samples, both of which are HSB. They create the ranges: TiO_2 - 0.14-0.18 wt%, Cr - 937-1204 ppm, and Ti/Zr - 39.86-44.49. While the TiO_2 and Ti/Zr values match with the shipboard definition of subunit 1b, these samples have much higher Cr.

Subunit 1b samples create a range of values for major elements: FeO - 7.78-7.94 wt%, Na_2O - 1.39-1.75 wt%, Al_2O_3 - 10.97-11.15 wt%, CaO - 7.51-7.79 wt%. This subunit has higher FeO than subunit 1a, and lower Al_2O_3 and Na_2O. CaO values are similar.

Unit 1c

Depth: 124.34–179.90 mbsf

Thickness: 55.56 m (5.54 m recovered)

Rock type: orthopyroxene ± olivine-phyric high-silica boninite

Deposit: hyaloclastite

Subunit 1c is characterized by low TiO_2 (<0.3 wt%), 300–500 ppm Cr, and low Ti/Zr ratios (40–50).

Subunit 1c has 3 samples: 2 HSB and 1 HMA. These samples fall in the ranges: TiO_2 - 0.21-0.27 wt%, Cr - 300-543 ppm, and Ti/Zr - 36.72-40.96. These samples have a lower Ti/Zr ratio than the shipboard definition and slightly higher Cr.

Subunit 1c samples create a range of values for major elements: FeO - 6.4-7.19 wt%, Na_2O - 2.28-2.98 wt%, Al_2O_3 - 12.02-13.84 wt%, CaO - 7.01-7.75 wt%. This subunit is lower in FeO and higher in Al_2O_3 and Na_2O. CaO values are similar.

Unit 1d

Depth: 179.90–208.10 mbsf

Thickness: 28.20 m (3.58 m recovered)

Rock type: orthopyroxene-olivine-phyric high-silica boninite

Deposit: lava flow

Subunit 1d is characterized by slightly higher TiO_2 (up to 0.35 wt%), 200–1300 ppm Cr, and slightly higher Ti/Zr ratios (50–70). The wide range in elemental concentrations (e.g., Cr) suggests that some samples may contain high proportions of cumulate crystals.

Subunit 1d has 2 samples, both of which are HMA. The ranges created by these samples are: TiO_2 - 0.24-0.32 wt%, Cr - 132-330 ppm, and Ti/Zr - 35.29-36.3. These samples are much closer in range than the shipboard definition. Cr

is slightly lower and Ti/Zr ratio is much lower.

Subunit 1d samples create a range of values for major elements: FeO - 7.08-7.67 wt%, Na_2O - 2.72-2.93 wt%, Al_2O_3 - 12.54-16.75 wt%, CaO - 7.08-8.2 wt%. These samples are similar to subunit 1c.

Unit 1e

Depth: 208.10–248.605 mbsf

Thickness: 40.505 m (6.975 m recovered)

Rock type: orthopyroxene ± olivine-phyric high-silica boninite

Deposit: hyaloclastite

This subunit is chemically similar to Subunit 1d

Subunit 1e has 2 samples: HSB and HMA. They form the ranges: TiO_2 - 0.19-0.32 wt%, Cr - 249-872 ppm, and Ti/Zr 40.03-44.18. The shipboard definition of subunit 1e is chemically similar to subunit 1d. The Cr and TiO_2 values are within range but the Ti/Zr ratio is still lower then the definition.

Subunit 1e samples create a range of values for major elements: FeO - 7.6-8.08 wt%, Na_2O - 1.86-2.71 wt%, Al_2O_3 - 11.43-16.65 wt%, CaO - 6.93-8.97 wt%. Higher FeO similar to subunit 1b. Looking only at the boninite sample, values are most similar to Subunit 1b.

Unit 2a

Depth: 248.605–305.89 mbsf

Thickness: 57.285 m (9.435 m recovered)

Rock type: aphyric to sparsely phyric high-silica boninite and high-Mg andesite

Deposit: hyaloclastite intermingled with evolved lava

The wide range in compositions (e.g., TiO_2 of ~0.25–0.45 wt% and Ti/Zr ratios of 60–85) and magnetic susceptibilities are consistent with a mixed magma origin for this subunit.

Subunit 2a has 1 sample which is an andesite. The geochemistry on this sample is: TiO_2 - 0.42 wt%, Cr - 46 ppm, and Ti/Zr - 60.18. This sample falls within the boundaries defined by the shipboard crew.

Subunit 2a samples create a range of values for major elements: FeO - 6.97 wt%, Na_2O - 3.08 wt%, Al_2O_3 - 17.71 wt%, CaO - 9.85 wt%. This andesite sample falls outside the values imposed by boninite. Higher Al_2O_3, CaO, and Na_2O with lower FeO.

Unit 2b

Depth: 305.89–393.52 mbsf

Thickness: 87.63 m (7.58 m recovered)

Rock type: sparsely olivine ± clinopyroxene ± plagioclase phyric high-magnesium andesite

Deposit: lava flow

This subunit has uniformly low Cr concentrations (≤250 ppm), moderate TiO_2, relatively high Ti/Zr ratios (50–90), and high magnetic susceptibilities.

Subunit 2b has 5 samples consisting of 3 HMA and 2 LSB. The ranges from these samples are: TiO_2 - 0.31-0.47 wt%, Cr - 15-552 ppm, and Ti/Zr -

53.51-75.24. In this case, these samples have moderate to high TiO_2, greater Cr than expected, and within range for Ti/Zr compared to the shipboard definition.

Subunit 2b samples create a range of values for major elements: FeO - 6.52-7.64 wt%, Na_2O - 2.09-3.76 wt%, Al_2O_3 - 14.93-16.72 wt%, CaO - 6.57-11.28 wt%. The boninites in this Subunit have higher Al_2O_3 and highest CaO. FeO and Na_2O fall within the range of other boninites in the core.

Unit 3

Depth: 393.52–461.60 mbsf

Thickness: 68.08 m (7.32 m recovered)

Rock type: aphyric to sparsely phyric high-magnesium andesite

Deposit: hyaloclastite intermingled with lava

The evolved lavas in Unit 3 are characterized by higher TiO_2 (~0.35 wt%), low Cr (<200 ppm), and Ti/Zr ratios of 70–90.

Unit 3 has 2 samples, both of which are HMA. These samples create the ranges: TiO_2 - 0.37 wt%, Cr - 95-104 ppm and Ti/Zr 64.44-65.91. They have the same concentration of TiO_2 which matches the higher TiO_2 shipboard definition. Cr also matches the shipboard definition, however the Ti/Zr ration is low for these samples.

Unit 3 samples create a range of values for major elements: FeO - 7.34-7.39 wt%, Na_2O - 2.51-2.58 wt%, Al_2O_3 - 17.09-17.56 wt%, CaO - 9.86-10.08 wt%. These samples are HMA but have very similar values to Subunit 2a.

Unit 4

Depth: 461.60–522.97 mbsf

Thickness: 61.37 m thick (11.21 m recovered)

Rock type: aphyric to augite ± plagioclase-phyric high-magnesium Andesite

Deposit: hyaloclastite and lava flows

Unit 4 has 1 sample which is a LSB. The concentrations of this sample are: TiO_2 - 0.27 wt%, Cr - 106 ppm, and Ti/Zr 65.89. These values are similar to Unit 3 with variation in TiO_2 resulting in a lower value for this sample.

The Unit 4 sample has the following chemistry: FeO - 5.5 wt%, Na_2O - 2.82 wt%, Al_2O_3 - 19.39 wt%, CaO - 8.73 wt%. This boninite sample has the highest Al_2O_3 and lowest FeO. This sample still has higher CaO and Na_2O than other units.

Core U1439

Core U1439 has 10 units with subunits 2a, 2b, 3a, 3b, and 9a, 9b. Units 1-4 are dominantly HSB, units 5-10 are dominantly LSB type boninite with a significant portion of HMA. No samples were collected from Unit 2, subunit 3b, or Unit 4.

Unit 1

Depth: 182.00–184.75 mbsf

Thickness: 2.75 m (1.86 m recovered)

Rock type: olivine-orthopyroxene phyric boninite and olivine-phyric high-

magnesium andesite

Deposit: massive lavas overlain by a breccia layer

All of the boninites are low in TiO_2 (≤0.3 wt%) and relatively high in Cr (250–1200 ppm) with Ti/Zr ratios ≤50

Unit 1 consists of 2 samples: HSB and BB. Compared to the shipboard unit definition, these samples fall within: TiO_2 - 0.15-0.21 wt%, Cr - 960-1220 ppm, and Ti/Zr - 40.35-42.05. These samples fall within range of the shipboard definition of Unit 1.

Unit 1 samples create a range of values for major elements: FeO - 7.27-7.97 wt%, Na_2O - 1.46-2.05 wt%, Al_2O_3 - 10.51-13 wt%, CaO - 6.99-11.9 wt%.

Unit 2a

Depth: 184.75–191.80 mbsf

Thickness: 7.05 m (0.50 m recovered)

Rock type: olivine ± orthopyroxene-phyric high-silica boninite

Deposit: massive lava, sheet flows

Unit 2a is dominated by high-silica boninites, with low TiO_2 (≤0.25 wt%), low Ti/Zr (≤60), and 900–1150 ppm Cr.

Unit 2b

Depth: 191.80–201.60 mbsf

Thickness: 9.80 m (5.25 m recovered)

Rock type: high-silica boninite scoria

Deposit: hyaloclastite/pyroclastic flow deposit

Subunit 2b is chemically identical to Subunit 2a (high-silica boninite).

No data for Unit 2 in samples analyzed here.

Unit 3a

Depth: 201.60–240.80 mbsf

Thickness: 39.20 m (5.50 m recovered)

Rock type: olivine + orthopyroxene-phyric high-silica boninite

Deposit: pillow lava with interpillow breccia

Subunit 3a lavas are high-silica boninites, with low TiO_2 (≤0.25 wt%), low Ti/Zr (≤50), and 300–1000 ppm Cr.

Unit 3b

Depth: 240.8–243.02 mbsf

Thickness: 2.22 m (1.94 m recovered)

Rock type: olivine-phyric high-silica boninite

Deposit: hyaloclastite breccia/pyroclastic flow deposit

Subunit 3b is chemically similar to Subunit 3a.

Unit 3 consists of 2 samples that fall within the subunit 3a: FAB and HSB. Despite the large difference in rock type, hey have similar trace geochemistry which falls within: TiO_2 - 0.18-0.28 wt%, Cr - 521-673 ppm, and Ti/Zr - 33.02-38.74. These values fall mostly within the shipboard definition, however the TiO_2 here is marginally higher (0.28 wt%).

Unit 3 samples create a range of values for major elements: FeO- 7.3-10.12 wt%, Na_2O - 2.33-3.1 wt%, Al_2O_3 - 12.21-17.12 wt%, CaO - 7.49-9.76 wt%. Unit 3 has higher FeO, Na_2O, and Al_2O_3 than Unit 1, but fall within the values for CaO.

Unit 4

Depth: 243.02–251.04 mbsf

Thickness: 8.02 m (0.98 m recovered)

Rock type: augite + plagioclase-phyric high-magnesium andesite

Deposit: pillow lava

Unit 4 is low in TiO_2 (≤0.4 wt%), low in Cr (<400 ppm), and has a low Ti/Zr ratio (<80), which is similar to that of the overlying boninites

No data for Unit 4 from samples analyzed here.

Unit 5

Depth: 251.04–285.10 mbsf

Thickness: 34.06 m thick (8.62 m recovered)

Rock type: olivine + orthopyroxene ± augite-phyric basaltic boninite

Deposit: pillow lava with interpillow breccia and glass

Unit 5 is characterized chemically by low TiO_2 (≤0.4 wt%), ~200–2000 ppm Cr, and very low Zr (15–25 ppm), resulting in high Ti/Zr ratios (80–110).

Unit 5 has 3 samples of that vary dramatically: Andesite, picrite, and LSB. Due to the nature of these rocks, the geochemistry is more spread out: TiO_2 -

0.3-0.44 wt%, Cr - 1-1031 ppm, Zr - 26.24-67.56 ppm, and Ti/Zr - 39.16-82.52. The andesite samples is more variable, while the LSB and picrite have similar values. These samples have slightly higher TiO_2 than the shipboard definition and higher Zr making the Ti/Zr ratio lower.

Unit 5 samples create a range of values for major elements: FeO - 6.46-7.79 wt%, Na_2O - 2.02-4.51 wt%, Al_2O_3 - 12.2-19.86 wt%, CaO - 7.39-15.77 wt%. The large range of values is due to the different rock types present.

Unit 6

Depth: 285.10–390.40 mbsf

Thickness: 105.3 m (45.0 m recovered)

Rock type: olivine ± orthopyroxene-phyric low-silica boninite

Deposit: pillow lavas (including megapillows) with interpillow breccia

Unit 6 is a low-silica boninite with high Cr (600–1200 ppm), low TiO_2 (0.30–0.40 wt%), and Ti/Zr of 65–75, on the border of the canonical limit for boninites.

Unit 6 has 10 samples: 8 LSB and 2 picrite. The geochemistry of these samples are all similar despite the difference in rock type: TiO_2 - 0.27-0.36 wt%, Cr - 920-1329 ppm, and Ti/Zr - 61.41-78.06. These samples have slightly higher Cr, lower TiO_2, and similar Ti/Zr ratios.

Unit 6 samples create a range of values for major elements: FeO - 7.32-8.62 wt%, Na_2O - 1.74-2.26 wt%, Al_2O_3 - 10.66-12.96 wt%, CaO - 7.31-15.96 wt%. Similar boninite values to Unit 5, main difference is the andesite in Unit 5.

Unit 7

Depth: 390.40–397.75 mbsf

Thickness: 7.35 m thick (1.67 m recovered)

Rock type: augite ± olivine ± plagioclase-phyric high-magnesium Andesites

Deposit: massive lava; allochthonous, with fault breccias at upper and lower contacts

Unit 7 is characterized by high Ti/Zr (100–120) and relatively high magnetic susceptibilities.

Unit 7 has 1 sample: LSB. The geochemistry on this sample is: TiO_2 - 0.23 wt%, Cr - 1385 ppm, and Ti/Zr - 63.63. Only Ti/Zr is reported from the shipboard definition which this sample does not fall in, having a lower ratio.

The Unit 7 sample has the following chemistry: FeO - 7.84 wt%, Na_2O - 1.76 wt%, Al_2O_3 - 11.1 wt%, CaO - 7.51 wt%. This Unit 7 sample of LSB falls within he range of Unit 6.

Unit 8

Depth: 397.75–476.21 mbsf

Thickness: 78.46 m thick (36.37 m recovered)

Rock type: olivine (± orthopyroxene, ± augite)-phyric low-silica boninite with intercalated augite-phyric high-magnesium andesite

Deposit: pillow lava, some massive flows

Boninites of Unit 8 are low-silica boninites containing low TiO_2 but relatively high Ti/Zr (65–75). Unit 8 high-magnesium andesites have low Cr concentrations (<300 ppm), but their Ti/Zr ratios are essentially identical to the low-silica boninites, suggesting they are derived from a similar parent magma

Unit 8 has 7 samples: 6 LSB and 1 picrite. Despite the picrite being a different rock type, it falls within the LSB range on geochemical values: TiO_2 - 0.2-0.25 wt%, Cr - 1151-1678 ppm, and Ti/Zr - 50.27-64.28. Comparing the shipboard Ti/Zr ratio, these samples have lower ratios that do not fall within reported values.

Unit 8 samples crate a range of values for major elements: FeO - 6.8-8.13 wt%, Na_2O - 1.64-2.86 wt%, Al_2O_3 - 10.45-14.2 wt%, CaO - 6.9-16.23 wt%. Lower FeO than Unit 6, otherwise, within range of Units 6 and 7.

Unit 9a

Depth: 476.21–504.30 mbsf

Thickness: 28.10 m (2.96 m recovered)

Rock type: aphyric to sparsely augite-phyric high-magnesium andesite

Deposit: pillow lava with some massive sheet flows

Subunit 9a high-magnesium andesites have low Cr (<200 ppm) and Ti/Zr ratios of 60–70, similar to Unit 8.

Unit 9b

Depth: 504.30–514.10 mbsf

Thickness: 9.80 m thick (7.32 m recovered)

Rock type: aphyric high-magnesium andesite

Deposit: pillow lava (single flow)

Subunit 9b has higher Ti/Zr ratios (75–120) than Subunit 9a.

Unit 9 has 5 samples with 2 samples in subunit 9a: 2 high-magnesium andesites, and 3 samples in subunit 9b: 2 LSB and 1 BB. Subunit 9a values are: TiO_2 - 0.36-0.37 wt%, Cr - 108-120 ppm, and Ti/Zr - 66.54-69.08. This subunit falls within the shipboard definition. Subunit 9b values are: TiO_2 - 0.38-0.4 wt%, Cr - 198-221 ppm, and Ti/Zr - 76.39-78.24. This subunit has slightly higher Cr than shipboard definition, but the Ti/Zr ratio is good.

Subunit 9a samples create a range of values for major elements: FeO - 6.37-6.98 wt%, Na_2O - 2.48-2.56 wt%, Al_2O_3 - 16.55-16.96 wt%, CaO - 9.87-10.39 wt%. Subunit 9b samples create a range of values for major elements: FeO - 7.24-7.34 wt%, Na_2O - 2.12-2.35 wt%, Al_2O_3 - 17.02-17.27 wt%, CaO - 7.16-8.49 wt%. The differences between Subunits 9a and 9b are due to different rock type, boninites fall within range of other units with the exception of Al_2O_3 being higher than all other units.

Unit 10

Depth: 514.10–542.23 mbsf

Thickness: 28.13 m thick (7.56 m recovered)

Rock type: aphyric to olivine + augite-phyric high-magnesium andesite and boninitic dolerite

Deposit: dikes and/or sills

Unit 10 has relatively high TiO_2 (0.35–0.5 wt%), high Ti/Zr (75–110), and low Cr (<500 ppm).

Unit 10 has 4 samples: 2 LSB and 2 high-magnesium andesites. The values are: TiO_2 - 0.4-0.45 wt%, Cr - 94-282 ppm, and Ti/Zr - 65.67-79.62. With the exception of Ti/Zr ratio which is lower than defined, this sample falls within the shipboard definition.

Unit 10 samples create a range of values for major elements: FeO - 7.06-7.68 wt%, Na_2O - 2.58-2.79 wt%, Al_2O_3 - 16.07-17.24 wt%, CaO - 6.98-9.54 wt%. Unit 10 falls within the same range of values for FeO and CaO. Differences lie in higher Al_2O_3 than most units and slightly lower than Unit 9. Na_2O values are also a little higher in Unit 10.